**NATIONAL TECHNICAL UNIVERSITY OF ATHENS**
SCHOOL OF NAVAL ARCHITECTURE AND MARINE ENGINEERING
DEPARTMENT OF MARINE STRUCTURES


# MSc Naval and Marine Technology

## Master Thesis

---

# Extreme Value Analysis of Environmental Parameters and Energy Output Estimation of a Multi-Purpose Floating Structure at Specific Locations in the Greek Seas Suitable for Wind and Wave Energy Exploitation

---

by

**Kimon Kardakaris**

Supervisor: Dr. Takvor Soukissian

*Research Director, Institute of Oceanography,*
*Hellenic Center for Marine Research*

*Athens, September 2022*

NATIONAL TECHNICAL UNIVERSITY OF ATHENS
SCHOOL OF NAVAL ARCHITECTURE AND MARINE ENGINEERING
DEPARTMENT OF MARINE STRUCTURES

MSc Naval and Marine Technology

---

# Extreme Value Analysis of Environmental Parameters and Energy Output Estimation of a Multi-Purpose Floating Structure at Specific Locations in the Greek Seas Suitable for Wind and Wave Energy Exploitation

---

Master Thesis

by

**Kimon Kardakaris**

**Defense Committee**

. . . . . .
Dr. T. SOUKISSIAN
*Research Director,*
*Institute of Oceanography, HCMR*

. . . . . .
Prof. D. KONISPOLIATIS
*Assistant Professor*
*Department of Marine Structures*

. . . . . .
Prof. K. BELIBASSAKIS
*Director of the Department of*
*Marine Hydrodynamics*

*Athens, September 2022*

# Acknowledgements

With the preparation of the present thesis, my postgraduate studies at the School of Naval Architecture and Marine Engineering in the National Technical University of Athens (NTUA) finish under a long but full of knowledge academic period. Applying for the MSc in *Naval and Marine Technology*, was a wish that came true, as it equipped me with insightful and more than useful theoretical and technical knowledge regarding ocean engineering, marine and offshore works, which are my main interests as a civil engineer. These two years were tough due to the COVID-19 situation; however, this MSc course could not have been completed without the help of some people who supported me and I would like to thank.

First of all, I would like to express my sincere gratitude to Dr. Takvor Soukissian, Research Director at the Institute of Oceanography of the Hellenic Center for Marine Research, who accepted to supervise me although his very busy schedule. His advice on the thesis's topic along with his continuous guidance, both on the thesis and on our published scientific article, contributed significantly to produce quality work.

Secondly, I would like to express my very great appreciation to Prof. Dimitrios Konispoliatis, Assistant Professor in the Department of Marine Structures at the School of Naval Architecture and Marine Engineering in NTUA, for his valuable and constructive suggestions during the planning and development of this project. His willingness to give his time so generously has been very much appreciated and helped the most not only for conducting the present research work, but also for giving me a deeper insight in the offshore structures analysis.

Last but not least, I would like to thank all my friends that were beside me all these years, yet I wish to express my deepest gratitude to my family for their continuous and unconditional support and encouragement throughout my life.

*Kimon Kardakaris*
*Athens, September 2022*

# Abstract

The present thesis describes the methodology for an Extreme Value Analysis of wind and wave parameters at three specific locations in the Greek seas that are known to be advantageous in terms of joint power production (both offshore wind and wave) and bathymetric conditions. The analysis is conducted via the Peak-Over-Threshold method examining wind speed, significant wave height and peak wave period data from the ERA5 reanalysis dataset. Moreover, a suitable multi-purpose floating platform is presented that can be adequately utilized for co-exploitation at the selected locations. The mooring system of the platform was also designed, as it was modified from the initial tensioned tethers concept (TLP) to catenaries. Regarding this, using the quasi-static approach, two cases were investigated in terms of material, studless chains and wire ropes, and their stiffness characteristics were specified. Subsequently, a coupled hydro-aero-elastic analysis was performed and special attention was drawn to platform's responses, OWCs' inner pressure as well as line tensions. Additionally, a dynamic analysis regarding the catenary mooring system consisting of studless chains was conducted in order to approach a more realistic behavior, taking into account the mooring damping effects. The aforementioned analyses were performed via software available at the Laboratory for Floating Structures and Mooring Systems (LFSMS) in the School of Naval Architecture and Marine Engineering in NTUA. Furthermore, offshore wind and wave energy output was estimated for the examined locations, whereas the different mooring systems were compared in terms of OWC efficiency. For offshore wind, results are presented in annual and monthly scale and the annual capacity factor is estimated, while for wave energy the JONSWAP spectrum is used. Last but not least, theoretical background referring to hydrodynamics, floaters and moorings are presented herein, along with a brief review on the status, research and development of the offshore wind market and infrastructure.

# Περίληψη

Η παρούσα διπλωματική εργασία περιγράφει τη μεθοδολογία για την ανάλυση ακραίων τιμών, ανεμολογικών και κυματικών παραμέτρων σε τρεις συγκεκριμένες τοποθεσίες στις ελληνικές θάλασσες, οι οποίες πλεονεκτούν όσον αφορά την κοινή παραγωγή ενέργειας (υπεράκτια αιολική και κυματική) και τη βαθυμετρία. Η ανάλυση διεξάγεται μέσω της μεθόδου Peak-Over-Threshold εξετάζοντας δεδομένα ταχύτητας ανέμου, σημαντικού ύψους κύματος και μέγιστης περιόδου κύματος από τη βάση δεδομένων του ERA5. Επιπλέον, παρουσιάζεται κατάλληλη πλωτή πλατφόρμα πολλαπλών χρήσεων για τη συνεκμετάλλευση στις επιλεγμένες θέσεις. Το σύστημα αγκύρωσής της σχεδιάστηκε εκ νέου, αφού τροποποιήθηκε από την αρχική ιδέα των προεντεταμένων τενόντων (TLP) σε αλυσοειδείς γραμμές. Χρησιμοποιώντας την οιονεί στατική προσέγγιση, διερευνήθηκαν δύο περιπτώσεις όσον αφορά το υλικό, δηλ. τυπικές αλυσίδες και συρματόσχοινα, και προσδιορίστηκαν τα χαρακτηριστικά δυσκαμψίας τους. Στη συνέχεια, πραγματοποιήθηκε συζευγμένη υδρο-αερο-ελαστική ανάλυση και δόθηκε ιδιαίτερη προσοχή στις αποκρίσεις της πλατφόρμας, στην εσωτερική πίεση των κυματικών μηχανών καθώς και στις τάσεις των γραμμών αγκύρωσης. Επιπλέον, διεξήχθη δυναμική ανάλυση όσον αφορά την περίπτωση των αλυσίδων, προκειμένου να προσεγγιστεί μια πιο ρεαλιστική συμπεριφορά, λαμβάνοντας υπόψη τα φαινόμενα απόσβεσης του συστήματος αγκύρωσης. Οι προαναφερθείσες αναλύσεις πραγματοποιήθηκαν μέσω λογισμικού που διατίθεται στο Εργαστήριο Πλωτών Κατασκευών και Συστημάτων Αγκύρωσης της Σχολής Ναυπηγών Μηχανολόγων Μηχανικών του ΕΜΠ. Επιπρόσθετα, εκτιμήθηκε η παραγωγή υπεράκτιας αιολικής και κυματικής ενέργειας για τις εξεταζόμενες τοποθεσίες, ενώ τα διάφορα συστήματα αγκύρωσης συγκρίθηκαν με κριτήριο την αποδοτικότητα των κυματικών μηχανών. Για την υπεράκτια αιολική ενέργεια, τα αποτελέσματα παρουσιάζονται σε ετήσια και μηνιαία κλίμακα και εκτιμάται ο ετήσιος συντελεστής δυναμικότητας, ενώ για την κυματική ενέργεια χρησιμοποιείται το φάσμα JONSWAP. Τέλος, παρουσιάζεται θεωρητικό υπόβαθρο που αναφέρεται στην υδροδυναμική, τους πλωτήρες και τα συστήματα αγκύρωσης, καθώς και μια σύντομη ανασκόπηση της κατάστασης, της έρευνας και της ανάπτυξης των υποδομών και της υπεράκτιας αιολικής αγοράς.

# Contents

# List of Figures

# List of Tables

# Chapter 1

# Introduction

## 1.1 General

Over the last decades, it is more and more evident that the global energy demands are rapidly increasing. This, along with the imminent fossil fuel deficiency, oblige governments and industries to make accelerated efforts on producing green energy. Onshore renewable energy systems are already in use for years, producing energy via wind and solar farms, as well as hydroelectric power plants. The main focus however, is spotted on the marine environment, which is a vast source of renewable energy. The oceans cover more than two-thirds of the Earth, representing a huge energy resource, containing far more energy than humans can use. The energy of the sea is stored as kinetic energy due to the movement of waves and currents and as thermal energy due to the sun. Although most marine energy is very diffuse, due to the vast expanse of the oceans, and far away from the terrestrial part of the planet, in special cases it can be effectively captured and used appropriately. Depending on the criteria and requirements of each form of ocean energy for efficient utilization, the locations on the planet are also limited. Hence, a well-managed ocean will be increasingly essential, in order for the ocean to deliver on its potential. Marine Spatial Planning (MSP) [1] will take care of the grid challenges and innovations in offshore wind and thus, it is of high importance not only to investigate the most suitable areas, but also to implement MSP even during the initial studies of the projects.

Another key topic in the renewables industry is hybridization, i.e., the combination of wind energy with another energy source. A hybrid power project can use complementary renewable technologies to create a stable supply of power and provide a feasible solution for rural electrification and community energy access. For example,

wind combined with solar PV can generate power during cloudy periods, less windy periods and darkness. This, in combination with the continuous innovation on wind turbines and other ocean energy systems, can establish generating energy with lower costs than electricity from conventional energy forms like fossil fuels, accomplishing grid parity. However, as the offshore wind industry expands, so will its demand for structural materials such as concrete and steel, critical minerals such as copper, nickel, chromium and manganese, and rare earths such as the neodymium and boron magnets in wind turbines. This not only intensifies the mining of minerals and rare earths, but also deepens the problem of environmental protection leading to a vicious cycle. The materials extraction process is the primary source of harmful emissions in the lifecycle of an offshore wind project, dominated by steel manufacturing. Life Cycle Assessment (LCA) studies are therefore more than necessary in order to mitigate such problems in the offshore wind supply chain [2].

The onshore wind farm development is usually restricted by land availability. Problems such as wind turbine noise and their visual impact on the natural environment are the main reasons for people to refuse to accept the building of onshore wind turbines close to residential areas. In contrast, although offshore wind turbines operate in the same manner as onshore wind turbines, installation at sea has a number of advantages: there is a lot more available space and fewer complaints about noise and visual intrusion. Besides, wind over the water is generally stronger, more consistent and much smoother than wind over land. However, compared to onshore wind farms, offshore wind turbines are more expensive and difficult to install and maintain due to the variable and rough sea conditions, construction, and operation phases as well as additional infrastructure regarding the electricity transmission to shore [3]. At present, the major barrier to the deployment of offshore wind energy on a massive scale is the high costs of offshore wind facilities. As offshore wind farms increase in size, wake effects within large offshore wind farms can influence considerably on their energy production and mechanical loads on individual turbine. The wind downstream of a wind turbine has reduced speed and is turbulent; this downstream wind is the wake of the turbine. As the wind flow proceeds further downstream, this wake will begin to spread and gradually return to free stream conditions. Due to the wake effect, power efficiency depends on the turbine layout and the nature of the site's wind regime, both in steady-state operation and dynamic performance of the wind farm and as a result, adequate turbine spacing is critical in order to minimize the total power losses [4, 5]. However, blockage effects i.e., the interaction of pressure jump across turbines, have to be taken into account as well, as this altering of the

velocity field can increase efficiency. Similar studies on tidal turbines showed that the efficiency increases, from the Lanchester-Betz limit of 0.593 to another limiting value of 0.798, as the spacing is reduced to the optimal value, yet regarding wind turbines the efficiency increases also, however less significantly [6–8].

## 1.2 Market Status

Among the technologies that exploit energy from the ocean, the most mature one is offshore wind energy. The Global Offshore Wind Report of 2021 from the Global Wind Energy Council (GWEC) states that from now to 2050, offshore wind becomes the main medium for global decarbonization, transforming the electricity system in generation and infrastructure, as well as for production of green fuels like hydrogen. Offshore wind is a key technology in net zero scenarios, with fixed-bottom offshore wind being in a rapid development until 2030 and floating offshore wind unlocking tremendous potential for fossil fuels displacement from 2030 and beyond.

The offshore wind market had grown from 2.2 GW in 2016 to 6.1 GW in 2020. As of 2020, a total of 73.33 MW net floating wind was installed globally, of which 32 MW was located in the UK, 25 MW in Portugal, 12 MW in Japan, 2.3 MW in Norway and 2 MW in France. The UK remained at the top spot globally in terms of cumulative offshore wind capacity as of the end of 2020, while China had overtaken Germany to become the world's second largest offshore wind market. Regarding Europe, Denmark, the Netherlands and France filled the top 5 on the European offshore market, while globally, apart from China, Japan as well as the US led on their respective continents [2]. According to the International Renewable Energy Agency (IRENA), China recorded the highest capacity of new offshore wind installations in 2020, with more than 3 GW, followed by the Netherlands with 1.5 GW, Belgium with 0.7 GW and the UK with 0.4 GW. In terms of other marine energy forms, cumulative global installed ocean energy capacity – including tidal and wave energy as well as ocean thermal energy conversion (OTEC) and salinity gradient – was more than 515 MW, by the end of 2020, with more than 98% of this capacity being operational. Globally, 31 countries are in pursue of ocean energy projects with leaders being European countries such as Finland, France, Ireland, Italy, Portugal, Spain, Sweden and the UK, in addition to Australia, Canada and the USA. However, these technologies have various degrees of maturity as well as challenges to consider on marine renewable infrastructure like developing the required grid and withstanding harsh offshore environment (e.g., salinity, corrosion, extreme forces, etc.) [9].

According to the latest GWEC Global Wind Report, the offshore wind market enjoyed its best ever year in 2021, with 21.1 GW commissioned scaling up offshore capacity to 57 GW, which is 7% of global installations. China contributed 80% of that offshore growth, the fourth year that China has led the way in new installations. Europe is the only other region to report new offshore wind installations in 2021, driven by a record year for the UK, where more than 2.3 GW was connected to the grid, followed by Denmark (608 MW) and the Netherlands (392 MW). Even though the UK relinquished its title as the world's largest offshore market to China, it leads the way with floating offshore wind, with 57 MW installed in 2021, bringing total capacity to 139 MW [10].

Over the next decade, it is expected that over 235 GW of new offshore wind capacity will be added, bringing total offshore wind capacity to 270 GW by 2030. 30% of this new volume will be installed in the first half of the decade (2021-2025), with the remaining to be connected in the latter half (2026-2030). The volume of annual offshore wind installations is expected to more than triple, from 6.1 GW in 2020 to 23.1 GW in 2025, bringing its share of global new installations from today's 6.5% to 20% by 2025. In total, more than 90 GW of offshore is expected to be added worldwide in 2022-2026, forming the annual average of offshore installations to 18.1 GW. As far as hybridization is concerned, it is well underway in many countries, currently mainly in Australia, the US, China and India. According to GWEC Market Intelligence, developers in the US have successfully presented 2238 MW of hybrid projects, while in China, 1350 MW of hybrid projects were awarded in 2021 and in India, respective projects of 2800 MW and 1950 MW were also awarded in 2020 and 2021 respectively. Apart from the known key players in offshore wind industry, promising offshore markets in the future are countries in Asia, Latin America and Africa such as Taiwan, Vietnam, Japan, India, Brazil, Colombia and Egypt [2].

## 1.3 Offshore wind and Infrastructure

The concept of a large scale Floating Offshore Wind Turbine (FOWT) was introduced at the University of Massachusetts back in 1972, but it gained more interest 20 years later when the wind industry was well established. Even though the majority of offshore wind farms consist of fixed-bottom structures, with the advances of technology into deeper waters, floating wind turbine platforms are capable of becoming more financially profitable due to the extreme abundance of the offshore wind potential. The offshore oil and gas industry has proven that the technical challenges can be

overcome but the economics of implementing such solutions would prohibit any deployment in a competitive wind energy market. However, one must keep in mind that floating systems can be assembled at a great extent in production facilities onshore, which can maximize production providing a lower cost than fixed bottom systems, which must be constructed at sea [11]. Additional advantages can be noted regarding the FOWTs, firstly considering the fact that offshore wind is a more constant and predictable wind resource. It is also possible to develop wind farms in deeper waters and areas subjected to earthquakes, reducing the visual impact as well. Last but not least, anchoring installation does not require the use of sophisticated vessels while floating substructures can be designed to be reused in various site locations [12].

Regarding bottom-fixed offshore wind turbines, their substructures can be modified variously depending on the installation depth. In shallow waters (i.e., up to 20-40 m) gravity-based designs and monopiles (or tripiles) are mostly used, whereas in intermediate waters (i.e., up to 50-70 m) tripods or lattice structures (jackets) are the main solution [13]. As far as operating principle is concerned, the floating platforms that support the wind turbines can be classified into three main categories (Fig. 1.1).

- *Buoyancy stabilized platforms*

  In this category, the stability is achieved through buoyancy and there are two main concepts of structures; semi-submersible platforms and barges. The barge concept uses a large waterplane area and shallow draft to maintain stability, yet it is not so popular for offshore wind applications. The semi-submersible concept is initially originated from the oil-and-gas industry. It comprises of columns, providing the main volume underwater, and connecting members that provide structural integrity to the system as a whole. Regarding wind turbine platforms, this concept evolved considering that the payload of wind turbines is lower and the required deck space is equally reduced, thus reducing the total volume of the platform to achieve lower costs [14]. To provide, however, sufficient buoyancy and stability, such structures have high structural mass and complex steel designs with many welded joints which can be difficult to fabricate. Another drawback is the potentially high costs on active ballast systems, yet in terms of repairs, they can easily be done port-side. Semi-submersibles can operate in shallow waters, requiring only basic tug boats, and the turbine assembly can be done onshore, minimizing the offshore installation procedures [15].

- *Mooring stabilized platforms*

  The oil and gas industry initially developed tension leg platforms (TLPs) as a

cost-effective way of exploiting deeper waters, dating back to 1970s. The first working TLP was successfully deployed by Conoco in the North Sea in the 1980s. The main feature of a TLP is that instead of relying on the buoyancy resulting from the underwater geometry, the stability of the structure is provided by vertical taut mooring lines [14]. Along with excellent stability and low structural mass of this concept, a couple of more advantages are the onshore turbine assembly and no requirements for active ballast. However, it is necessary to use sophisticated vessels for the challenging installation process and to protect moorings and anchors from the high loads during operation [15].

- *Ballast stabilized platforms*
  Spar platforms are the main ballast stabilized platforms, originally designed as buoys to gather oceanographic information and initially used by the oil and gas industry in the 1990s. Spar resembles a slender vertical cylinder, where stability is provided by heavy ballast at the lower extremity of the platform, shifting the center of gravity to below the center of buoyancy. Station keeping is provided by catenary mooring systems with or without taut lines [14]. This simple design has excellent stability and is amenable to serial fabrication processes, has few moving parts and does not require active ballast. On the contrary, turbine needs to be assembled offshore, which requires dynamic positioning vessels as well as heavy-lift cranes, whereas such structures are constrained to deep water locations. Moreover, the simplicity of the hull form makes the spar design susceptible to a phenomenon called vortex-induced vibrations (VIVs). As the cylinder heaves, it creates vortices that alter the pressure distribution along the surface, and the flow becomes irregular. This pressure change leads to low-frequency vortex-induced vibrations, causing higher mean current forces and leading to fatigue, a critical factor for the structure's operational robustness [15].

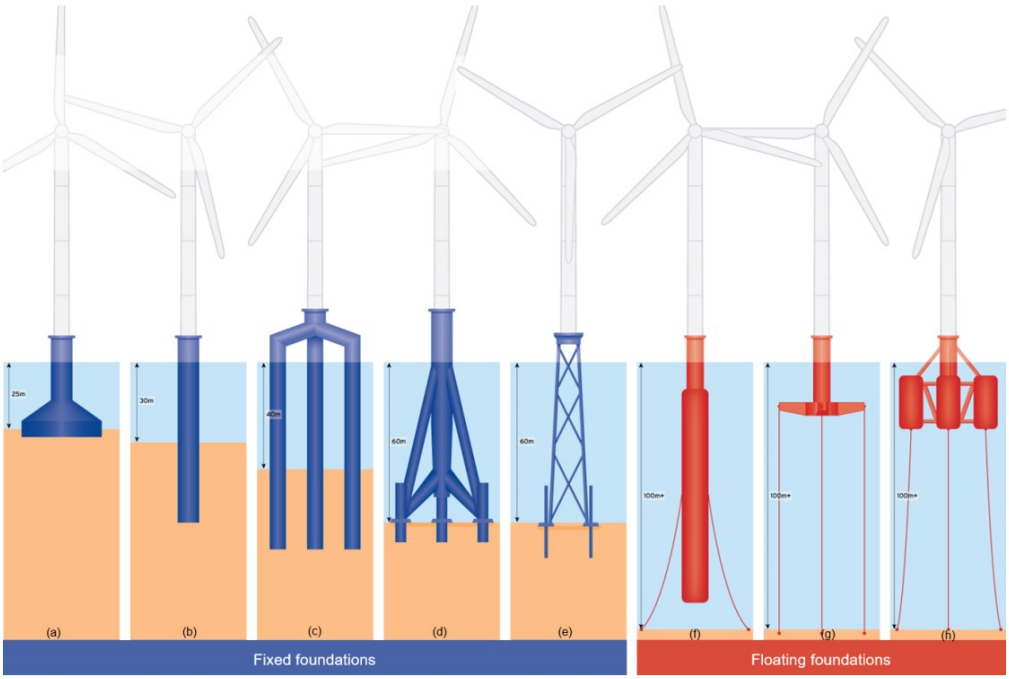


Figure 1.1: Offshore wind foundations; Fixed-bottom: (a) Gravity-based, (b) Monopile, (c) Tripile, (d) Tripod, (e) Jacket. Floating: (f) Spar, (g) TLP, (h) Semi-submersible. Source: [16]

Depending on the structure, its operation as well as the bathymetric conditions of the installation site, mooring systems can be divided in three main categories; tension-leg, taut-leg and catenary systems. The first mooring system type comprises of vertical tubular lines made of high-strength steel, which achieve station-keeping via very high pretension. The other two types are almost similar, apart from the fact that a part of a catenary line lies on the seabed. The taut-leg concept can be applied in a more vertical manner along with higher pretension on the line and thus to deeper waters, whereas a catenary mooring system requires longer lines, is less stiff regarding station-keeping and often used in shallower depths. TLPs and taut-leg moorings are governed by simplified dynamics and minimal wave loading, however, expensive anchors are required to withstand the great vertical loads and may not be effective solutions to depths less than 50 m. On the other hand, catenary mooring systems require low-cost anchors and can be deployed in shallow waters, but show complex dynamics leading to ballast needs for restricting excessive platform motions [17]. Simplified designs are shown in Fig. 1.2, where one can also see a concept with additional buoys on the catenary lines (Fig. 1.2d) that can be utilized for further stability requirements.

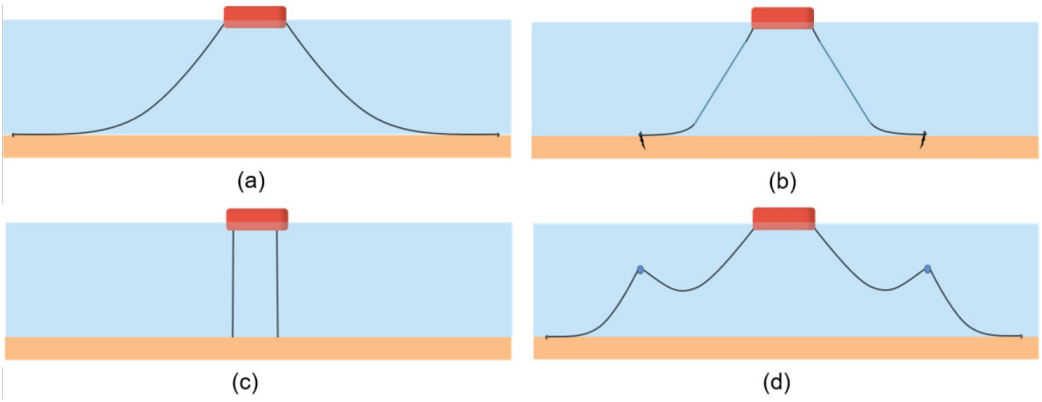


Figure 1.2: Moorings: (a) Catenary system, (b) Taut-leg system, (c) Tension-leg system and (d) Catenary system with intermediate buoys. Source: [16]

There are also concepts that aim to integrate other forms of energy (such as wave) into a single system, through multi-purpose floating structures, or to integrate multiple turbines together on a single platform [14]. Multiple-turbine floaters can share anchors and provide wave stability and mass optimization possibilities, yet they are highly costly and require complex yaw control. On the contrary, single-turbine floaters, except for the individual anchor costs, are simpler to manufacture, have lower structural requirements and standard yaw control options. Regarding the anchoring system costs, it depends on the type and material cost of the anchor and on the installation. Seafloor anchors consist of different types such as gravity-based, driven piles, drag-embedded as well as suction anchors and more, with use in several offshore works depending on the functionality i.e., permanent or deep-water installations, maximum pull-out loads etc. Additional costs are added due to the materials of mooring lines, which can be made of chains, steel wire or synthetic ropes or steel pipes [17]. A more comprehensive review on offshore wind foundations, substructure categories, mooring systems and anchors can be found in [15, 18].

The use of a floating base structure for a wind turbine has currently allowed for operating depths of 100 m based on the current level of technology maturity. The spar floating wind turbines can be regarded as the most technically mature, and a known challenge relates to the cost-effective assembly in open seas. The semi-submersible floating wind turbines have a relatively converged installation solution because of their good towability. TLPs are the least commercialized, and many concepts face installation challenges because of the platform stability issue and the complex anchoring systems. Further challenges exist also on the installation of the wind turbine components, as well as on the assembly procedures and the phases of marine operations [13, 19]. Additional future challenges include the development of

improved construction materials to reduce the mass of the increasing size of turbines, improved analysis techniques for the combined wind and wave loading present on FOWT installations, the adaption of current manufacturing techniques to improve the performance of large components, such as turbine blades, as well as the optimization of the power cabling connections to reduce the large costs associated with the long lengths needed for deep water offshore operations. The development of innovative solutions can reduce the operational and maintenance costs associated with the remote operation of these systems and enable cost reductions up to 50% [20]. A particular attention must be also paid to mooring line fracture as they are especially vulnerable to extreme sea conditions, resulting in fatigue, corrosion, impact damage, and further risks. Electrical failures are amongst the most significant errors of FOWT as well, with corrosion being the most common cause. It is technically possible to deploy FOWT in depth of over 200 m but mooring line, foundation support, deployment, installation and maintenance costs will rise and hence, making these projects financially feasible is a top priority for competitiveness in the energy market [21].

## 1.4 Research and Development of FOWTs

Over the last two decades, numerous concepts and projects have been studied and tested in order to develop not only the most efficient and robust structures for exploiting offshore wind, but also the adequate software tools and the specific experiment scenarios to validate the theoretical background of such complex analyses. The National Renewable Energy Laboratory (NREL) in the U.S., in cooperation with the MIT, have studied various designs that encompass the NREL 5-MW offshore baseline wind turbine. A complete analysis of static and coupled dynamics of floating wind turbine systems have been conducted with linear theory and standard tools (FAST & WAMIT software) exploring the effects of coupling the wind turbine with the floating platform, the effects of water depth, and the effects of wind speed on the systems' performance. Two floater concepts have been studied, a TLP and a barge, that may be deployed in offshore environments with water depths of 10 to 200 m, while it is also considered that both designs are statically stable in their non-moored condition, which allows them to be assembled at a near shore facility and towed to the offshore site. It was concluded that both systems demonstrated acceptable motions and had estimated costs of $\$1.4 - \$1.8$ million, not including the cost of the wind turbine, the power electronics, or the electrical transmission [22]. Additional examinations were later conducted in terms of mooring system types, comparing TLP

designs with catenaries, through a pareto optimal approach, where parameters were optimized without negative changes to other factors [23]. Given the fact that the floating wind turbines show increased loads on turbine components as compared to the land-based systems, four FOWT concepts were analyzed in terms of strength and response for ultimate loads as well as fatigue, using FAST software which performs coupled hydro-aero-elastic analyses [24]. The loads in the turbine supported by the barge were found to be the highest, whereas the differences in the loads between the TLP, the semi-submersible, and the spar buoy were not significant, except for the loads in the tower, which were greater in the spar and semi-submersible systems [25]. Regarding a different mooring system approach, a single-point mooring (SPM) system has been investigated in terms of the weathervane performance of a spar and a semi-submersible platform, concluding that the SPM-semi-submersible FOWT is acceptable in all the examined cases, while the one of the SPM-spar FOWT is acceptable when there are no currents [26].

Apart from the numerical analyses, scaled models have been also fabricated for validation purposes. At the Maritime Research Institute Netherlands (MARIN), experiments were performed regarding the three of the aforementioned platform types except for the barge concept, using a wave environment that represents the offshore area of the state of Maine, to generate data on coupled motions and loads for the operational, design, and survival sea-states [27]. Similar experiments have been also performed in Japan universities [28]. Further scientific material on validation can be found in reports of projects such as OC4-DeepCWind and OC5, where a semi-submersible platform with catenary moorings has been investigated and a full-scale model is tested in MARIN tanks under open-ocean conditions [29, 30]. More work on these designs has been done regarding the solution of the potential flow and how it is affected with decreasing bathymetry as well as motion evaluation under irregular waves [31, 32]. Coupled aero-hydro-servo-elastic simulations and model tests have been also compared in more sophisticated floaters such as the GustoMSC Tri-Floater [33], WindFloat [34], as well as a V-shaped braceless semi-submersible platform (Fig. 1.3) supporting either the NREL 5-MW or a 7-MW wind turbine, planned of being installed 20 km offshore Fukushima, Japan [35, 36].


Figure 1.3: Floating platform concepts: (a) GustoMSC Tri-Floater, (b) WindFloat and (c) V-shaped braceless semi-submersible. Source: Respective literature.

Additional projects can be found in literature encompassing machines with greater rated power. The European project LIFES50+ has studied two floating substructures for the DTU 10-MW reference wind turbine, i.e., the LIFES50+ OO-Star Wind Floater semi-submersible and the NAUTILUS-10 semi-submersible (Fig. 1.4), both equipped with a catenary mooring system capable of being installed in water depths up to 130 m [37]. The NAUTILUS-10 design has been also investigated under turbulent wind and irregular waves representing conditions at the Gulf of Maine, in order to study its hydrodynamic characteristics and its mooring dynamics [38]. A technical report by SINTEF presented recently the INO WINDMOOR 12-MW floating wind turbine that consists of a semi-submersible platform with a catenary mooring

system [39], whereas an innovative design with similar moorings, the TetraSpar (Fig. 1.4), has been developed capable of accommodating turbines in the 15-MW+ scale. According to the authors, the TetraSpar design brings a milestone and can be characterized as a modular and fully industrialized foundation that consists of components already widely available in the current wind energy supply chain, and thus capable of reducing significantly the costs in the field of FOWT [40]. About a decade ago though, the Vertiwind project was introduced, a breakthrough solution with the similar goal of cost reduction for offshore floating wind applications, based on the use of a vertical axis wind turbine (VAWT) that offers a much lower center of gravity than the more standard horizontal axis wind turbine concepts (Fig. 1.4) [12]. Similar design supporting a VAWT is also the DeepWind, which alongside with the HyWind and WindFloat projects have been compared, both in terms of technical solution and in maturity [41].

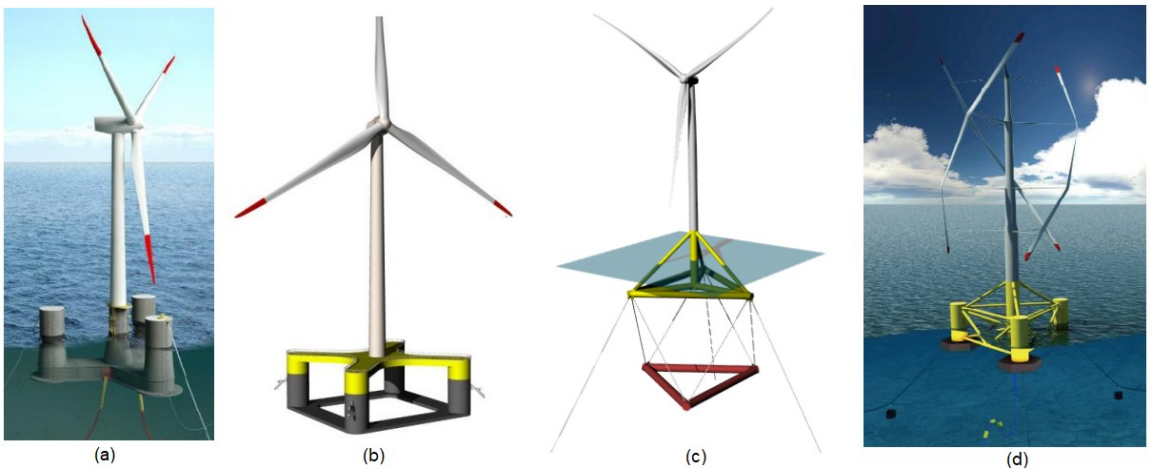


Figure 1.4: FOWT projects: (a) LIFES50+ OO-Star Wind Floater, (b) NAUTILUS-10, (c) TetraSpar and (d) Vertiwind. Source: Respective literature.

The continuous will for developing hybrid systems, has made scientific community to integrate wave energy converters (WECs) in FOWT designs. Despite the large variation in designs and concepts, WECs can be classified into three predominant types, attenuators, point absorbers and terminators, depending on how they interact with waves and how they are positioned upon them. Within these categories, there is a further level of classification, determined by their mode of operation. Examples are overtopping devices, oscillating water column devices (OWCs), submerged pressure differential devices among others [42]. However, OWCs are the most common in hybrid designs (see e.g., the REFOS system [43, 44]), were the first concept for

wave energy conversion to be developed and are still the favorite technology among a large part of the wave energy conversion community. Large scale testing began in the late 1970s, but accelerated efforts on research were witnessed in the early 1990s and beyond, with various concepts such as fixed-structure, floating-structure and breakwater-integrated OWCs. As far as principle of operation is concerned, in an OWC there is a fixed or floating hollow structure, open to the sea below the water surface, that traps air above the inner free-surface. Wave action alternately compresses and decompresses the trapped air, which is forced to flow through a turbine coupled to a generator that produces energy. These air turbines are constantly under optimization and play the key role for an effective OWC with efficient operation in almost every sea-state [45].

Despite the fact that FOWTs are in the path of becoming competitive in the energy market bearing in mind that they are extensively developed, tested and validated, it is critical to further improve cost-wise factors. A multi-objective genetic algorithm has been developed to represent an entire design exploration and optimal points, considering TLP, spar and semi-submersible platform types with a wide range of floater configurations. A combination of cost and dynamic models was used to define the economic and engineering performance of the platforms. TLPs and semi-submersibles with three outer cylinders were shown to be the best options below a cost of $4.5 million [46]. Extensive study on costs has been also conducted recently, regarding the Mediterranean Sea, based on factors that affect the levelized cost of energy (LCOE) from floating offshore wind. The LCOE depends on capital expenditures, spent prior to the functioning of the energy farm (CAPEX), operational expenditures, related to the operation and maintenance (OPEX), as well as annual energy production (AEP). The multi-parameter analysis showed that the main site-specific variable controlling the LCOE was the energy production, which depends on the spatial variability of the wind resource. Although the costs are greatly influenced by the distance to shore and secondarily by water depth, this effect is overshadowed by the local wind conditions [47].

## 1.5 Objectives and Outline

The aim of this study is to describe the methodology for an extreme value analysis of wind and wave parameters at three specific locations in the Greek seas that are known to be advantageous in terms of joint power production and bathymetric conditions. The analysis is applied to a multi-purpose floating platform suitable for joint

offshore wind and wave energy exploitation, in order to determine the designated range of environmental conditions at the installation sites and its power efficiency comparing two different mooring systems.

The remainder of this thesis consists of four more chapters. In Chapter 2, the extreme value analysis of metocean parameters is presented using the Peak-Over-Threshold (POT) method, while the choice procedure of the most promising locations in the Aegean Sea is also demonstrated. Chapter 3 deals with the design of a catenary mooring system for a multi-purpose floating structure, along with the formulation of the hydrodynamic problem, the coupled hydro-aero-elastic analysis and the structure's responses comparing the designed and the initial mooring system. In Chapter 4, offshore wind and wave energy potentials are calculated and compared for the three selected locations, while the efficiency between catenaries and pre-tensioned tethers on the power production is also compared and discussed. The thesis closes with Chapter 5, where the main conclusions of this study are reported along with recommendations for further research on the examined topics.

# Chapter 2

# Extreme Value Analysis

## 2.1 Introduction

Even from the first stages of an engineering project, the knowledge of critical parameters and their potential extreme values is of utmost importance for the robustness and efficiency of the final result. The determination of these extreme values can be done statistically through the methodologies from extreme value analysis (EVA). Such studies are also frequently conducted in the fields of economics, hydrology and physics; however, the focus will be spotted on variables that are more common in meteorology and oceanography like wind and wave parameters. As far as data source is concerned, reanalysis data have several advantages compared to in-situ measurements. The acquired time series are continuous, the sampling intervals are constant and they are usually of long duration, in contrast to in-situ measurements or satellite data that are usually temporally limited. Hence, discrepancies in the results can occur, depending on the data source. For example, effects of alternative wind data sources on the wind climate analysis in four locations across the Aegean Sea have been examined, using the Error-In-Variables approach to analyze and calibrate satellite and model wind data, taking as reference buoy measurements [48].

In literature, one can find a plethora of EVA that serve many purposes. For instance, global trends in the extreme values of significant wave heights ($H_s$) and wind speeds ($U_w$) have been presented using the ERA-40 dataset, estimating also the 100-year return periods [49], while similar EVA for $H_s$ has been performed in the North Atlantic Ocean [50]. In the latter, a regional frequency analysis on different datasets from different climate scenarios allowed the comparison and assessment of the potential effect of climate change on the ocean wave climate. Regarding Europe,

extreme $H_s$ have been evaluated for 20-, 50- and 100-year return periods for the Adriatic Sea, based on WorldWaves database (1992–2016), developing wind and wave statistical models that take into account joint distributions of significant wave height with peak wave period ($H_s - T_p$) and wind speeds ($H_s - U_w$). Such data can be useful for the design, risk-based operation planning, lifetime extension and maintenance of new and existing seagoing vessels and offshore installations [51]. In general, design parameters corresponding to environmental loads implied by wind, waves, etc., are used in practice to evaluate the resistance of an offshore structure in the ultimate limit state, whereas the accurate estimation of design values greatly facilitates the analysis of different serviceability limit states and fatigue. In this respect, a bivariate EVA of wind and waves can produce 50- or 100-year return forces that would be experienced by a typical offshore system. Similar analysis has been performed estimating the 50-year mooring force of a moored semi-submersible, along with return period contours that indicate the likely combinations of wind and wave, which could give rise to the 50-year condition [52].

Regarding EVA methods, the most widely used are the Block Maxima (BM) and the Peaks-Over-Threshold (POT). In order to implement the BM method, the grouping of data into blocks of equal length and the selection of the maximum of each block is required. According to the main theoretical result of EVA, these maxima follow asymptotically the Generalized Extreme Value (GEV) distribution. On the other hand, using the POT method presupposes the selection of a threshold above which all values are considered extreme. A comparison of both methods has been performed for real wind speed data and the effects of sample size and GEV distribution parameter estimation methods are discussed [53, 54]. More applications regarding the estimation of metocean extremes can be found in references therein. Similar study has been conducted for the offshore Colombian Caribbean Sea, where a 24-year dataset of Cross-Calibrated Multi-Platform (CCMP) winds and a 35-year dataset of ERA-Interim significant wave heights were analyzed via BM method, POT method and the Method of Independent Storm (MIS) [55]. Further applications of the POT method can be found both regionally e.g., with $H_s$ data of Figueira da Foz, Portugal [56] and globally for ocean wind speed and $H_s$, estimating 100-year return periods from a 46-year ERA-40 dataset [57]. POT method has been used also for estimation of long-term trends in the frequency and intensity of severe storm waves [58], as well as for developing extremes' modelling, capturing both short- and long-range correlations with a fitted ARFIMA model [59].

## 2.2 Peaks-Over-Threshold Method and Model Diagnostics

In this section, the Peaks-Over-Threshold method as well as model diagnostics will be presented according to the book of Coles [60]. In a case that, for example, hourly or daily observations are available, it is better to avoid the procedure of blocking and utilize all the data for an EVA by selecting an appropriate threshold above which reliable results can rise. This approach contrasts with the block maxima approach through the characterization of an observation as extreme if it exceeds a high threshold.

Supposing that a proper and large threshold $u$ is defined, the distribution function of the exceedance $y = (X - u)$, where $X > u$ is an arbitrary term of the examined sequence, is approximately:

$$H(y) = 1 - \left(1 + \frac{\xi y}{\tilde{\sigma}}\right)^{-\frac{1}{\xi}} \tag{2.1}$$

defined on $\{y : y > 0 \text{ and } (1 + \xi y/\tilde{\sigma}) > 0\}$, where $\tilde{\sigma}$ and $\xi$ are the scale and shape parameters respectively. If $\xi < 0$ the distribution of excesses has an upper bound of $u - \tilde{\sigma}\xi$; if $\xi > 0$ the distribution has no upper limit. The distribution is also unbounded if $\xi = 0$, which should again be interpreted by taking the limit $\xi \to 0$ in Eq. (2.1), leading to

$$H(y) = 1 - exp\left(-\frac{y}{\tilde{\sigma}}\right), \quad y > 0 \tag{2.2}$$

corresponding to an exponential distribution with parameter $1/\tilde{\sigma}$. The family of distributions defined by Eq. (2.2) is called the generalized Pareto family and the excesses are considered to be independent and identically distributed (IID) variables.

As mentioned above, all sample points exceeding a defined threshold are separated from the rest of the data for further analysis (i.e., modeled as a generalized Pareto distribution). The main challenge at this stage, however, is to choose a threshold that balances bias and variance. Too low a threshold is likely to violate the asymptotic basis of the model, leading to bias, whereas too high a threshold will generate few excesses with which the model can be estimated, leading to high variance. In this context, two methods are available for this purpose: one is an exploratory technique carried out prior to model estimation; the other is an assessment of the stability of parameter estimates, based on the fitting of models across a range of different thresholds. In more detail, regarding the first one, theory suggests that when the

generalized Pareto distribution is appropriate, the sample mean of the threshold excesses of $u$ changes linearly with $u$. This leads to the mean residual life (MRL) plot, which constitutes the locus of points

$$\left\{ \left( u, \frac{1}{n_u} \sum_{i=1}^{n_u} (x_{(i)} - u) \right) : u < x_{max} \right\} \tag{2.3}$$

where $x_{(1)}, \ldots, x_{(n_u)}$ consist of the $n_u$ observations that exceed $u$, and $x_{max}$ is the largest of the $x_i$. Above a threshold $u_0$ at which the generalized Pareto distribution provides a valid approximation to the excess distribution, the MRL plot should be approximately linear in $u$. Common practice is also the depiction of confidence intervals at a certain confidence level in the MRL plot calculated as:

$$\pm\, z_{score}(confid.\, level) \cdot \frac{Var(y_u)}{\sqrt{n_u}} \tag{2.4}$$

where $Var(y_u)$ and $n_u$ are the variance and the number of the excesses respectively based on a threshold $u$.

The second procedure for threshold selection is to estimate the model at a range of thresholds. Above a level $u_0$ at which the asymptotic motivation for the generalized Pareto distribution is valid, estimates of the shape parameter $\xi$ should be approximately constant, while estimates of $\sigma_u$ should be linear in $u$, based on the relation for $u > u_0$,

$$\mathrm{E}(X - u \mid X > u) = \frac{\sigma_u}{1 - \xi} = \frac{\sigma_{u_0} + \xi u}{1 - \xi} \tag{2.5}$$

A complementary technique is to fit the generalized Pareto distribution at a range of thresholds, and to look for stability of parameter estimates. This argument suggests plotting both $\sigma^* = \sigma_u - \xi \cdot u$ (modified scale) and $\xi$ estimates against $u$, together with confidence intervals for each of these quantities, and selecting $u_0$ as the lowest value of $u$ for which the estimates remain near-constant. The confidence intervals for $\hat{\xi}$ are obtained immediately from the variance-covariance matrix as

$$\pm\, z_{score}(confid.\, level) \cdot \sqrt{Var(\hat{\xi})} \tag{2.6}$$

while the ones for $\hat{\sigma}^*$ require the delta method for the variance, using

$$\mathrm{Var}\,(\sigma^*) \approx \nabla {\sigma^*}^T V \nabla \sigma^*, \quad \text{where} \quad \nabla {\sigma^*}^T = \left[ \frac{\partial \sigma^*}{\partial \sigma_u}, \frac{\partial \sigma^*}{\partial \xi} \right] = [1, -u] \tag{2.7}$$

Having determined a threshold, the parameters of the generalized Pareto distribution can be estimated by Maximum Likelihood (ML). The ML method is unbiased, consistent and asymptotically efficient, but becomes biased for small samples and may not provide a global optimum, when the likelihood function is arbitrarily large. In general, an ideal estimate should be unbiased, efficient and consistent. The expected value of an unbiased estimator equals the true parameter value, while an efficient estimator provides a minimal mean square error. Furthermore, an estimator is consistent if it converges with probability one to the real parameter, as the sample size tends to infinity [53]. The principle of maximum likelihood estimation is to adopt the model with greatest likelihood. Since of all the models under consideration, this is the one that assigns highest probability to the observed data. In greater detail, referring back to the situation in which $x_1, \ldots, x_n$ are independent realizations of a random variable having probability density function $f(x; \theta_0)$, the likelihood function is:

$$L(\theta) = \prod_{i=1}^{n} f\left(x_i; \theta\right) \tag{2.8}$$

Denoting the density function of $X_i$ by $f_i(x_i; \theta)$, we obtain

$$L(\theta) = \prod_{i=1}^{n} f_i\left(x_i; \theta\right) \quad \text{and} \quad \ell(\theta) = \sum_{i=1}^{n} \log f_i\left(x_i; \theta\right) \tag{2.9}$$

as it is often more convenient to take logarithms and work with the log-likelihood function. More generally still, if $\mathcal{F} = \{f(x; \theta) : \theta \in \Theta\}$ denotes a family of joint probability density functions for a set of (not necessarily independent) observations $x = (x_1, \ldots, x_n)$, then the likelihood is $L(\theta) = f(x; \theta)$, regarded as a function of $\theta$ with $x$ fixed at the observed value. The maximum likelihood estimator $\hat{\theta}_0$ of $\theta_0$ is defined as the value of $\theta$ that maximizes the appropriate likelihood function.

In offshore and coastal engineering applications, the concept of return period and design value is widely used. The formal definition of the return period implies that the design value is expected to be exceeded on average once during the next n years. The period of n years is called return period, associated with the design value. Assuming as $\zeta_u$ the exceedance probability or the proportion of data above a threshold $u$, the N-year return level $z_N$ can be written as

$$z_N = u + \frac{\sigma}{\xi}\left[\left(N n_y \zeta_u\right)^{\xi} - 1\right] \tag{2.10}$$

where $n_y$ the exceedance observations per year, or

$$z_N = u + \sigma \log\left(N n_y \zeta_u\right) \tag{2.11}$$

when $\xi = 0$. Standard errors or confidence intervals can be derived again by the delta method. From standard properties of the binomial distribution, $Var(\hat{\zeta_u}) \sim \hat{\zeta_u} \cdot (1 - \hat{\zeta_u})/n$, so the complete variance-covariance matrix for $(\hat{\zeta_u}, \hat{\sigma}, \hat{\xi})$ is approximately

$$V = \begin{bmatrix} \hat{\zeta}_u \left(1 - \hat{\zeta}_u\right)/n & 0 & 0 \\ 0 & v_{1,1} & v_{1,2} \\ 0 & v_{2,1} & v_{2,2} \end{bmatrix} \tag{2.12}$$

where $v_{i,j}$ denotes the $(i, j)$ term of the variance-covariance matrix of $\hat{\sigma}$ and $\hat{\xi}$.

Lastly, probability (PP) and quantile (QQ) plots are useful for further assessing the quality of the fitted generalized Pareto model. For a threshold $u$, threshold excesses $y_{(1)} \leq \ldots \leq y_{(n)}$ and an estimated model $\hat{H}$, the probability plot consists of the pairs

$$\left\{ \left( i/(k+1), \hat{H}\left(y_{(i)}\right) \right); i = 1, \ldots, k \right\} \quad \text{where} \quad \hat{H}(y) = 1 - \left(1 + \frac{\hat{\xi} y}{\hat{\sigma}}\right)^{-1/\hat{\xi}} \tag{2.13}$$

while the quantile plot constitutes the locus of points

$$\left\{ \left( \hat{H}^{-1}(i/(k+1)), y_{(i)} \right), i = 1, \ldots, k \right\} \quad \text{where} \quad \hat{H}^{-1}(y) = u + \frac{\hat{\sigma}}{\hat{\xi}} \left[ y^{-\hat{\xi}} - 1 \right] \tag{2.14}$$

provided that $\hat{\xi} \neq 0$. If $\hat{\xi} = 0$ the equations are appropriately modified using Eq. (2.2) and Eq. (2.1). At this stage, the model diagnostics are completed, and the model is adequately identified, provided that both plots depict a very close relation between theoretical and sample quantities.

In the work herein, the above methodology will be used for EVA of metocean data. However, short- and long-term clustering of extremes leads to deviations from the IID behavior. The significance of persistence when using POT method will not be examined, even though environmental parameters like wind and wave data, are governed by periodicity and have stochastic behavior. Further reading on the topic can be done in [60, 61].

## 2.3 Site Selection and Data

As it is already mentioned, offshore wind provides a more powerful source of energy than onshore wind. The differences between the two resources have been examined, showing offshore wind energy to be more even and available. Similar study in Fujian province of China has concluded that for the sake of economic feasibility and annual energy production, it is recommended to choose the hub heights of the selected wind turbine as 70 m and 40 m at the onshore site and offshore site, respectively [62]. Such fact emphasizes the power difference, if we keep in mind that the higher the altitude the greater the wind. In this context, the attention is drawn to the Mediterranean Sea. Studies have showed that in terms of LCOE, the lowest values are located in the Gulf of Lion and the Aegean Sea (approximately 95 €/MWh), where the wind resource is the best [47]. A study about the offshore wind power potential of the Aegean and Ionian Seas have been also conducted, examining the annual and inter-annual characteristics through a 15-year hindcast of wind data. Overall, it is concluded that offshore deep-water locations, especially in the Aegean Sea, are characterized by high values of offshore wind resource (mean annual wind power density up to 885 W/m$^2$ in the central Aegean) [63].

In this work, the aim is to perform an EVA in locations of the Aegean that are known to be advantageous in terms of both offshore wind and wave potentials as well as bathymetry. Due to the fact that the main concept is to install a multi-purpose floating structure to capture both wind and wave energy, the temporal relations between the two phenomena are also critical. Such study has been done for the Greek Seas in order to assess the complementarity and synergy between wind and wave and depict the most promising areas [64]. Via this analysis and with the help of EMODnet bathymetry map, three offshore locations were selected at approximately 200 m of water depth (Tab. 2.1). The first (L1) is east of Cyclades and south of Ikaria, the second one (L2) is between Kythira and Antikythira and the third site (L3) is located between Kasos and Karpathos (Fig. 2.1). The EVA will be performed in metocean parameters such as wind speed ($U_w$), significant wave height ($H_s$) and peak wave period ($T_p$). The slightly increased values in water depth will not affect the overall analysis, bearing in mind that the Aegean Sea has a relatively hilly seabed with steep bathymetry, deep waters and few subsea plateaus, making it challenging to find installation areas of constant depth.

Table 2.1: Coordinates and depth of the three examined locations.

| | Latitude | Longitude | Depth |
|---|---|---|---|
| Location 1 (L1) | 37.220° N | 26.115° E | 230 m |
| Location 2 (L2) | 35.964° N | 23.160° E | 208 m |
| Location 3 (L3) | 35.378° N | 27.038° E | 246 m |

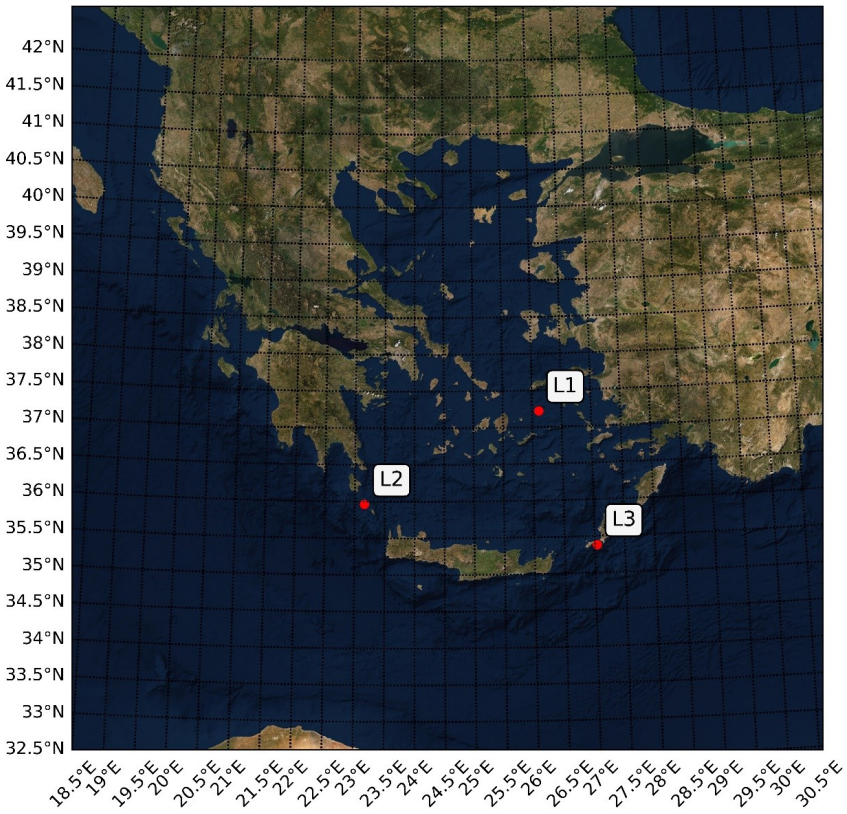


Figure 2.1: Selected locations in the Aegean Sea.

In order to perform an analysis with continuous and validated data, the ERA5 reanalysis dataset was chosen. Produced by the European Centre for Medium-Range Weather Forecasts (ECMWF), it combines vast amounts of historical observations into global estimates using advanced modeling and data assimilation systems. In this work 20 years (1 January 2000–31 December 2019) of available wind and wave data in an hourly temporal timestep were utilized for the Greek Seas (defined by a rectangle with the top left corner at 42° N, 19° E and bottom right corner at 33° N, 30° E). For the significant wave height and the wave energy period the data are provided on a 0.50° × 0.50° spatial grid, while for the wind speed, the data are available at 100 m height (i.e., at a typical wind turbine hub height) on a 0.25° × 0.25° spatial grid.

However, preparations have to be made in order to continue with the aforementioned POT method for the extremes. First of all, the ERA5 reanalysis dataset was spatially co-located with the selected locations via the nearby grid point values by using a simple form of inverse squared distance weighting interpolation function based on the values of the four nearest grid points. Denoting $x_1$, $x_2$, $x_3$ and $x_4$ the respective variables (wind or wave parameters) at the four grid points surrounding the selected location (Fig. 2.2 and 2.3), and $r_1$, $r_2$, $r_3$ and $r_4$ the corresponding distances from that location, the requested data for each variable at the specific site can be estimated as follows:

$$x = \frac{\sum_{i=1}^{4} \frac{x_i}{r_i^2}}{\sum_{i=1}^{4} \frac{1}{r_i^2}} \tag{2.15}$$

Regarding wave data, the ERA5 reanalysis dataset refer to the wave energy period $T_e$. Under the JONSWAP spectrum with a peak enhancement $g = 3.3$, $T_p$ and $T_e$ are approximately related as follows:

$$\frac{T_e}{T_p} \approx 0.9 \tag{2.16}$$

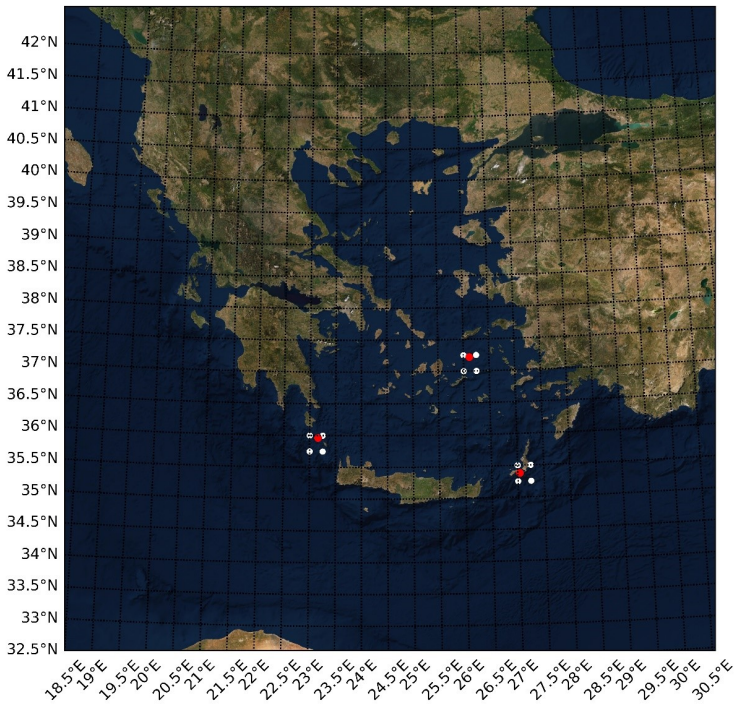


Figure 2.2: Examined locations (red) and neighboring grid points (white) of wind data.

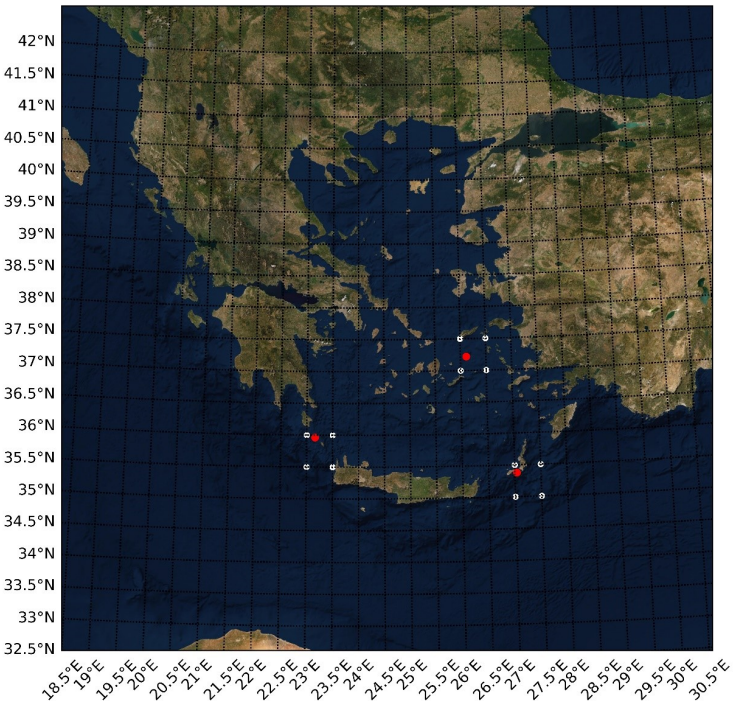


Figure 2.3: Examined locations (red) and neighboring grid points (white) of wave data.

Lastly, due to the fact that the third location is more surrounded by land, an additional verification for the respective wave parameters was performed, taking as reference highly grid dense data ($\sim$ 3.5 km spatial step) from the Copernicus Marine Environment Monitoring Service (CMEMS). Regarding wind, the process of co-location does not carry significant errors due to the continuous medium at the specific altitude, whereas as far as wave parameters are concerned, phenomena of discontinuity, refraction and shoaling can occur nearshore and thus display discrepancies in the data. For this verification, $H_s$ and $T_p$ data of equal length and similar timestep with ERA5 were utilized for the surrounding area of the third selected site in Kasos (L3). Again, no grid point matched and hence, an initial co-location of Copernicus data was done to adjust them at the site (L3) as well as at the four respective neighboring grid points of ERA5. Next, another similar procedure was performed that extracted the timeseries of L3 from the data that resulted from the previous step, concerning the four nearby ERA5 grid points. Subsequently, a regression line was plotted to depict the relation between the Copernicus results from co-located data and the ones purely from L3 (Fig. 2.4 and 2.5), in order to examine the aforementioned effects of land in the same data source with a fair approximation. Both $H_s$ and $T_p$ did not show great results, however, ERA5 co-located data for the examined site were fixed with the re-

spective equations of the regression lines to achieve at least even small improvements. The aforementioned data editing process, both modifications and verification, was performed via Matlab codes, while the maps were printed using Python. Relevant code scripts can be found in Appendix B.

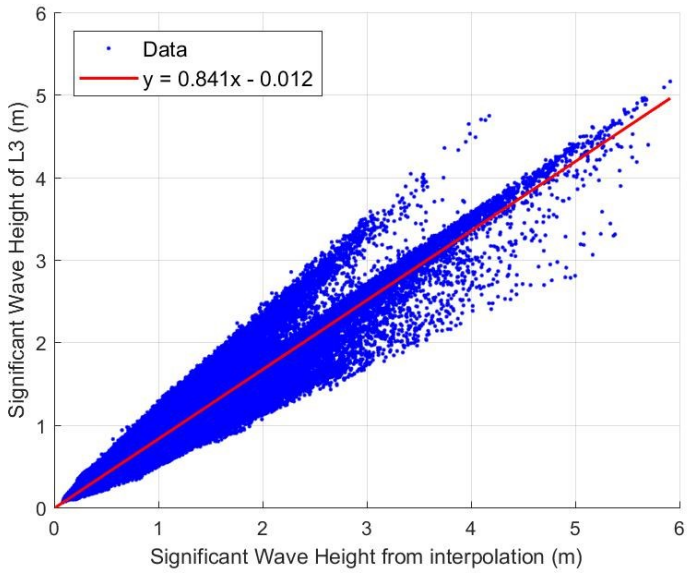


Figure 2.4: Linear regression for $H_s$ from Copernicus data.

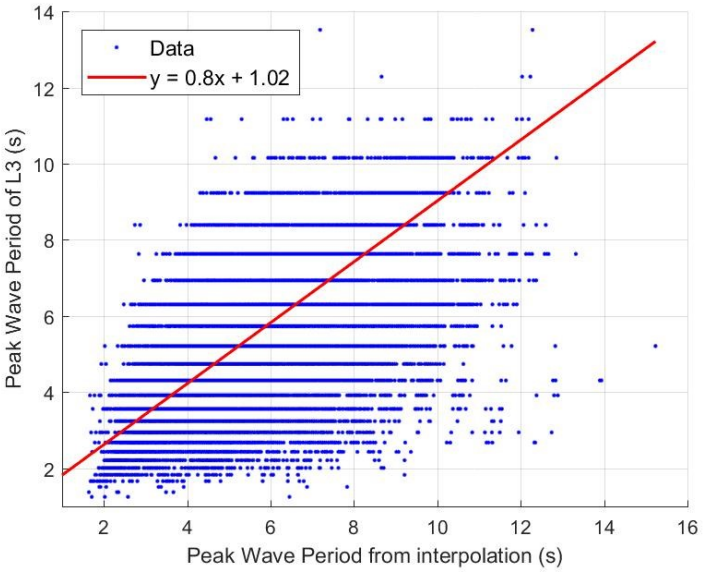


Figure 2.5: Linear regression for $T_p$ from Copernicus data.

## 2.4 Results

After the necessary modifications in the datasets described in Section 2.3 and based on the methodology presented in Section 2.2, an EVA on significant wave height ($H_s$), peak wave period ($T_p$) as well as wind speed at 100 m altitude ($U_w$) was performed for the three examined locations. The analysis was performed in Python based on a code script that follows exactly the procedures described in Section 2.2 [65]. It is noted that, although a proper procedure would be a bivariate analysis for the two wave parameters due to their correlation, the univariate one will be followed with the assumption that both variables can be examined separately. For a better insight and convenience of presentation, the plotted results of $U_w$ from the first location are presented to show the reliability of the method, while the rest can be found in Appendix A.

The first step of the analysis is to select a threshold, above which the data allow a reliable study for the behavior of the extremes. For that purpose, the mean residual life plot (Fig. 2.6) as well as the shape and modified scale parameter stability plots (Fig. 2.7 and 2.8) were used. As theory suggests, the threshold u should be spotted on the end of the linear part of the curve in the MRL plot and on the constant part of both stability plots. Regarding the first plot, it is initially approximately linear until $u \approx 13$, then it curves and returns to linearity for the part of u between 18 and 22. From this result and only, one can select a threshold of 15, 18, 20 or 22 without any concern about a false start. However, when stability plots are taken into account, above a threshold $u = 18$, the errorbars are significant and a problem of increased variance is on concern. Although a fair selection is a value of $u = 15$ as it meets all the aforementioned requirements, a little higher threshold was selected ($u = 17.5$) after trials, as it did not negate the variance prerequisites and showed great results that will be discussed below. Besides, such approach is in favor of safety when designing a project, since EVA results are utilized for robustness in ultimate limit states. Similar procedure was followed for all cases and the final thresholds are presented in Tab. 2.2.

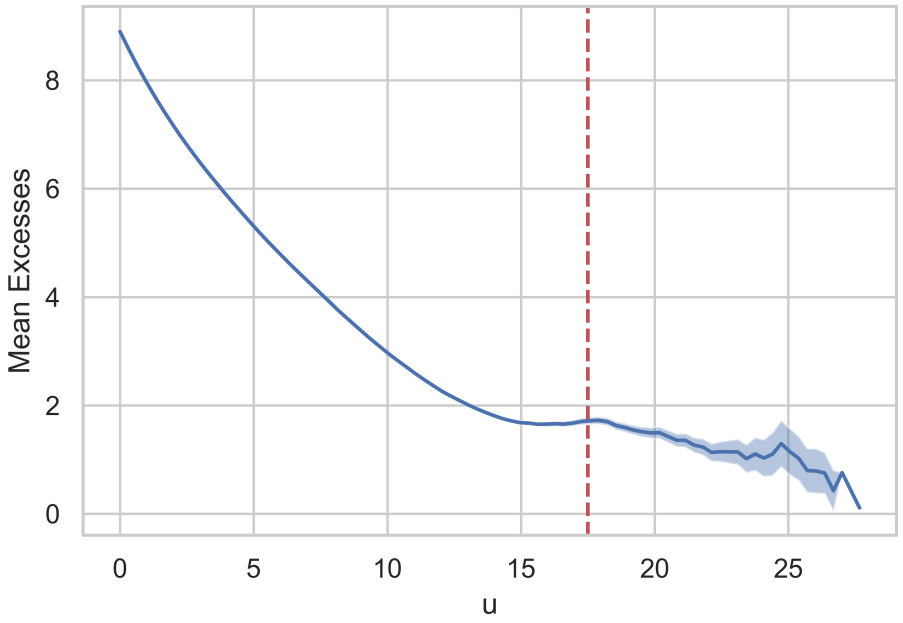


Figure 2.6: MRL plot with confidence bands of $U_w$ (m/s) for L1. Red line depicts the threshold selection.

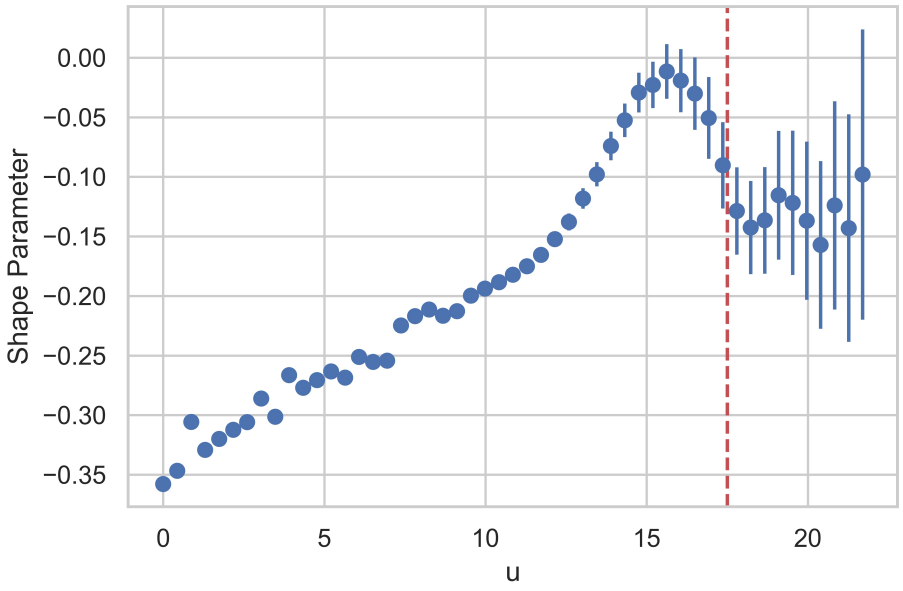


Figure 2.7: Shape stability plot with errorbars of $U_w$ (m/s) for L1. Red line depicts the threshold selection.

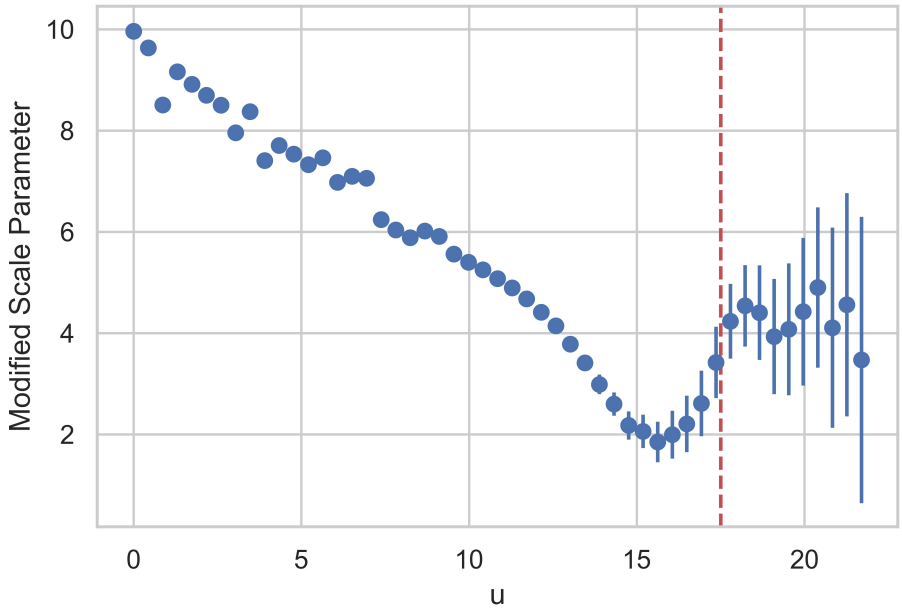


Figure 2.8: Modified scale stability plot with errorbars of $U_w$ (m/s) for L1. Red line depicts the threshold selection.

Table 2.2: Threshold selection for every examined variable and location.

| Variable | Ll | L2 | L3 |
|---|---|---|---|
| Uw (m/s) | 17.5 | 18.5 | 18 |
| $H_s$ (m) | 3 | 3.25 | 2.75 |
| $T_p$ (s) | 7 | 8.5 | 7 |

Coming back to the examined case, diagnostic plots for the fitted generalized Pareto model are shown in Fig. 2.9 to 2.12. None of the plots gives any real cause for concern about the quality of the fitted model, which supports the bias-variance trade-off. In particular, QQ and PP plots show great results regarding the relatively high selected threshold, as the data follow the regression line which states the similarity between theoretical and sample quantities. Furthermore, the return level plot illustrates also a goodness-of-fit between theoretical and empirical values, which lie inside the confidence bands without very large uncertainties that accrue once the model is extrapolated to higher levels. As far as statistical characteristics are concerned, the threshold $u = 17.5$ leads to 2655 exceedances in the series of length 175320, so $\zeta_u = 2655/175320 = 0.0151$. The maximum likelihood estimates of the generalized Pareto distribution parameters are $(\sigma, \xi) = (1.913, -0.111)$, with standard errors of 0.0508 and 0.0182 respectively. The 95% confidence interval of $\sigma$ is

[1.814, 2.013] and for $\xi$ is [-0.146, -0.075] calculated via the delta method and the complete variance-covariance matrix, which is shown in Tab. 2.4. The total statistics regarding estimates for all variables and locations can be found also in Tab. 2.4.

Having verified the successful threshold selection, an additional calculation was performed to extract return values for a number of return periods that appear in the design of both onshore and offshore projects. The errorbar equipped curve in Fig. 2.12 depicts the results for 20 to 100 years for the wind speed at L1, while the overall results are presented in Tab. 2.3 and the respective figures for every case are attached at Appendix A along with the rest of the diagnostic plots. Lastly, it is easily noticeable the fact that in Location 3 the return levels of the wave parameters are inferior compared to the other sites due to the presence of land nearby, whereas the opposite occurs for wind speed and Location 1, as the region is not only more open and lacks near highland, but also hosts both strong winter and summer winds (Etesian winds).

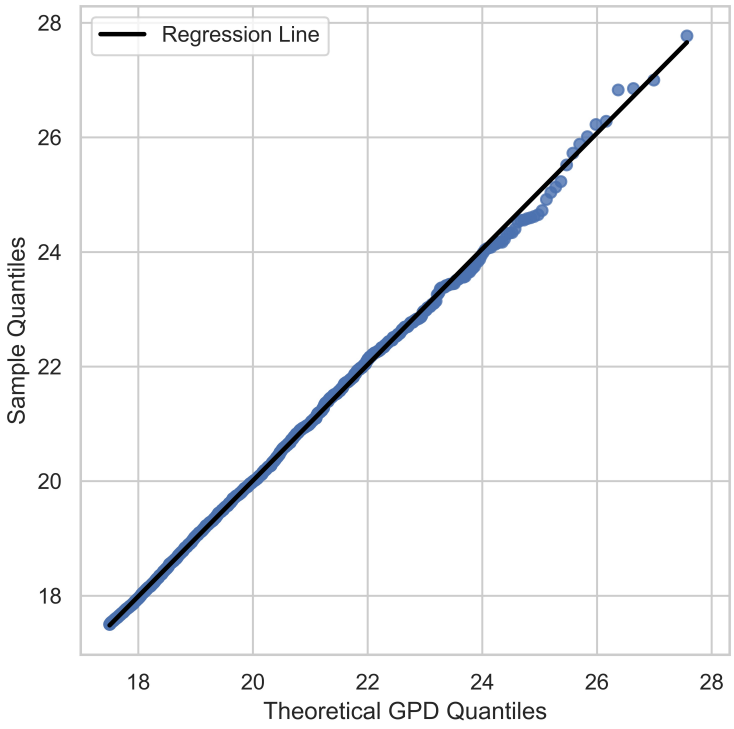


Figure 2.9: QQ plot of $U_w$ for L1.

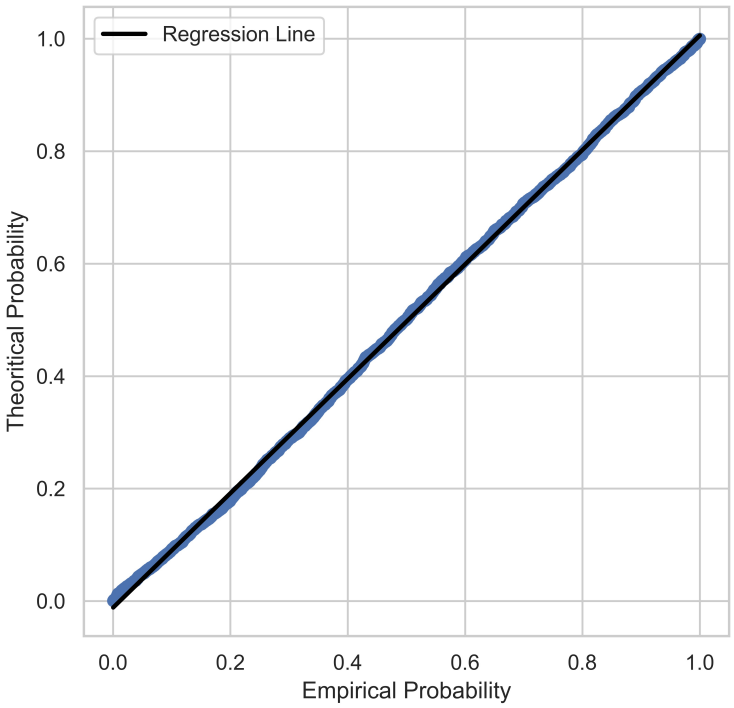


Figure 2.10: PP plot of $U_w$ for L1.

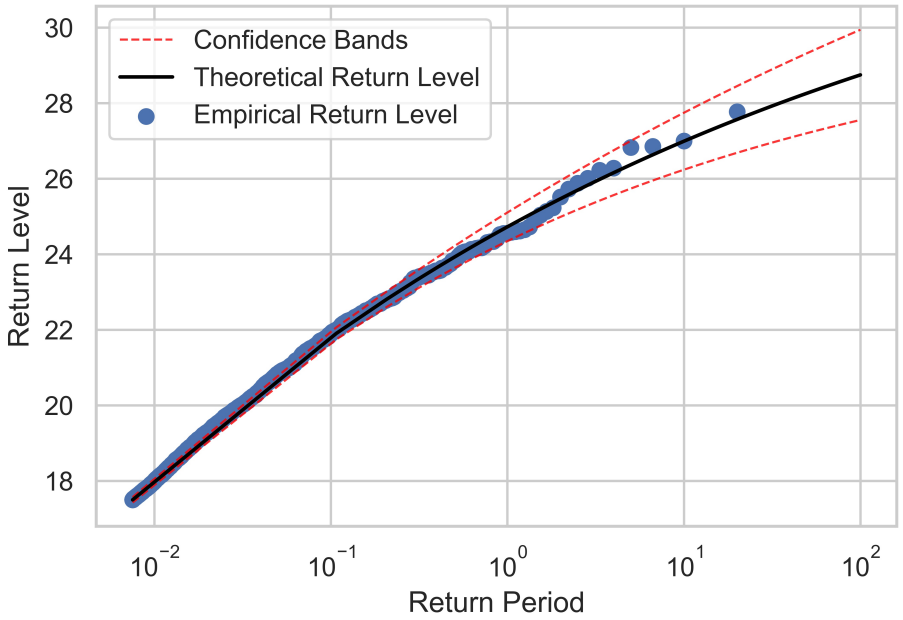


Figure 2.11: Return level plot with confidence bands of $U_w$ for L1.

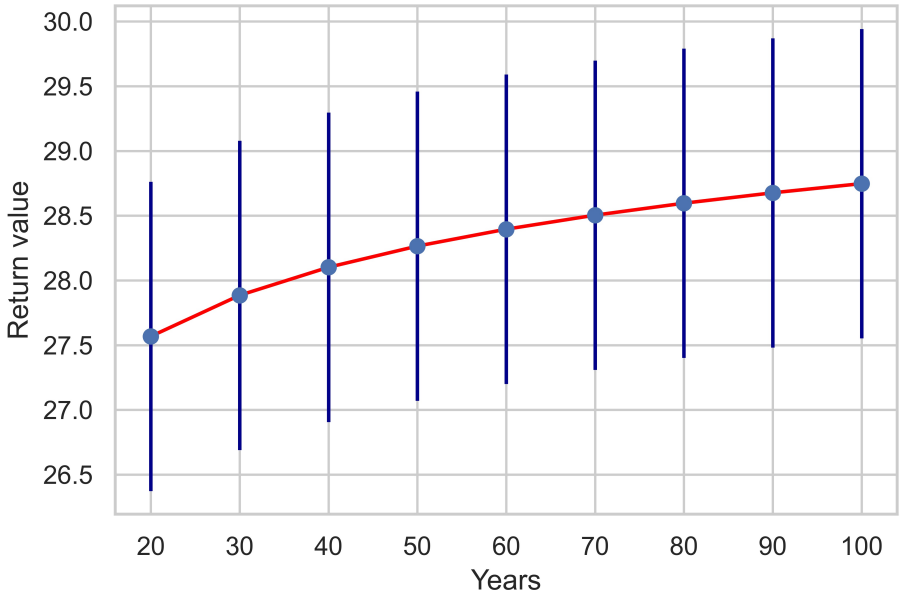


Figure 2.12: Return values curve with errorbars of $U_w$ for L1.

Table 2.3: Return values and 95% confidence intervals of the three examined variables referring to the three presented locations.

| $U_w$ (m/s) | Location 1 | | Location 2 | | Location 3 | |
|---|---|---|---|---|---|---|
| Years | Ret. Level | 95% Conf. Int. | Ret. Level | 95% Conf. Int. | Ret. Level | 95% Conf. Int. |
| 20 | 27.57 | [26.69, 28.45] | 26.51 | [25.89, 27.12] | 24.20 | [23.61, 24.80] |
| 30 | 27.88 | [26.93, 28.85] | 26.67 | [26.01, 27.32] | 24.37 | [23.72, 25.01] |
| 40 | 28.10 | [27.09, 29.12] | 26.77 | [26.09, 27.46] | 24.48 | [23.79, 25.16] |
| 50 | 28.27 | [27.21, 29.32] | 26.85 | [26.14, 27.56] | 24.56 | [23.85, 25.27] |
| 60 | 28.40 | [27.30, 29.49] | 26.91 | [26.18, 27.64] | 24.62 | [23.89, 25.35] |
| 70 | 28.50 | [27.38, 29.63] | 26.96 | [26.22, 27.71] | 24.67 | [23.92, 25.42] |
| 80 | 28.60 | [27.45, 29.75] | 27.00 | [26.24, 27.76] | 24.72 | [23.95, 25.48] |
| 90 | 28.68 | [27.50, 29.85] | 27.04 | [26.27, 27.81] | 24.75 | [23.97, 25.53] |
| 100 | 28.75 | [27.55, 29.94] | 27.07 | [26.29, 27.85] | 24.79 | [23.99, 25.58] |
| $H_s$ (m) | Location 1 | | Location 2 | | Location 3 | |
| Years | Ret. Level | 95% Conf. Int. | Ret. Level | 95% Conf. Int. | Ret. Level | 95% Conf. Int. |
| 20 | 6.01 | [5.63, 6.38] | 6.22 | [5.94, 6.50] | 4.43 | [4.33, 4.54] |
| 30 | 6.13 | [5.71, 6.54] | 6.31 | [6.01, 6.62] | 4.46 | [4.35, 4.58] |
| 40 | 6.21 | [5.77, 6.66] | 6.37 | [6.05, 6.70] | 4.48 | [4.36, 4.60] |
| 50 | 6.28 | [5.81, 6.74] | 6.42 | [6.09, 6.76] | 4.50 | [4.37, 4.62] |
| 60 | 6.33 | [5.84, 6.82] | 6.46 | [6.11, 6.81] | 4.51 | [4.38, 4.64] |
| 70 | 6.37 | [5.87, 6.87] | 6.49 | [6.13, 6.85] | 4.51 | [4.38, 4.65] |
| 80 | 6.41 | [5.89, 6.93] | 6.52 | [6.15, 6.89] | 4.52 | [4.39, 4.66] |
| 90 | 6.44 | [5.91, 6.97] | 6.54 | [6.17, 6.92] | 4.53 | [4.39, 4.66] |
| 100 | 6.47 | [5.93, 7.01] | 6.56 | [6.18, 6.94] | 4.53 | [4.40, 4.67] |
| $T_p$ (s) | Location 1 | | Location 2 | | Location 3 | |
| Years | Ret. Level | 95% Conf. Int. | Ret. Level | 95% Conf. Int. | Ret. Level | 95% Conf. Int. |
| 20 | 9.39 | [9.16, 9.61] | 11.74 | [11.48, 12.00] | 8.43 | [8.35, 8.52] |
| 30 | 9.46 | [9.21, 9.71] | 11.84 | [11.56, 12.12] | 8.45 | [8.36, 8.55] |
| 40 | 9.51 | [9.25, 9.77] | 11.90 | [11.61, 12.20] | 8.47 | [8.37, 8.56] |
| 50 | 9.55 | [9.28, 9.82] | 11.95 | [11.65, 12.26] | 8.48 | [8.38, 8.58] |
| 60 | 9.58 | [9.30, 9.86] | 11.99 | [11.67, 12.31] | 8.49 | [8.39, 8.59] |
| 70 | 9.60 | [9.31, 9.89] | 12.02 | [11.70, 12.35] | 8.49 | [8.39, 8.60] |
| 80 | 9.62 | [9.33, 9.92] | 12.05 | [11.72, 12.38] | 8.50 | [8.39, 8.60] |
| 90 | 9.64 | [9.34, 9.95] | 12.08 | [11.74, 12.41] | 8.50 | [8.40, 8.61] |
| 100 | 9.66 | [9.35, 9.97] | 12.10 | [11.75, 12.44] | 8.51 | [8.40, 8.61] |

Table 2.4: Statistical characteristics of model parameters estimation for every examined variable and location.

| $U_w$ (m/s) | Excesses | Proportion above ($\zeta$) | Estimates scale ($\sigma$) | Estimates shape ($\xi$) | Standard errors scale ($\sigma$) | Standard errors shape ($\xi$) | 95% confidence interval scale ($\sigma$) | 95% confidence interval shape ($\xi$) | Variance-Covariance matrix of ($\zeta$, $\sigma$, $\xi$) | | |
|---|---|---|---|---|---|---|---|---|---|---|---|
| | | | | | | | | | 8.48E-08 | 0 | 0 |
| L1 | 2655 | 0.0151 | 1.913 | -0.111 | 0.0508 | 0.0182 | $[1.814, 2.013]$ | $[-0.146, -0.075]$ | 0 | 0.0025782 | -0.007065 |
| | | | | | | | | | 0 | -0.007065 | 0.0003322 |
| | | | | | | | | | 5.26E-08 | 0 | 0 |
| L2 | 1623 | 0.0093 | 2.234 | -0.227 | 0.0744 | 0.0229 | $[2.088, 2.380]$ | $[-0.272, -0.182]$ | 0 | 0.0055332 | -0.0014122 |
| | | | | | | | | | 0 | -0.0014122 | 0.0005239 |
| | | | | | | | | | 4.92E-08 | 0 | 0 |
| L3 | 1517 | 0.0087 | 1.506 | -0.176 | 0.0540 | 0.0255 | $[1.400, 1.612]$ | $[-0.226, -0.126]$ | 0 | 0.0029184 | -0.0011195 |
| | | | | | | | | | 0 | -0.0011195 | 0.0006477 |

| $H_s$ (m) | Excesses | Proportion above ($\zeta$) | Estimates scale ($\sigma$) | Estimates shape ($\xi$) | Standard errors scale ($\sigma$) | Standard errors shape ($\xi$) | 95% confidence interval scale ($\sigma$) | 95% confidence interval shape ($\xi$) | Variance-Covariance matrix of ($\zeta$, $\sigma$, $\xi$) | | |
|---|---|---|---|---|---|---|---|---|---|---|---|
| | | | | | | | | | 5.53E-08 | 0 | 0 |
| L1 | 1726 | 0.0098 | 0.521 | -0.072 | 0.0183 | 0.0256 | $[0.485, 0.557]$ | $[-0.122, -0.022]$ | 0 | 0.0003351 | -0.0003625 |
| | | | | | | | | | 0 | -0.0003625 | 0.0006567 |
| | | | | | | | | | 7.65E-08 | 0 | 0 |
| L2 | 2392 | 0.0136 | 0.578 | -0.115 | 0.0166 | 0.0202 | $[0.545, 0.610]$ | $[-0.155, -0.076]$ | 0 | 0.0002742 | -0.0002612 |
| | | | | | | | | | 0 | -0.0002612 | 0.0004096 |
| | | | | | | | | | 5.42E-08 | 0 | 0 |
| L3 | 1686 | 0.0096 | 0.509 | -0.257 | 0.0161 | 0.0212 | $[0.477, 0.540]$ | $[-0.299, -0.216]$ | 0 | 0.0002591 | -0.0002852 |
| | | | | | | | | | 0 | -0.0002852 | 0.0004471 |

| $T_p$ (s) | Excesses | Proportion above ($\zeta$) | Estimates scale ($\sigma$) | Estimates shape ($\xi$) | Standard errors scale ($\sigma$) | Standard errors shape ($\xi$) | 95% confidence interval scale ($\sigma$) | 95% confidence interval shape ($\xi$) | Variance-Covariance matrix of ($\zeta$, $\sigma$, $\xi$) | | |
|---|---|---|---|---|---|---|---|---|---|---|---|
| | | | | | | | | | 7.10E-08 | 0 | 0 |
| L1 | 2211 | 0.0126 | 0.476 | -0.121 | 0.0141 | 0.0209 | $[0.448, 0.504]$ | $[-0.162, -0.080]$ | 0 | 0.0001995 | -0.0002299 |
| | | | | | | | | | 0 | -0.0002299 | 0.0004350 |
| | | | | | | | | | 7.60E-08 | 0 | 0 |
| L2 | 2359 | 0.0135 | 0.654 | -0.126 | 0.0175 | 0.0173 | $[0.619, 0.688]$ | $[-0.160, -0.092]$ | 0 | 0.0003062 | -0.0002261 |
| | | | | | | | | | 0 | -0.0002261 | 0.0002992 |
| | | | | | | | | | 9.26E-08 | 0 | 0 |
| L3 | 2899 | 0.0165 | 0.416 | -0.252 | 0.0107 | 0.0183 | $[0.395, 0.437]$ | $[-0.287, -0.216]$ | 0 | 0.0001138 | -0.0001657 |
| | | | | | | | | | 0 | -0.0001657 | 0.0003329 |

# Chapter 3

# Multi-Purpose Floating Offshore System

## 3.1 REFOS Platform

Offshore wind and wave resources demand adequate state-of-the-art technologies in order to be exploited. The renewable energy market has witnessed various offshore wind turbine and WEC concepts till today in a broad range of structures. In deeper waters, the need for floating structures is imperative and thus, the global focus is spotted on such projects. The main target however, apart from the reliability of the structures, is the economic feasibility that characterizes an offshore project, as there are still parameters such as mooring systems and wind turbine's rated power, that contribute to increased costs. Low rated power and high cost of moorings increase the LCOE, a challenge that is currently faced by the scientific community. A concept to decrease the LCOE is through hybrid solutions by co-exploiting offshore wind and wave via the same floating system. In the present work, the Renewable Energy Multi-Purpose Floating Offshore System (REFOS) [43, 44], a European project developed in the National Technical University of Athens, will be utilized and modified to investigate the produced energy in the three selected locations that presented in the previous chapter.

The REFOS platform is a TLP type multi-purpose floater supporting the DTU 10MW reference wind turbine (RWT), that also encompasses three cylinders, which include three OWC devices (Fig. 3.1 and 3.2). Details of the modelling of the system as well as hydro-aero-elastic coupling between the floater, the mooring system, and the WT have been presented, incorporating the solutions of the diffraction, the motion-

and the pressure-dependent radiation problems around the moored structure in the analysis, along with the aerodynamics of the WT and validation experiments through scaled-down model tests [44]. Moreover, the air turbines installed at the top of each device's oscillating chamber have been investigated in terms of optimization on their characteristics (e.g., its pneumatic admittance) for maximum wave energy absorption [43]. The system's characteristics are presented in more detail in Tab. 3.1 to 3.3 and Fig. 3.3, nevertheless, for the purposes of this work, the mooring system will be modified, analyzed and discussed extensively in Sections 3.3 and 3.4. Regarding the supported wind turbine, the respective properties are shown in Tab. 3.4.

Figure 3.1: REFOS structure above (left) and below (right) sea water level. Source: [44]

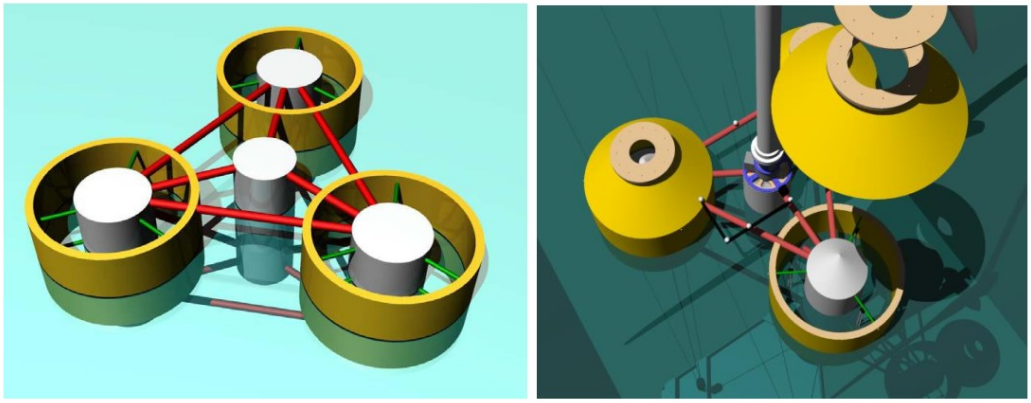

Figure 3.2: 3D representation of the REFOS floater: without the oscillating water column (OWC) domes (left); with the conical OWC domes (right). Source: [44]

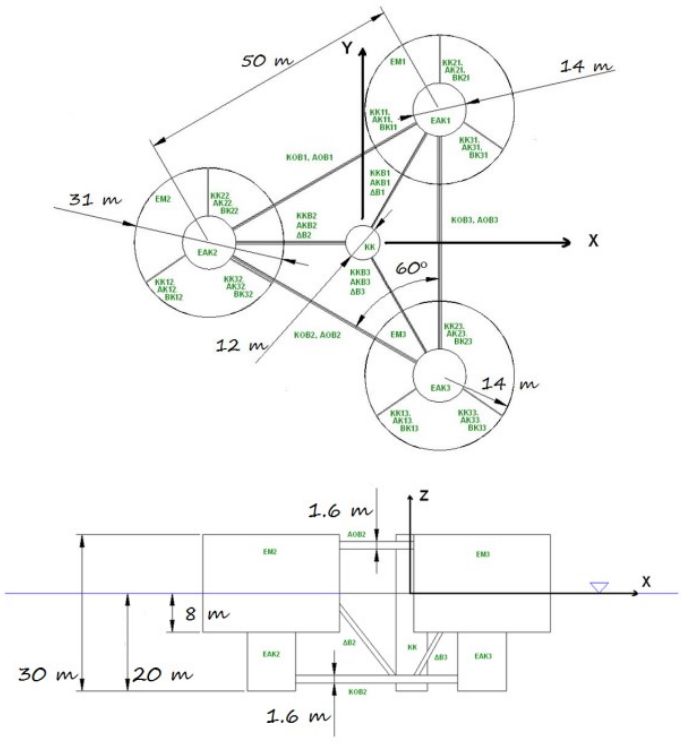


Figure 3.3: Top and side view of the REFOS floater. Source: [66].

Table 3.1: Floating platform geometry. Source: [44].

| **Oscillating Water Column (OWC) Devices** | |
|---|---|
| Diameter of inner concentric cylindrical body | 14.00 m |
| Draught of inner concentric cylindrical body | 20.00 m |
| Oscillating chamber thickness of each chamber | 1.500 m |
| Outer radius of the oscillating chamber of each device | 15.50 m |
| Oscillating chamber's draught | 8.000 m |
| Spacing between columns (distance from the center of the bodies) | 50.00 m |
| Elevation of offset columns above SWL | 10.00 m |
| **Central cylindrical body supporting WT** | |
| Diameter of main column | 12.00 m |
| Draught of main column | 20.00 m |
| Elevation of main column (tower base) above SWL | 10.00 m |
| Depth of platform base below SWL (total draught) | 20.00 m |
| Diameter of pontoons and cross braces | 1.600 m |

Table 3.2: Mass distribution. Source: [44].

| **Mass of the Floater** | |
|---|---|
| Mass of each oscillating chamber (including ballast) | 1140 t |
| Mass of each concentric cylindrical body | 828 t |
| Mass of the central cylindrical body (including ballast) | 1218.5 t |
| Mass of braces | 408.6 t |
| Total mass of the floater | 7531.1 t |
| Mass of the 10 MW WT | 1100 t |
| Mass of each air turbine (including generator) | 3.3 t |
| Mass of each mooring tendon in water (3 tendon pipes) | 192 t |
| Total mass of the REFOS platform | 9550 t |
| Center of mass (CM) location below SWL | 3.180 m |
| Center of buoyancy below SWL | 8.651 m |
| Platform roll inertia about CM | $6.385 \times 10^6 \text{tm}^2$ |
| Platform pitch inertia about CM | $6.385 \times 10^6 \text{tm}^2$ |
| Platform yaw inertia about CM | $1.170 \times 10^7 \text{tm}^2$ |

Table 3.3: Initial mooring system properties. Source: [44].

| | |
|---|---|
| Number of tendons | 3 |
| Depth to anchors below SWL (Water depth) | 180 m |
| Depth to fairleads below SWL | 20 m |
| Mooring line length | 160 m |
| Tendon outer diameter (OD) | 1.2192 m |
| Tendon wall | 0.0422 m |
| Equivalent mooring line mass density | 104 kg/m |
| Equivalent mooring line mass in water | 888.6 N/m |
| Mooring line stiffness $k_{xx}$ of each tendon | 104.0 kN/m |
| Mooring line stiffness $k_{zz}$ of each tendon | 173533 kN/m |
| Pretension of each tendon | 18838 kN |
| Young's modulus of elasticity | 200 GPa |
| Yield stress | 482.5 MPa |

Table 3.4: Properties of the 10 MW DTU RWT. Source: [43].

| | |
|---|---|
| Cut in, out speeds | 4-25 m/s |
| Rated wind speed | 11.4 m/s |
| Nominal power | 10 MW |
| Number of blades | 3 |
| Rotor diameter | 14.00 m |
| Length of each blade | 86.35 m |
| Mass of each blade | 41.716 t |
| Mass of the hub | 105.5 t |
| Mass of the nacelle | 406 t |
| Mass of the tower | 563.3 t |
| Total mass of the WT | 1200 t |

## 3.2 Hydrodynamics and Coupled Analysis

Initializing the process of analyzing such complex systems, it is necessary to examine the hydrodynamic problem step by step through the individual phenomena. In literature, one can find a number of mathematical formulations and solutions emanating from hydromechanical theory. Surface wave interactions with systems of oscillating bodies and pressure distributions have been studied decades ago [67]. Furthermore, the solution of both diffraction and radiation problems has been presented, through a macroelement method, approximating the velocity with Fourier series, for the linear hydromechanics analysis of vertical bodies of revolution [68]. Further work has been conducted for multi-body configurations consisting of an arbitrary number of vertical bodies of revolution, having any geometrical arrangement and individual body geometries, investigating their hydrodynamic interaction in infinite or finite depth [69, 70]. Additional material can be found regarding the solution of the diffraction, the pressure- and motion-dependent-radiation problems for an array of hydro-dynamically interacting OWC's devices consisting of concentric vertical cylinders, either floating independently or as a unit assuming a platform [71, 72]. As far as the REFOS platform is concerned, an analytical method has been developed to solve all the aforementioned problems, considering either free-floating state or TLP configuration, calculate the first- and mean second-order wave forces, the inner air pressure and the free-surface oscillation amplitude inside and outside each OWC device, as well as evaluate the wave power efficiency of the system [73, 74]. Moreover,

the coupled hydro-aero-elastic problem has been scrutinized and numerical results have been presented for the exciting forces acting on the platform, the hydrodynamic damping coefficients, as well as the platform's responses and the total mooring forces [75]. Similar work can be found also encompassing a smaller wind turbine on a similar floater, where numerical results are compared with experimental data [76]. In the subsections below, theory on hydrodynamics and on hydro-aero-elastic simulation will be presented, concerning the analysis of the REFOS platform moored with catenaries.

### 3.2.1 Hydrodynamics

In this section, a short introduction to the theory of hydrodynamics of the floater will be presented, yet a more detailed analysis can be found in [73, 74]. To begin with, we assume a plane periodic wave of amplitude $H/2$, frequency $\omega$, and wave number $k$, propagating in water of finite depth $d$, exciting the REFOS triangular floater, which consists of 4 bodies (3 OWC devices and 1 vertical cylindrical body supporting the WT). In order for the linear potential theory to be employed, small amplitude as well as inviscid, incompressible and irrotational fluid flow is assumed. For reasons of reference, a global Cartesian co-ordinate system O-XYZ with origin on the seabed and its vertical axis OZ directed positive upwards is used, along with three local cylindrical co-ordinate systems $(r_q, \theta_q, z_q)$, $q = 1, 2, 3$ with similar origins and directions. The fluid flow around the device of order $q = 1, 2, 3, 4$ can be described by the potential function:

$$\Phi^q \left(r_q, \theta_q, z; t\right) = Re\left\{\phi^q \left(r_q, \theta_q, z\right) \cdot e^{-i\omega t}\right\} \tag{3.1}$$

On the basis of linear modeling, the spatial function $\phi^q$ can be decomposed as:

$$\phi^q = \phi_0^q + \phi_7^q + \sum_{p=1}^{N} \sum_{j=1}^{6} \dot{\xi}_{j0}^p \cdot \phi_j^{qp} + \sum_{p=1}^{N} p_{in0}^p \cdot \phi_p^{qp} \tag{3.2}$$

Here, $\phi_0^q$ is the velocity potential of the undisturbed incident harmonic wave; $\phi_7^q$ is the scattered potential around the q device, when it is considered fixed in waves with the duct open to the atmosphere, so that the pressure in the chamber is equal to the atmospheric one; $\phi_j^{qp}$ is the motion–dependent radiation potential around the body $q$, resulting from the forced oscillation of the $p$ body in $j$ direction with unit velocity amplitude $\dot{\xi}_{j0}^p$ considering the air chambers of all the devices open to the atmosphere.

Index $j = 1, 2, ..., 6$ represents the surge, sway, heave, roll, pitch and yaw modes of motion respectively. Additionally, $\phi_p^{qp}$ is the pressure–dependent radiation potential around the $q$ body when it is considered open to the atmosphere (i.e., atmospheric air pressure inside its chamber), due to unit time harmonic oscillating pressure head $p_{in0}^{p}$ in the chamber of the $p$ device when all the devices are considered fixed in calm water.

The potentials $\phi_j^q(j = 0, 7; q = 1, 2, 3, 4)$, $\phi_j^{qp}(j = 1, ..., 6; q, p = 1, 2, 3, 4)$ and $\phi_p^{qp}(q = 1, 2, 3, 4; p = 1, 2, 3)$ are solutions of Laplace's equation in the entire fluid domain and satisfy the zero normal velocity on the sea bed ($z = 0$). They also satisfy the boundary conditions at the outer and inner free sea surface ($z = d$) of each body, as well as fulfil kinematic conditions on the mean body's wetted surface, all of which are presented in [73]. Finally, a radiation condition is imposed which states that disturbance propagation must be outgoing.

In order to evaluate the $\phi_j^q$, $\phi_j^{qp}$ and $\phi_p^{qp}$ potentials, the method of matched axisymmetric eigenfunction expansions is applied. Hence, the flow field around each body of the hybrid platform can be subdivided in coaxial ring-shaped fluid regions in which different velocity potential expansions are made. The latter are then matched by continuity requirements of the velocity potentials and their radial derivatives along the vertical boundaries shared by adjacent fluid regions [44]. The diffraction $\phi_D^q = \phi_0^q + \phi_7^q$, the motion-radiation $\phi_j^{qp}$ and the pressure-radiation $\phi_p^{qp}$ potentials in each fluid domain of the $q$ body, $q = 1, 2, 3, 4$, expressed in its co-ordinate system can be written as:

$$\phi_D^q\left(r_q, \theta_q, z\right) = -i\omega \frac{H}{2} \sum_{m=-\infty}^{\infty} i^m \Psi_{m,D}^q\left(r_q, z\right) e^{im\theta_q} \tag{3.3}$$

$$\phi_j^{qp}\left(r_q, \theta_q, z\right) = -i\omega \sum_{m=-\infty}^{\infty} \Psi_{m,j}^{qp}\left(r_q, z\right) e^{im\theta_q} \tag{3.4}$$

$$\phi_P^{qp}\left(r_q, \theta_q, z\right) = \frac{1}{i\omega\rho} \sum_{m=-\infty}^{\infty} \Psi_{m,P}^{qp}\left(r_q, z\right) e^{im\theta_q} \tag{3.5}$$

Here, the functions $\Psi_{m,D}^q$, $\Psi_{m,j}^{qp}$, $j = 1, 2, \ldots, 6, P$ are the principal unknowns of the problem and the velocity potentials, as expressed above, are evaluated implementing the multiple scattering approach, which accounts for the hydrodynamic interaction phenomena among the bodies of the hybrid structure. Having determined the velocity potentials in each fluid region, the hydrodynamic forces on the hull of the REFOS floater (exciting forces at the $i-th$ direction, $f_i^T, i = 1, \ldots, 6$; hydrodynamic added mass and damping coefficients, $A_{i,j}, B_{i,j}$; pressure hydrodynamic forces at the $i-th$

direction, $f_{P,i}^{T}, i = 1, ..., 6$) can be calculated [73].

As far as wave energy calculations are concerned, it is necessary to briefly present the mathematics behind the function of the OWC devices [73]. The water oscillation inside each device's chamber pushes the dry air above the free surface through a Wells turbine. The volume flow produced by the oscillating internal water surface in the $q$ device ($q = 1, 2, ..., N$) is denoted by $Q^q(t) = Re\left\{q^q \cdot e^{-i\omega t}\right\}$ where:

$$q^q = \iint_{S_i^q} u_z^q dS_i^q = \iint_{S_i^q} u_z^q \left(r_q, \theta_q, z\right) r_q dr_q d\theta_q = \iint_{S_i^q} \frac{\partial \phi^q}{\partial z} r_q dr_q d\theta_q \tag{3.6}$$

Here, $u_z^q$ denotes the vertical velocity of the water free surface in the $q$ device and $S_i^q$ the cross-sectional area of the inner water surface inside the $q$ device. However, similar to the decomposition of $\phi^q$ in, the volume flow $q^q$ in the $q$ device can be written as a function of three terms associated with the diffraction $q_D^q$, the motion-dependent, $q_R^q$ and the pressure-dependent, $q_P^q$, radiation problem, as follows:

$$q^q = q_D^q + q_R^q + \sum_{p=1}^{N} p_{in0}^p \cdot q_p^{qp} \tag{3.7}$$

where $p_{in0}^p$ is the chamber pressure of the $p$ device.

A Wells turbine is assumed to be placed in each devices' duct between the chamber and the outer atmosphere since it rotates in one direction in spite the direction of the air flow. For simplicity, the total volume flow $q^q$, in the $q$ device is proportional to the chamber air pressure by a pneumatic complex admittance $\Lambda^q$ (Eq. (3.8)), which is considered to be a real number, as in this work the air compressibility is neglected.

$$q^q = \Lambda^q \cdot p_{in0}^q \tag{3.8}$$

Finally, the absorbed power, $P^q$, of each OWC device of the array, via Eq. (3.8), can be written as:

$$P^q = \frac{1}{2} Re\left\{q^q \cdot \overline{p_{in0}^q}\right\} = \frac{1}{2} \cdot \Lambda^q \cdot \left|p_{in0}^q\right|^2 \tag{3.9}$$

### 3.2.2 Coupled Hydro-Aero-Elastic Formulation

In order to investigate the dynamic equilibrium of the forces acting on the REFOS structure as well as determine its total responses, the following system of differential equations of motion, describing the couple hydro-aero-elastic problem in the frequency domain is formulated, taking also into account the catenary mooring system that is

applied instead of the TLP design.

$$\sum_{j=1}^{6}\Bigg[-\omega^2\left(M_{i,j}+M_{i,j}^{WT}+A_{i,j}+\frac{i}{\omega}B_{i,j}+\frac{i}{\omega}B_{i,j}^{WT}+\frac{i}{\omega}B_{i,j}^{m}\right) + C_{i,j}^{H}+C_{i,j}^{m}+C_{i,j}^{WT}\Bigg]x_{j0}-f_{P,i}^{T}=f_{i}^{T},\quad i=1,\ldots,6 \quad (3.10)$$

Here, $A_{i,j}$, $B_{i,j}$ are the hydrodynamic mass and potential damping coefficients of the platform; $f_i^T$ and $f_{P,i}^T$, are the exciting- and the pressure hydrodynamic- forces acting on the platform; $x_{j0}$ is the motion component of the REFOS system in the $j-th$ direction with respect to a global co-ordinate system; $M_{i,j}$ is the platform's mass matrix; $C_{i,j}^H$ is the platform's hydrostatic restoring stiffness matrix; whereas regarding the contribution of the wind turbine we have its mass matrix $M_{i,j}^{WT}$ that includes the WT inertia and the gyroscopic effects due to rotation, its damping matrix $B_{i,j}^{WT}$ that includes the WT damping due to rotation and aerodynamics and finally, its stiffness matrix $C_{i,j}^{WT}$ including the contribution from both aerodynamics and gravity [44]. The remaining $B_{i,j}^m$ and $C_{i,j}^m$ are the mooring system's damping matrix and restoring stiffness matrix respectively, with respect to the global co-ordinate system as well. It is noted that depending on the model that the moorings are analyzed, $B_{i,j}^m$ and $C_{i,j}^m$ correspond to dynamic phenomena, while for the quasi-static approach, the damping matrix is equal to zero and $C_{i,j}^m$ differs and includes only the static behavior. Quasi-static and dynamic models will be further discussed in the next sections of this chapter.

## 3.3 Mooring System Analysis

As already mentioned in the beginning of the chapter, the mooring system will be modified, meaning that the TLP concept consisting of vertical tensioned tethers will be replaced with catenaries, in order to evaluate the system's responses based on a more economic approach. In general, different mooring conditions have been investigated regarding the dynamic responses of floating wind turbines, examining variables such as tether length, pretension and tether failure and providing insightful conclusions about the integrity and performance of the structure [77].

In this work, the catenary mooring system of REFOS will be designed and analyzed through the quasi-static approach, whereas a further analysis will be performed regarding the dynamic phenomena of the lines incorporating also the damping ef-

fects. A classical approach to estimate mooring line damping is the calculation of energy dissipation in the mooring system [78]. Frequency- and time-domain analysis methods have been used for the quantitative evaluation of the dissipated energy (absorbed energy per cycle of motion) and the associated mooring line damping, due to line's motions into the water, which is significant in the low frequency range [79]. In addition, it has been shown theoretically and experimentally that model testing of the dynamics of cables submerged in heavy fluids, such as water, requires proper scaling of two fundamental parameters; the elastic stiffness, which is the predominant parameter in determining the dynamic tension, and the free-falling velocity of the line, if the dynamic tension exceeds the static tension [80]. Regarding FOWT, the mooring line damping estimation derived from the calculation of the dissipated energy has been studied on the ITI Energy barge supporting the NREL 5-MW offshore wind turbine, as well as validated through model scale tests [81]. Moreover, similar work has been done on the DeepCwind Semisubmersible FOWT comparing coupled and uncoupled models with tank tests on mooring line dynamics. The analysis revealed that an uncoupled model using the quasi-static mooring approximation can underestimate peak mooring line loads versus a coupled model using a dynamic mooring line [82]. Finally, unlike a typical offshore system, the design of moorings for a WEC device must consider reliability and survivability, and the need to ensure efficient energy conversion. The use of a catenary mooring arrangement for a WEC device could result in a wide range of mooring properties from a fully slack to a semi-taut condition. It has been shown that for semi-taut or high frequency oscillation modes, the damping properties and the accumulated cyclic loading to the mooring system increase, resulting in fatigue damage which could become a major source of failure [83].

### 3.3.1 Quasi-Static Analysis

In theory, the quasi-static approach assumes that the motion of the system is uniform and linear between two static positions, during a given time step for which the loads on the systems are assumed constant (Fig. 3.4). The dynamic effects on the mooring system are ignored by this method, omitting the motion dependency of mass, damping and fluid acceleration on the system. Quasi-static models derive the mooring line shape and tension from the catenary formulations, based on the assumption that the line is in static equilibrium in each time step, that inertia effects can be neglected and that the line profile is well described by the catenary equations. In this category,

slack moorings mainly produce static restoring forces, resulting from the weight of the line. The restoring force can be also calculated from the catenary equations, by taking the derivative of the tension with respect to the displacement. Buoys or clump weights can be used to locally modify the weight or buoyancy of the mooring line and consequently the stiffness characteristics of the mooring system [84]. The main disadvantage of quasi-static models, however, is that they neglect hydrodynamic and inertial forces on the line, which can affect the structure's response and are especially important for predicting the mooring loads. This effect on structure's response also overestimates the motions, which eventually lead to decreased power absorption from the OWC devices.

Applying a quasi-static model for the design of a mooring system, the following procedure needs to be followed. The mooring system is initially considered to undergo only pretention loads without any external excitation forces and then it is displaced from its initial equilibrium position under the action of environmental generated forces. Hence, the mooring characteristics of the system (i.e., tension forces, suspended mooring line length, horizontal distance between the anchor and the fairlead, and vertical projection of the suspended mooring line length) in its new displaced position are calculated. In addition, the mooring restoring coefficients, $c_{lj}^{m,i}$, of each line $i$ and, consequently, the restoring mooring stiffness coefficients $\overline{C}_{lj}^{m}$, $l, j = 1, \ldots, 6$, in the global mooring coordinate system are defined [85]. The aforementioned description is paired with the application of the following equations [86]. Firstly, the value of line pretension needs to be estimated, assuming the line characteristics and a given depth. This results from an iterative process through Eq. (3.11) and (3.12) and a given offset criterion $\delta x/D$ due to an external force $H_{ex}$, applying also that $H_1 = H_{ex} + H_2$, where $H_2 = aH_{ex}$ a significantly smaller fraction of $H_{ex}$, assuming that $H_1$, $H_2$ are the horizontal line tensions in a simplified configuration of a pair of mooring lines (i.e., like Fig. 3.4 with an extra line at the right side of the floater).

$$2 \cdot \delta x = D \left\{ \sqrt{1 + 2\frac{H_2}{D \cdot w}} - \sqrt{1 + 2\frac{H_1}{D \cdot w}} \right\} + \frac{H_1}{w} \cosh^{-1}\left(1 + \frac{D \cdot w}{H_1}\right) - \frac{H_2}{w} \cosh^{-1}\left(1 + \frac{D \cdot w}{H_2}\right) \quad (3.11)$$

$$\delta x = D\left\{\sqrt{1+2\frac{H_p}{D\cdot w}}-\sqrt{1+2\frac{H_1}{D\cdot w}}\right\} + \frac{H_1}{w}\cosh^{-1}\left(1+\frac{D\cdot w}{H_1}\right)-\frac{H_p}{w}\cosh^{-1}\left(1+\frac{D\cdot w}{H_p}\right) \quad (3.12)$$

Another criterion that has to be satisfied refers to the breaking tension, where the upper limit is 55% of the Minimum Breaking Load (MBL) of the line (Eq. (3.13)), which determines also the suspended mooring line length $L_s$ and subsequently the total mooring length $L$ (Eq. (3.14)), taking into account the line's elasticity. Having defined the aforementioned parameters, the horizontal projection $x_s$ of $L_s$, as well as the horizontal distance between the anchor and the fairlead $x$ can be calculated for any load condition via Eq. (3.15) and (3.16) (i.e., for pretension $H = H_p$ while for loading $H = H_1$). It is noted that $\varphi$ and $\varphi_A$ are the line angles at the fairlead and the anchor, respectively, and it is always considered that $\varphi_A = 0$ in order to fulfil the fundamental condition of catenaries and avoid a taut-leg configuration (Fig. 3.4).

$$\sigma_{br} = \frac{T}{a_0 A} = \sqrt{\frac{H^2+(wL_S)^2}{a_0 A}},\ a_0^{\max} = 55\% \quad (3.13)$$

$$L_s = \frac{H}{w}\left\{\sqrt{\left(\frac{wD}{H}+\sqrt{1+\tan^2\varphi_A}\right)^2-1}-\tan\varphi_A\right\},\quad L = L_s/0.9 \quad (3.14)$$

$$x_s = \frac{H}{w}\left\{\sinh^{-1}(\tan\varphi)-\sinh^{-1}(\tan\varphi_A)\right\}+\frac{HL_s}{EA} \quad (3.15)$$

$$x = x_s + (L - L_s) \quad (3.16)$$

As far as the restoring coefficients are concerned, $c_{lj}^{m,i}$ can be evaluated using well-known quasi-static equations of a single mooring line, i.e.,

$$c_{11}^{m,i} = \frac{\delta H}{\delta x},\quad c_{22}^{m,i} = \frac{H}{x_s},\quad c_{33}^{m,i} = \frac{\delta V}{\delta z},\quad c_{13}^{m,i} = c_{31}^{m,i} = \frac{\delta V}{\delta x} \quad (3.17)$$

forming the symmetric 3×3 matrix of line $i$ at its local coordinate system as

$$\left[c_{lj}^{m,i}\right] = \begin{bmatrix} c_{11}^{m,i} & 0 & c_{13}^{m,i} \\ 0 & c_{22}^{m,i} & 0 \\ c_{31}^{m,i} & 0 & c_{33}^{m,i} \end{bmatrix} \quad (3.18)$$

From Eq. (3.17) and following an analytical solution, it results that

$$
\begin{aligned}
c_{11}^{m,i} &= \frac{\sinh\varepsilon}{\varepsilon\sinh\varepsilon + 2(1-\cosh\varepsilon)}w, \quad c_{33}^{m,i} = \frac{\varepsilon\cosh\varepsilon - \sinh\varepsilon}{\varepsilon\sinh\varepsilon + 2(1-\cosh\varepsilon)}w, \\
c_{13}^{m,i} &= c_{31}^{m,i} = \frac{\cosh\varepsilon - 1}{\varepsilon\sinh\varepsilon + 2(1-\cosh\varepsilon)}w, \quad \varepsilon = \frac{wx_s + V - wL_s}{H}
\end{aligned}
\tag{3.19}
$$

where in our case $\varepsilon = wx_s/H$ ($V = wL_s$), since there are no additional parts on the line (i.e., buoys or weights).

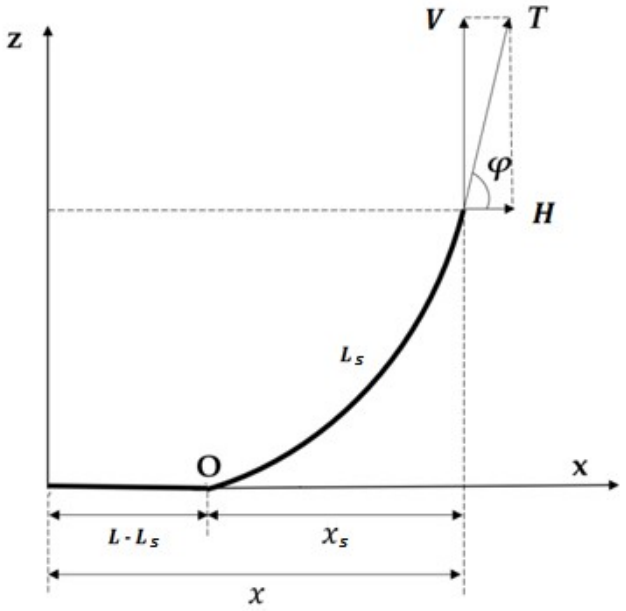


Figure 3.4: Schematic representation of a 2D typical mooring line. Source: Adapted from [85]

With respect to the global coordinate system, the total mooring stiffness symmetric 6×6 matrix $\left[\bar{C}_{lj}^{m}\right]$ of N lines can be expressed as

$$
\left[\bar{C}_{lj}^{m}\right] = \sum_{i=1}^{N} \left[\lambda^{i}\right]^{T} \left[c_{lj}^{m,i}\right] \left[\lambda^{i}\right] \tag{3.20}
$$

with $[\lambda^i]$ being the rotation matrix defined as

$$
\left[\lambda^{i}\right] = \begin{bmatrix} \cos a^{i} & \sin a^{i} & 0 \\ -\sin a^{i} & \cos a^{i} & 0 \\ 0 & 0 & 1 \end{bmatrix} \tag{3.21}
$$

The remaining terms of the symmetric matrix $\left[\bar{C}^m_{lj}\right]$ can be calculated by Eq. (3.22), assuming that $(x_1, y_1, z_1)$ are the coordinates of the mooring line attaching points on the structure with respect to the global coordinate system located at the body's vertical axis and at the undisturbed free surface.

$$
\begin{gathered}
\bar{C}^m_{41} = \bar{C}^m_{31} y_1 - \bar{C}^m_{21} z_1,\ \bar{C}^m_{51} = \bar{C}^m_{11} z_1 - \bar{C}^m_{31} x_1,\ \bar{C}^m_{61} = \bar{C}^m_{21} x_1 - \bar{C}^m_{11} y_1 \\
\bar{C}^m_{42} = \bar{C}^m_{32} y_1 - \bar{C}^m_{22} z_1,\ \bar{C}^m_{52} = \bar{C}^m_{21} z_1 - \bar{C}^m_{32} x_1,\ \bar{C}^m_{62} = \bar{C}^m_{22} x_1 - \bar{C}^m_{21} y_1 \\
\bar{C}^m_{43} = \bar{C}^m_{33} y_1 - \bar{C}^m_{32} z_1,\ \bar{C}^m_{53} = \bar{C}^m_{31} z_1 - \bar{C}^m_{33} x_1,\ \bar{C}^m_{63} = \bar{C}^m_{32} x_1 - \bar{C}^m_{31} y_1 \\
\bar{C}^m_{44} = \bar{C}^m_{33} y_1^2 - 2\bar{C}^m_{32} y_1 z_1 + \bar{C}^m_{22} z_1^2 \\
\bar{C}^m_{54} = \bar{C}^m_{31} y_1 z_1 - \bar{C}^m_{21} z_1^2 - \bar{C}^m_{33} y_1 x_1 + \bar{C}^m_{32} x_1 z_1 \\
\bar{C}^m_{64} = \bar{C}^m_{32} x_1 y_1 - \bar{C}^m_{31} y_1^2 - \bar{C}^m_{22} x_1 z_1 + \bar{C}^m_{21} y_1 z_1 \\
\bar{C}^m_{55} = \bar{C}^m_{11} z_1^2 - 2\bar{C}^m_{31} x_1 z_1 + \bar{C}^m_{33} x_1^2 \\
\bar{C}^m_{65} = \bar{C}^m_{21} x_1 y_1 - \bar{C}^m_{32} x_1^2 - \bar{C}^m_{11} y_1 z_1 + \bar{C}^m_{31} x_1 y_1 \\
\bar{C}^m_{66} = \bar{C}^m_{22} x_1^2 - 2\bar{C}^m_{21} x_1 y_1 + \bar{C}^m_{11} y_1^2
\end{gathered}
\tag{3.22}
$$

### 3.3.2 Dynamic Analysis

In order to approach a more realistic condition of the mooring system responses in the frequency domain, it is necessary to investigate its dynamics through the dynamic stiffness and damping effects. In general, there are a number of contributions to the overall damping from the mooring system. These are: (i) hydrodynamic drag damping due to the line's relative motion with the fluid, (ii) vortex induced vibration (VIV) due to vortex formation especially in wire lines, (iii) line internal damping due to friction between the chain links and (iv) damping caused by seabed interaction, where soil friction increases the line's stiffness as it reduces the tension fluctuations on the grounded part of the line [87]. Regarding these effects, it has been found that neglecting the drag amplification due to vortex-induced vibrations and wave-induced motions causes underprediction of the order of 50% in the value of the mooring line damping coefficient [88]. Apart from the classical approach to estimate mooring line damping through the calculation of energy dissipation, another one has been presented using a simplified dynamic model, assuming a system that consists of a viscous damper and a linear elastic spring in parallel, representing the geometric stiffness, which is further coupled in series to a linear elastic spring representing the elastic stiffness of the mooring line [89]. Although such assessment is conservative and bearing in mind that the more phenomena are taken into account the more precise

the procedure gets, the simplicity of the dynamic analysis constitutes a trade-off of computational efficiency and strict approximation. In this respect, the procedure of estimating the dynamic characteristics of the mooring system is described below.

In general, wave frequency (WF) motion generates periodic movement and causes the fairlead to oscillate. These oscillations are transferred to the top of the mooring line and propagate along the line with a fair amount of lag due to inertia (Fig. 3.5), whereas significant damping effects occur due to drag forces and the heavy medium of propagation. Slack mooring lines may also present dynamic restoring forces in the case of high frequency (HF) motion, whereby small displacements at the top end of the mooring line, can result in large lateral displacements at the midpoint of the mooring line. As the frequency increases, nonlinear drag (which increases with the square of frequency) provides very large lateral resistance, causing the mooring line to "freeze" in place and the motion to be then accommodated elastically by the mooring line [84]. In the HF range, special treatment is needed for the VIVs acting on the lines, while low frequency motion (LF), i.e., tidal influences or horizontal second order wave drift motions, as well as static loading may be approximated via the quasi-static models. However, in reality, the mooring dynamics at different frequencies are, in fact, coupled and this coupling should be taken into account for accurate modelling of the mooring system.

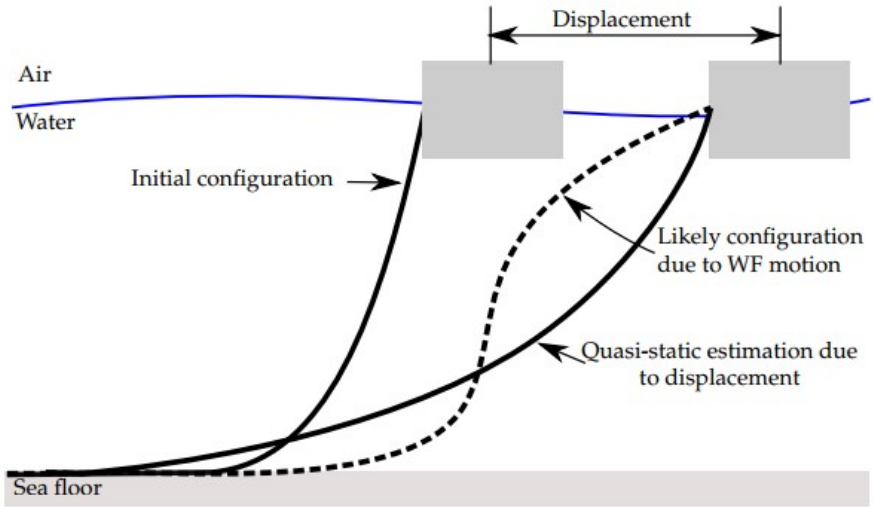


Figure 3.5: Difference between the dynamic (dashed line) and quasi-static model (solid line) regarding a timestep of the line's profile. Source: [84]

The contribution of the mooring lines to the total damping of a moored structure is a very important element for the evaluation of the body's responses. Due to the line

motions in the fluid domain, the phenomenon of energy dissipation appears, which offers to the moored body an additional amount of damping (i.e., mooring damping) originating from the drag and viscous forces on the mooring lines [85]. The motions of the floater can be expressed in terms of the response amplitude operator (RAO), where in our case due to symmetry we examine the RAOs of surge ($\mathrm{RAO}_1$), heave ($\mathrm{RAO}_3$) and pitch ($\mathrm{RAO}_5$), which are defined as:

$$\mathrm{RAO}_l = \frac{x_{j0}}{H/2}, \quad l = 1, 3; \quad \mathrm{RAO}_5 = \frac{x_{j0}}{kH/2} \tag{3.23}$$

where $k$ denotes the wave number. The dynamic modeling enables the evaluation of the dynamic tension, $F_{lj}^{d,i}$, at the top of each line $i$ and subsequently the mooring line damping, $B_{m,lj}^{i}$, and the mooring restoring coefficients $C_{m,lj}^{i}$, as it holds that:

$$\frac{F_{lj}^{d,i}}{A_j} = C_{m,lj}^{i} + iB_{m,lj}^{i} \tag{3.24}$$

where $C_{m,lj}^{i}$ and $B_{m,lj}^{i}$, both frequency- and excitation-amplitude-dependent, stand for the real and imaginary parts of $F_{lj}^{d,i}/A_j$ expressed in the local mooring coordinate system. The total frequency-dependent mooring system restoring stiffnesses, along with the corresponding total mooring line damping components can be derived with respect to the global coordinate system, through the transformation expressed in Eq. (3.20) to (3.22). However, to perform such calculations demands an iterative procedure. Initially, the $\mathrm{RAO}_l$ of the body is evaluated via Eq. (3.10), either as if it were floating without mooring constraints, (i.e., for zero $C_{lj}^{m}$ and $B_{lj}^{m}$ terms), or starting from a quasi-static approach (i.e., for $C_{lj}^{m}$ from quasi-static analysis and zero $B_{lj}^{m}$), and fed into the mooring dynamic model. Thus, the dynamic tensions are calculated for the specific values of the body's motions. Subsequently, the corresponding values of $C_{lj}^{m}$ and $B_{lj}^{m}$ are applied to the hydrodynamic formulation (Eq. (3.10)), and new values of $\mathrm{RAO}_l$ (i.e., denoted by $\mathrm{RAO}_l^2$) are determined. The iterative procedure continues until

$$\mathrm{RAO}_l^N - \mathrm{RAO}_l^{N-1} < \varepsilon \tag{3.25}$$

where $N$ stands for the iteration-cycle number, while the value of $\varepsilon$ depends on the accuracy of the applied solution [85]. After the aforementioned convergence process, the dynamic characteristics of the mooring system are well determined and a more realistic analysis on the floater's response and performance is conducted.

## 3.4 Results

### 3.4.1 Mooring System

Initializing the mooring system design, it is necessary to decide the mooring system configuration, regarding the number of the lines as well as their direction. In this work, the catenary mooring system of the REFOS platform is assumed to consist of 3 lines, one attached to each inner concentric cylinder of each OWC device. The configuration is depicted in Fig. 3.6, while the fairlead coordinates with respect to the global coordinate system (i.e., originating from the sea surface and the center of the central cylindrical body supporting the WT) are shown in Tab. 3.5.

Table 3.5: Fairlead coordinates and line directions.

| | Line 1 | Line 2 | Line 3 |
|---|---|---|---|
| $x(m)$ | $-28.87$ | 14.43 | 14.43 |
| $y(m)$ | 0 | 25 | $-25$ |
| $z(m)$ | $-20$ | $-20$ | $-20$ |
| $\alpha(deg)$ | 0 | 240 | 120 |

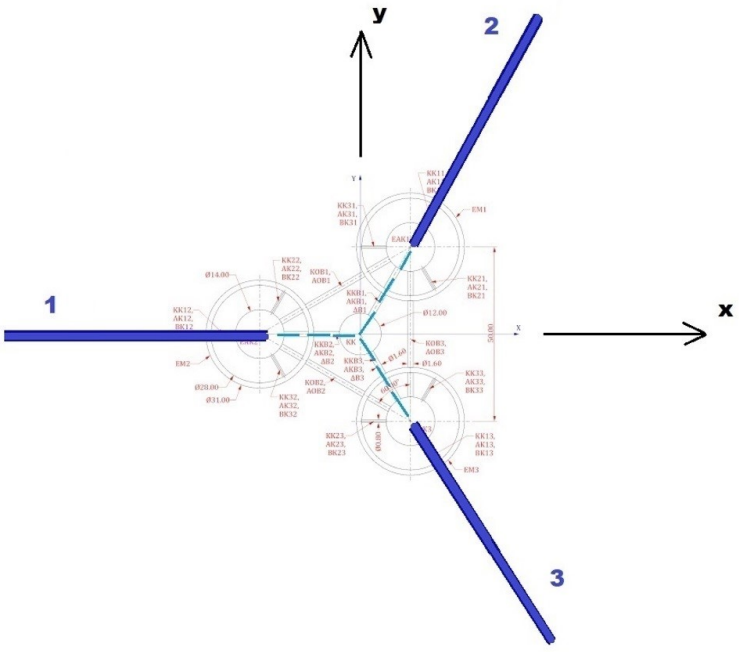


Figure 3.6: Top view of the catenary mooring system configuration. Source: Adapted from [90].

For reasons of completeness, two designs were investigated in terms of materials; a studless chain of Class R3 from Anchor Marine and a wire rope from Teufelberger-Redaelli. For both cases, the procedure described in Subsection 3.3.1 was applied, using Eq. (3.11) to (3.14) to estimate the horizontal pretension ($H_p$), through an iterative process in order for all conditions to be satisfied. It is noted that the installation depth was considered the same with the TLP concept (about 200 m) for comparison purposes, but the depth applied in the calculations is the vertical distance between the fairlead and the seabed i.e., $D = 200\ m - 20\ m = 180\ m$. Moreover, for the maximum offset criterion, it holds that $\delta x/D = 6\%$ and the external loading is assumed to be $H_{ex} = 3140$ kN, which corresponds to the maximum thrust of the wind turbine (1660 kN) plus the drift force (1480 kN) of the mean second-order surge due to waves [90]. The line characteristics and the resulted horizontal pretension are shown in Tab. 3.6.

Table 3.6: Studless chain and wire rope line specifications.

| Variable | Chain | Rope |
|---|---|---|
| Diameter (m) | 0.127 | 0.140 |
| Mass (kg/m) | 323 | 95.81 |
| Weight in water (N/m) | 2913.89 | 816.39 |
| EA (MN) | 1420 | 2614 |
| MBL (kN) | 12171 | 17928 |
| Horizontal Pretension (kN) | 2800 | 1370 |

Subsequently, the mooring system should be analyzed as a whole configuration, to further examine its properties. For that purpose, software from the Laboratory for Floating Structures and Mooring Systems (LFSMS) of the School of Naval Architecture and Marine Engineering in NTUA was utilized, in order to determine stiffness coefficients and include damping effects. The four programs that were used in this stage are in FORTRAN programming language and they were executed in series depending on the examined case. Firstly, NMPREP was used to generate the input file for the next program, which is NMSTAC, including all the line characteristics of the studless chain. It is noted that in this case, the chain diameter was set to be the equivalent one, i.e., $d_{eq} = d\sqrt{2} = 0.1796$ m, due to link geometry, whereas, in general, the total line length was estimated via Eq. (3.14). Next, NMSTAC was executed to derive results for the total mooring system, performing quasi-static analysis and taking into account second-order phenomena such as drift. As far as the applied loading

is concerned, it is considered equal to pretension without additional forces, due to the fact that the requested sought-for properties are needed in pretension conditions. From the output file of NMSTAC, the necessary results were derived to run NSTAC, which analyzes only one line in quasi-static conditions considering drift as well. At this stage, the line is set exclusively with its suspended length and generates the input file for the last program NTRANS, which performs line analysis in a frequency domain set by the user. In our cases, the frequency range was set to be [0.0001, 3] as the zero frequency would display errors during the runs. However, it is assumed that 0.0001 is approximately equal to zero excitation frequency, which allows prediction of the mooring stiffness imposed on the floating structure. At this stage, the values of $C_{11}$, $C_{13}$, $C_{31}$, and $C_{33}$ of the examined line in its local coordinate system are estimated and the final calculations to derive the total stiffness matrix of the mooring system with respect to the global coordinate system can be done according to the process described in Subsection 3.3.1 and based on the Eq. (3.20) and (3.22). It is noted that the value of $C_{22}$ can be estimated via Eq. (3.17) accordingly, while for the case of the wire rope, the same procedure is followed (the input file of NMSTAC in this case can be easily created by the user).

As mentioned before, the above completed procedure of estimating the stiffness matrix of the mooring system was performed regarding only pretension as the main loading. However, some line characteristics were also derived assuming the horizontal external force $H_{ex} = 3140$ kN as the main force on the structure. NMPREP was executed again for each case i.e., studless chain and wire rope, and results about suspended length ($L_s$) and its horizontal projection on the seabed ($x_s$), portion of the line laying on the seabed ($L - L_s$), top-end line angle ($\varphi_{top}$), anchor-fairlead distance ($x$) and ratio of maximum and breaking tension ($T_{max}/MBL$), are shown in Tab. 3.7. Last but not least, the stiffness matrices regarding the line in its local coordinate system as well as the total mooring configuration with respect to the global coordinate system were estimated and the respective ones for the case of the studless chains are presented in Tab. 3.8 and 3.9.

Table 3.7: Studless chain and wire rope line characteristics in pretension and loading conditions after quasi-static analysis.

| Variable | Chain | | Rope | |
|---|---|---|---|---|
| | Pretension | Loading | Pretension | Loading |
| $L_s$ (m) | 614.40 | 822.50 | 802.50 | 1346.40 |
| $x_s$ (m) | 551.70 | 770.60 | 747.25 | 1303.80 |
| $L$ (m) | 900 | 900 | 1500 | 1500 |
| $L - L_s$ (m) | 285.60 | 77.50 | 697.50 | 153.60 |
| $x$ (m) | 837.30 | 848.10 | 1444.75 | 1457.40 |
| $\varphi_{top}$ (deg) | 32.56 | 24.60 | 25.28 | 15.21 |
| $T_{max}/MBL$ (%) | 27.40 | 47.30 | 8.60 | 23.40 |

Table 3.8: Single line stiffness matrix (in $[kN/m]$) referring to studless chain with respect to the local coordinate system (software results).

| Cij | 1 | 2 | 3 |
|---|---|---|---|
| 1 | 153.867 | 0 | 44.864 |
| 2 | 0 | 4.833 | 0 |
| 3 | 44.879 | 0 | 18.483 |

Table 3.9: Total stiffness matrix (in $[kN/m; kNm]$) of the entire mooring system consisting of studless chains with respect to the global coordinate system.

| | | | | | |
|---|---|---|---|---|---|
| 230.801 | 0 | 0 | 0 | −4616.010 | 0 |
| 0 | 7.250 | 0 | 144.992 | 0 | −104.660 |
| 0 | 0 | 55.449 | 0 | 0.185 | 0 |
| 0 | 144.992 | 0 | 26003.586 | 0 | −2093.199 |
| −4616.010 | 0 | 0.185 | 0 | 115422.595 | 0 |
| 0 | −104.660 | 0 | −2093.199 | 0 | 52614.864 |

### 3.4.2 Coupled analysis software

After determining the mooring system characteristics, a coupled analysis is performed to estimate the platform's responses, the pressure inside the OWC chambers as well as the mooring line tensions, taking into account hydrodynamic effects from waves, aerodynamic effects from the wind turbine and effects due to moorings, as

mentioned in Subsection 3.2.2. The solution of Eq. (3.10) is derived by executing the HAMVAB software from LFSMS in NTUA, which performs the hydrodynamic analysis of the bodies in the REFOS structure in the frequency domain [91]. However, due to the modification of the mooring system, it is necessary to estimate the new total mass and center of mass (CoM) of the platform, as well as its hydrostatic restoring matrix, regarding the two designs, i.e., catenaries with studless chain or wire rope.

The difference between the TLP design and the free-floating case is the influence of the applied pretension and the mass regarding the suspended line length. Due to the presence of moorings, in order to maintain a constant draft at 20 m, the platform requires a different ballast and as a consequence, the CoM alters as well. Firstly, the new total mass and CoM were calculated for the case of chain moorings. Taking the free-floating data as reference, i.e., $\Delta_0 = 15205$ tn and $KG_0 = -14.95$ m, the new mass for the first examined case is derived by subtracting the total line mass (547.13 tn) and the equivalent mass from pretension (547.46 tn), from the free-floating mass. As a result, the new total mass of the platform with studless chain moorings equals to 14657.5 tn. The next step is to estimate the CoM, which requires the knowledge of the quantity of ballast that was extracted from the platform's tanks. In a fair approximation, knowing the area of the ballast tanks (574.91 $m^2$) and the subtracted water mass $P = 547.13 + 547.46 = 1094.59$ tn, the lowering of the water surface in the tanks can be estimated and in our case equals to 1.86 m. Moreover, the total displacement ($\Delta = 14657.50$ tn) is equal to the total mass, hence the new ballast equals to 5469.40 tn, taking into account masses of floater, WT and OWCs, whereas the water height in the ballast tanks equals to 9.28 m. Subsequently, from basic theory of ship stability, the new CoM can be estimated as follows:

$$KG = \left(\Delta_0 \cdot KG_0 - P \cdot z_p\right) / \Delta \tag{3.26}$$

where $z_p$ is the CoM of the volume of the subtracted water from the ballast tanks that equals to -9.79 m. Finally, the sought-for CoM equals to -14.78 m. The exact same procedure was followed to estimate the respective variables in the case of wire rope moorings, where the following data were derived: $\Delta = 15006$ tn, $KG = -14.82$ m, $P = 336.42 + 199.24 = 535.66$ tn, $z_P = -9.32$ m, ballast lowering = 0.91 m, ballast = 6028.34 tn, ballast water height = 10.23 m. Lastly, the values of $C_{44} = \Delta \cdot g \cdot GM_T$ and $C_{55} = \Delta \cdot g \cdot GM_L$ of the hydrostatic restoring matrices were calculated. In our case $GM_T$ and $GM_L$ are equal and represent the distances between the center of gravity and the transverse and longitudinal metacenter respectively. Consequently, it

is derived that $C_{44} = C_{55} = 4792523$ kNm for chains and $C_{44} = C_{55} = 4912360$ kNm for wire ropes.

Setting the new data in the input files of the program along with all the respective specification of the mooring lines, the analysis was performed in the frequency domain at a range of $\omega = [0.05, 3]$ rad/s with a step of 0.05 rad/s as well as for three different wave directions, i.e., 0 deg, 30 deg and 60 deg with respect to the global coordinate system. As an example, one of the input files of HAMVAB can be found in Appendix D. For comparison purposes, a free-floating case was also investigated, whereas TLP case data were already available. In Fig. 3.7 to 3.9, all cases are compared referring to the three wave directions respectively. Each figure displays the RAOs of surge, heave and pitch, the pressure inside each OWC device as well as the mooring line tensions at the fairleads. It is noted that HAMVAB outputs all the data as dimensionless numbers, e.g., like Eq. (3.23) for RAOs, however, most of the depicted data were fixed to represent real values per wave amplitude, except for the line tensions as they are compared with their respective MBL. In more detail, $RAO_5$ values were multiplied with the wave number k and dimensionless pressure values with $\rho \cdot g = 1.025 \cdot 9.81 =$ tn $\cdot$ m/s. To derive the maximum line tensions, a maximum significant wave height was set at $H_s = 7$ m.

As far as results are concerned, Fig. 3.7 to 3.9 display the different cases of wave direction. It is noted that HAMVAB assumes that the default wave direction of 0 deg travels from negative to positive x axis. Regarding RAOs, higher values in surge motion are depicted in the lower frequency range which corresponds to extreme sea-states. In heave and pitch, the little responses appearing at the TLP case are expected, as by definition the mooring system is more rigid, whereas catenaries show similar behavior among themselves with slightly higher heave responses in the mooring system consisting of wire ropes. Catenary system responses are also shown to be close to the ones of the free-floating case, except for pitch motion, where the peak of the figure is shifted in more extreme conditions range, yet free-floating structures are never considered feasible projects due to station-keeping criteria. Although the significantly higher RAOs of the examined mooring systems, chamber pressure distributions in the frequency domain do not reveal a similar behavior, i.e., the respective values corresponding to the examined cases are relatively close, which justifies that slack moorings are also a great solution, as in general, higher pressures correspond to greater absorbed energy. Moreover, it is shown that higher pressure values are always developed in the windward OWCs, however, depending on the wave direction, equivalent results occur in the leeward ones. Higher line tensions are also developed

on studless chains as well as on the windward lines accompanied with greater values in the extreme sea-state zones. However, maximum tensions on both studless chain and wire rope cases are way below the MBL designated limit (wire rope's MBL is not displayed because of its even higher value), which verify the reliability of the mooring lines' strength on ultimate limit states. Regarding the spikes that line tensions show in the very low frequency range, which surpass the 55% of MBL, it is assumed that are not a cause for concern, as no such sea-states occur in our examined locations presented in Chapter 2. Finally, comparing the variables based on wave direction, it is evident that RAOs and fairlead line tensions decrease with the wave angle increase. Regarding chamber pressures, they follow similar behavior among the wave direction cases, while among the mooring system cases, catenaries and TLP are close, especially in the average operational frequency range ($\omega > 0.75$ rad/s).

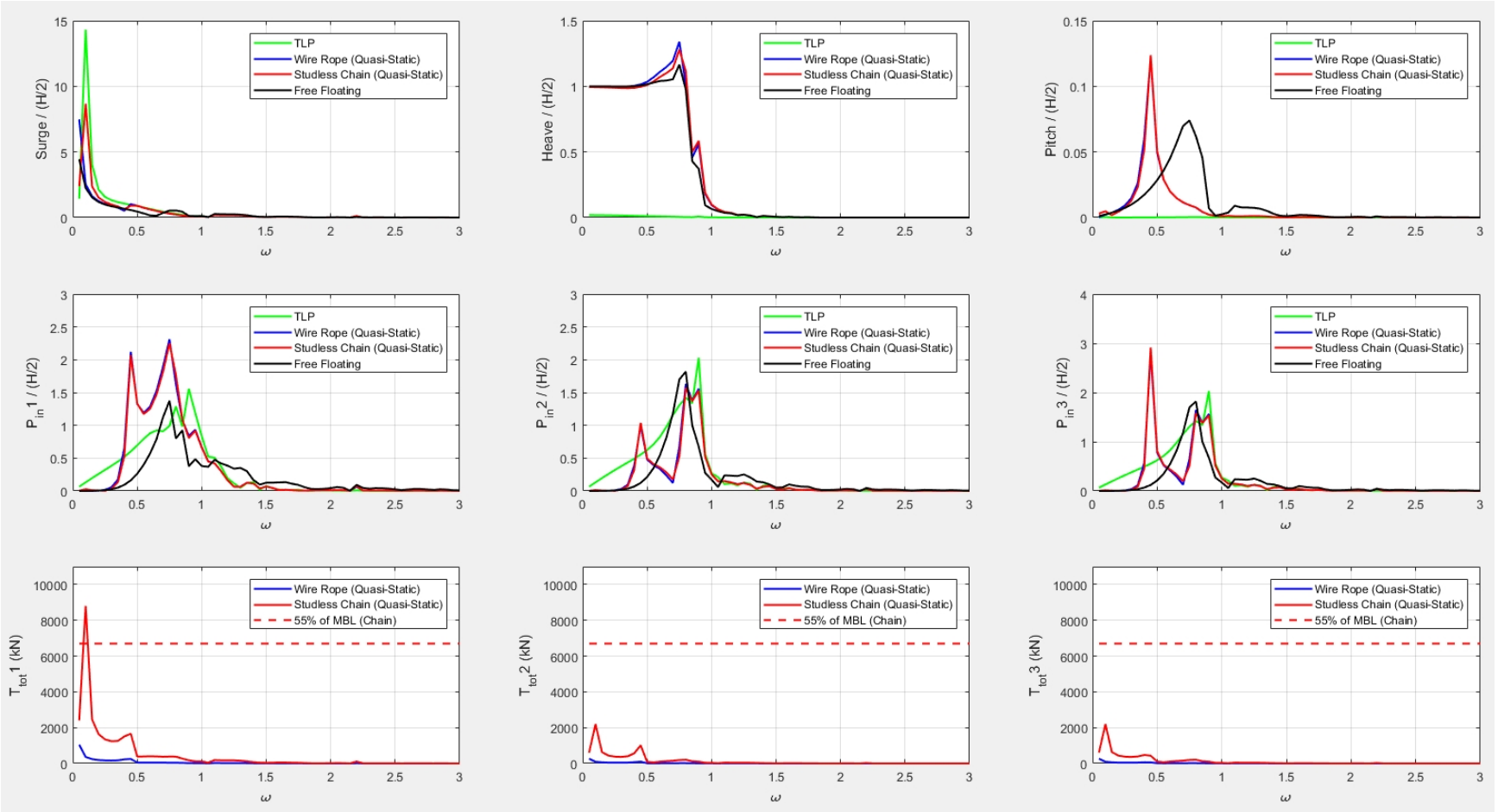


Figure 3.7: Results from coupled analysis using HAMVAB comparing the cases of TLP, free-floating, wire rope and studless chain catenaries excited by a wave of 0 deg direction. First row: Surge, Heave and Pitch RAOs. Second row: Pressure RAOs in the three chambers of OWCs. Third row: Maximum line tensions at fairleads compared with MBLs. The wire rope's MBL is not displayed due to its higher value.

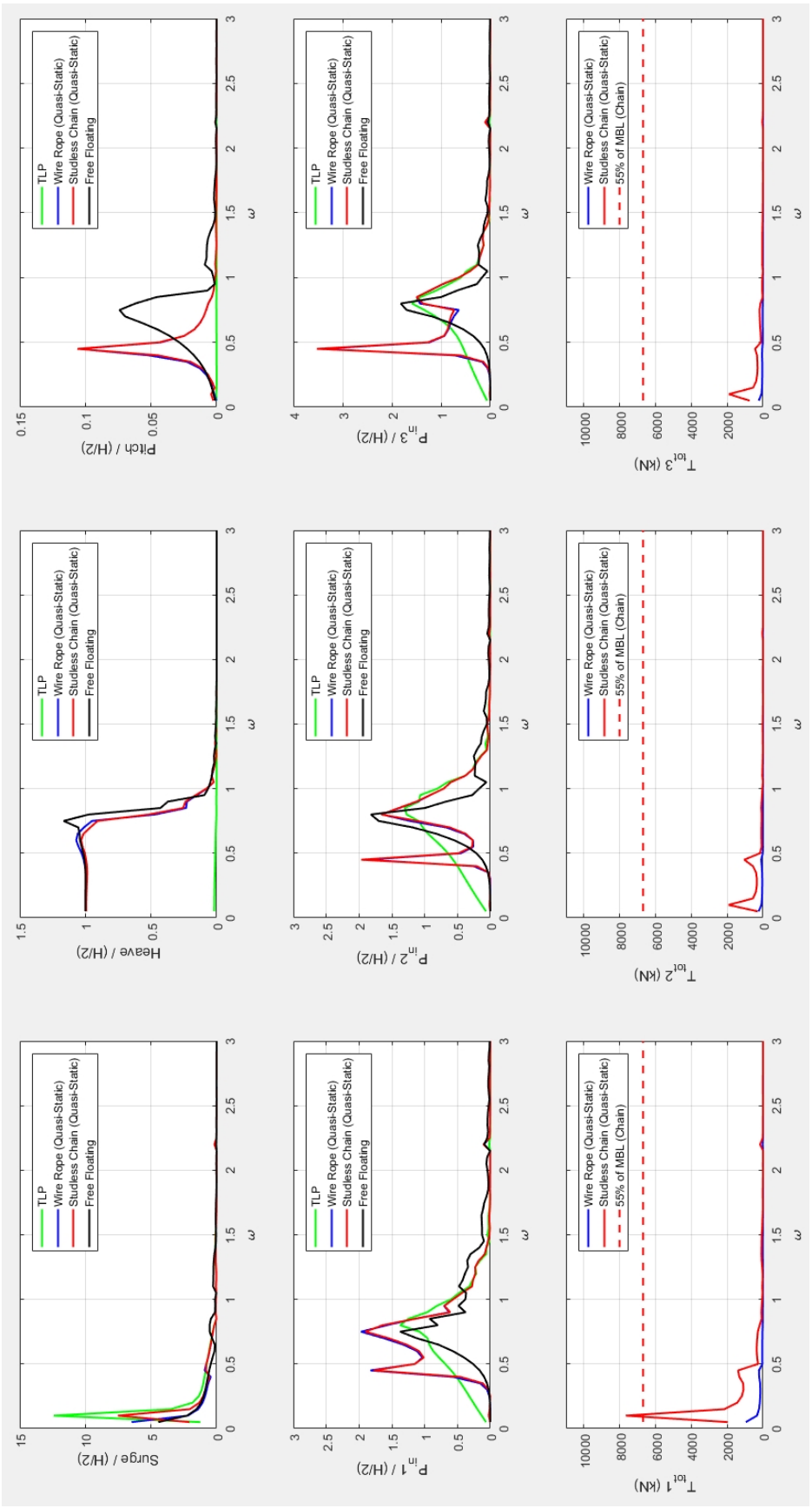


Figure 3.8: Results from coupled analysis using HAMVAB comparing the cases of TLP, free-floating, wire rope and studless chain catenaries excited by a wave of 30 deg direction. First row: Surge, Heave and Pitch RAOs. Second row: Pressure RAOs in the three chambers of OWCs. Third row: Maximum line tensions at fairleads compared with MBLs. The wire rope's MBL is not displayed due to its higher value.

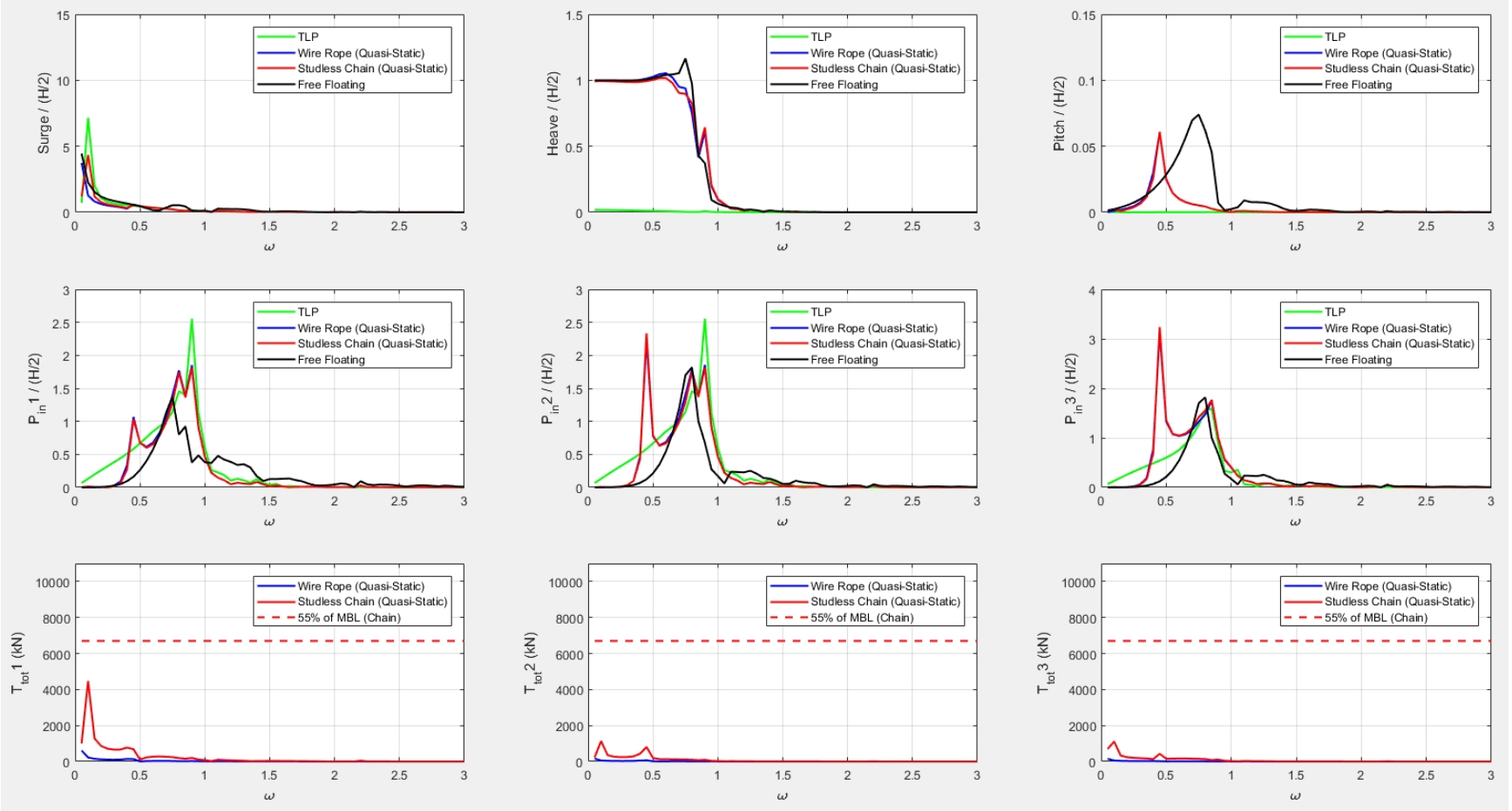


Figure 3.9: Results from coupled analysis using HAMVAB comparing the cases of TLP, free-floating, wire rope and studless chain catenaries excited by a wave of 60 deg direction. First row: Surge, Heave and Pitch RAOs. Second row: Pressure RAOs in the three chambers of OWCs. Third row: Maximum line tensions at fairleads compared with MBLs. The wire rope's MBL is not displayed due to its higher value.

### 3.4.3 Dynamic approach

Until now, the mooring system analysis was limited in a very conservative approach. As mentioned previously, the quasi-static model supports the idea of a uniform and linear motion between two static positions under constant loading, neglecting dynamics and leading to overestimation of the platform's responses. To take into account dynamic effects, the dynamic approach presented in Subsection 3.3.2 was followed regarding the studless chain mooring system. The wire rope case was not further investigated as it is assumed to be a non-efficient and uneconomical solution, due to the very large line length, the potentially increased abrasion due to friction with the seabed as well as the special design and installation method required for the anchor-line connection joint. Moreover, it is noted that in this study, the dynamic analysis of the lines is taking into account effects only due to the line motion in the water i.e., fluid inertia (added mass) and viscosity related effects (drag forces), and neglects the change of the touch-down point along the length of the line due to the constant motion. Further influences from phenomena that are already mentioned in a previous section e.g., VIVs, seabed interaction etc., are also not considered.

For conducting the dynamic analysis, the following procedure was followed. Firstly, the NTRANS software was executed by initially setting the free-floating motion data and extracting the total dynamic stiffness and damping matrices with respect to the global coordinate system. Due to the fact that inputs refer to single frequency cases, a small number of $\omega$ values was selected to be investigated. For accelerating the convergence procedure, the coupled analysis was continued in Matlab with a script solving Eq. (3.10), yet without the effect of pressure. The iterative process based on the surge and heave motions was continued until convergence and the same procedure was performed again running HAMVAB, instead of the Matlab code, to take into account the coupled effect of pressure and extract the final results. Regarding the examined frequencies, the range [0.9 rad/s, 1.15 rad/s] was investigated, as it corresponds to frequently observed sea-states. It is also considered that $C_{22}$ and $B_{22}$ values of the dynamic stiffness and damping matrices with respect to the local coordinate system were zero, in order to define the total global matrices with more parsimony. Tab. 3.10 presents the surge and heave responses as well as the absorbed wave energy by the OWCs. It can be observed that the heave responses of the TLP hybrid structure attain the least values compared to the quasi-static and dynamic cases. On the other hand, the absorbed wave energy ($Eabs$) from the TLP structure is higher than the corresponding values of the other two examined mooring cases, for $\omega = 0.95$ rad/s

and $\omega = 1$ rad/s. For these two frequencies, the total dynamic stiffness and damping matrices with respect to the global coordinate system are shown in Tab. 3.11 to 3.14. The rest examined frequencies show increased *Eabs* values that surpass the respective ones from the TLP case. Even though it is a bit contradictory, further analysis and investigation in a broader range of frequencies is needed to verify the impossibility of such behavior, along with a less biased definition of dynamic stiffness and damping matrices.

Table 3.10: Dimensionless data results for the dynamic analysis and comparison with the respective data from the TLP case and the quasi-static (QS) approach.

| | | $\omega$ rad/s | | | | | |
|---|---|---|---|---|---|---|---|
| | | 0.90 | 0.95 | 1.00 | 1.05 | 1.10 | 1.15 |
| Surge | TLP | 0.1100 | 0.1147 | 0.1225 | 0.0375 | 0.2284 | 0.2124 |
| | Chain QS | 0.0784 | 0.0884 | 0.0992 | 0.0311 | 0.1976 | 0.1828 |
| | Chain Dyn | 0.1956 | 0.0922 | 0.0925 | 0.0257 | 0.2048 | 0.1857 |
| Heave | TLP | 0.0073 | 0.0026 | 0.0016 | 0.0013 | 0.0010 | 0.0010 |
| | Chain QS | 0.5845 | 0.1889 | 0.0985 | 0.0630 | 0.0424 | 0.0357 |
| | Chain Dyn | 0.1636 | 0.0582 | 0.0393 | 0.0327 | 0.0286 | 0.0317 |
| Eabs | TLP | 0.8430 | 0.1533 | 0.0600 | 0.0247 | 0.0179 | 0.0103 |
| | Chain QS | 0.4223 | 0.1036 | 0.0401 | 0.0165 | 0.0142 | 0.0077 |
| | Chain Dyn | 0.9162 | 0.1240 | 0.0508 | 0.0304 | 0.0247 | 0.0166 |

Table 3.11: Total dynamic stiffness matrix (in $[kN/m; kNm]$) of the entire mooring system consisting of studless chains with respect to the global coordinate system for $\omega = 0.95$ rad/s.

| | | | | | |
|---|---|---|---|---|---|
| −93.570 | 0 | 0 | 0 | 1871.400 | 0 |
| 0 | 0 | 0 | 0 | 0 | 0 |
| 0 | 0 | −6.273 | 0 | −0.021 | 0 |
| 0 | 0 | 0 | −2613.750 | 0 | 0 |
| 1871.400 | 0 | −0.021 | 0 | −40041.597 | 0 |
| 0 | 0 | 0 | 0 | 0 | −19493.750 |

Table 3.12: Total damping matrix (in $[kN/m; kNm]$) of the entire mooring system consisting of studless chains with respect to the global coordinate system for $\omega = 0.95$ rad/s.

| | | | | | |
|---|---|---|---|---|---|
| 6.749 | 0 | 0 | 0 | −134.970 | 0 |
| 0 | 0 | 0 | 0 | 0 | 0 |
| 0 | 0 | 49.263 | 0 | 0.164 | 0 |
| 0 | 0 | 0 | 20526.250 | 0 | 0 |
| −134.970 | 0 | 0.164 | 0 | 23224.446 | 0 |
| 0 | 0 | 0 | 0 | 0 | 1405.938 |

Table 3.13: Total dynamic stiffness matrix (in $[kN/m; kNm]$) of the entire mooring system consisting of studless chains with respect to the global coordinate system for $\omega = 1$ rad/s.

| | | | | | |
|---|---|---|---|---|---|
| −121.061 | 0 | 0 | 0 | 2421.210 | 0 |
| 0 | 0 | 0 | 0 | 0 | 0 |
| 0 | 0 | −26.343 | 0 | −0.088 | 0 |
| 0 | 0 | 0 | −10976.250 | 0 | 0 |
| 2421.210 | 0 | −0.088 | 0 | −59399.806 | 0 |
| 0 | 0 | 0 | 0 | 0 | −25220.938 |

Table 3.14: Total damping matrix (in $[kN/m; kNm]$) of the entire mooring system consisting of studless chains with respect to the global coordinate system for $\omega = 1$ rad/s.

| | | | | | |
|---|---|---|---|---|---|
| 9.218 | 0 | 0 | 0 | −184.350 | 0 |
| 0 | 0 | 0 | 0 | 0 | 0 |
| 0 | 0 | 3.387 | 0 | 0.011 | 0 |
| 0 | 0 | 0 | 1411.250 | 0 | 0 |
| −184.350 | 0 | 0.011 | 0 | 5098.167 | 0 |
| 0 | 0 | 0 | 0 | 0 | 1920.313 |

## 3.5 Further Reading

The scientific community is constantly improving simulation methods to mimic physical phenomena and their effects on structures. Regarding the modeling and analysis of complex floating systems such as offshore wind turbines, a simulation tool called FAST has been developed to perform coupled aero-hydro-servo-elastic analyses [92]. Further efforts for improvements have generated models to include combined aero-hydro-dynamic damping, additional platform degrees of freedom, the platform mooring system and tower side-side motion, as well as gyroscopic effects [93], while additional damping caused by the operating rotor, so-called aerodynamic damping, has been also considered in studies yielding important results for surge and pitch responses [94].

As far as materials are concerned, apart from steel wire and chains, the synthetic mooring line is getting more and more attention in recent decades due to its economy and good performance. The characteristics of synthetic lines are very complex, and an intensive study is needed to investigate the stress-strain properties, fatigue, durability and creep among others. Engineering-wise, for a polyester mooring system, the level of pretension is governed by the criterion of maximum offset that the platform can accept, whereas for the HMPE and aramid which are much stiffer materials than the polyester, the maximum offset criterion is not critical any longer. For these two materials, the level of pretension is set to satisfy the criterion of minimum tension required to prevent failure due to compression fatigue and they are more competitive in deeper waters, due to lower density and higher stiffness, mitigating the overall costs [95]. Compared to the polyester, a more cost-effective component is nylon, mainly because of its lower stiffness and a corresponding capacity of reducing maximum tensions in the mooring system. However, the nonlinear behaviors of nylon ropes (e.g., load-elongation properties, fatigue characteristics, etc.) complicate the design and modeling of such systems. Regarding multi-material mooring lines, the chain-nylon-chain configuration is shown to be more advantageous than chain-polyester-chain, in terms of reducing the required mooring line lengths and tension responses [96]. For such configurations, an improved method has been proposed to accurately consider the mooring line segments and estimate mooring damping of single- and multi-component mooring lines [97].

In the context of dynamic load reduction and station keeping, a state-of-the-art system, so-called Intelligent Mooring System (IMS), has been developed and tested comparing its innovative operation with the respective responses of a spar, a semisub-

mersible and a TLP platform. IMS is a hydraulic based mooring tether that has the capability of providing non-linear and variable stiffness characteristics, achieved through active control. This non-linear load-response behavior could function like a "shock absorber" in the mooring system, and hence reduce the line tensions, enabling a more efficient mooring system that necessitates a lower MBL and thus lower cost [98]. An alternative solution for FOWT station keeping is the taut-leg mooring systems that are not examined thoroughly herein. Unlike the catenary mooring line, the taut mooring acts like a straight line under the effect of pretension and the restoring force comes from the axial stretching. Mooring pretension has significant effect on mooring damping, stiffness and mooring tensions, reducing the motion response of the floater. Although taut moorings are a good choice for deep-water installations, the special anchors that are needed to handle the large vertical load are expensive and a hurdle for mass manufacturing and utilization [99]. Additionally, the "string stiffness" effect must be considered, as in this case becomes even more relevant not only for peculiar arrangements of taut moorings, but also for particular and symmetric configurations [100]. More on assessing the stiffness of a mooring system and the damping achieved by cable or synthetic lines can be found respectively in [16, 101].

# Chapter 4

# Energy Output and Efficiency

## 4.1 Offshore wind energy

During its operation phase, the installed wind turbine, i.e., the DTU 10 MW RWT, will be producing energy continuously except for the maintenance periods or the respective hours with wind conditions outside the operation range. Offshore sites are characterized by strong and steady wind regime, so a high energy output is anticipated. Before proceeding to energy estimations, it is necessary to acquire information about the power curve of the turbine, which refers to the power the machine produces depending on the wind speed. The power curve of the DTU 10MW RWT can be seen in Fig. 4.1, whereas values of the steep part of the curve are shown in Tab. 4.1. It is recalled that the cut-in – cut-out range is [4, 25] m/s, the rated speed is 11.4 m/s, while the manufacturer states that the rated power is 10640 kW (NREL).

Table 4.1: Power values vs. wind speed of the DTU 10MW RWT. Source: Adapted from NREL.

| Wind speed (m/s) | 4 | 5 | 6 | 7 | 8 | 9 | 10 | 11 | 12-25 |
|---|---|---|---|---|---|---|---|---|---|
| Power (kW) | 280 | 800 | 1530 | 2500 | 3730 | 5310 | 7290 | 9700 | 10640 |

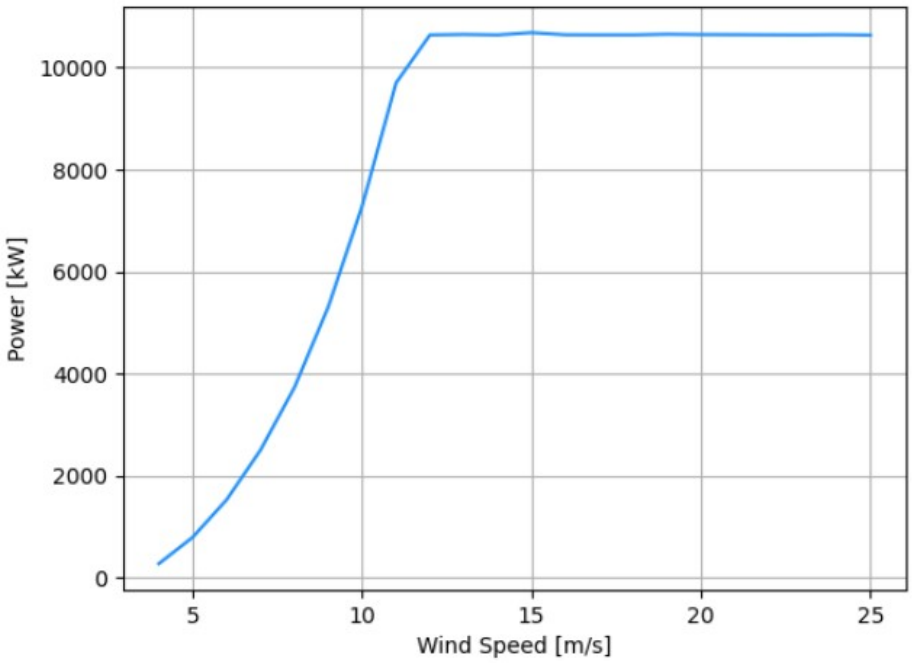


Figure 4.1: Power curve of the DTU 10MW RWT. Source: NREL.

The produced energy will be calculated regarding the three examined locations mentioned in Chapter 2. However, the wind speed timeseries refer to 100 m asl, while the hub height of the DTU 10MW RWT is 119 m and thus, the data were adjusted accordingly given that

$$u_{h_2} = u_{h_1} \frac{\ln \frac{h_2}{z_0}}{\ln \frac{h_1}{z_0}} \tag{4.1}$$

where $u_{h_2}$ (m/s) is the calculated wind speed at height $h_2$ (m), $u_{h_1}$ (m/s) is the known wind speed at height $h_1$ (m), and $z_0$ (m) is the roughness length equal to 0.0002 m for neutral atmospheric conditions. Having this fixed, the mean annual energy as well as the monthly mean energy can be estimated, analyzing the 20-year datasets. For the former one, each year is analyzed separately, while for the latter, a monthly clustering is needed. Lastly, due to the fact that the timeseries are in 1-hour timestep, the sum of the power values that correspond to the wind speed data based on the power curve, will result in the sought-for energy. It is noted that every wind speed value is matched to its respective power through linear interpolation between the known curve data, whereas the results for every examined location are shown in Fig. 4.2 and 4.3.

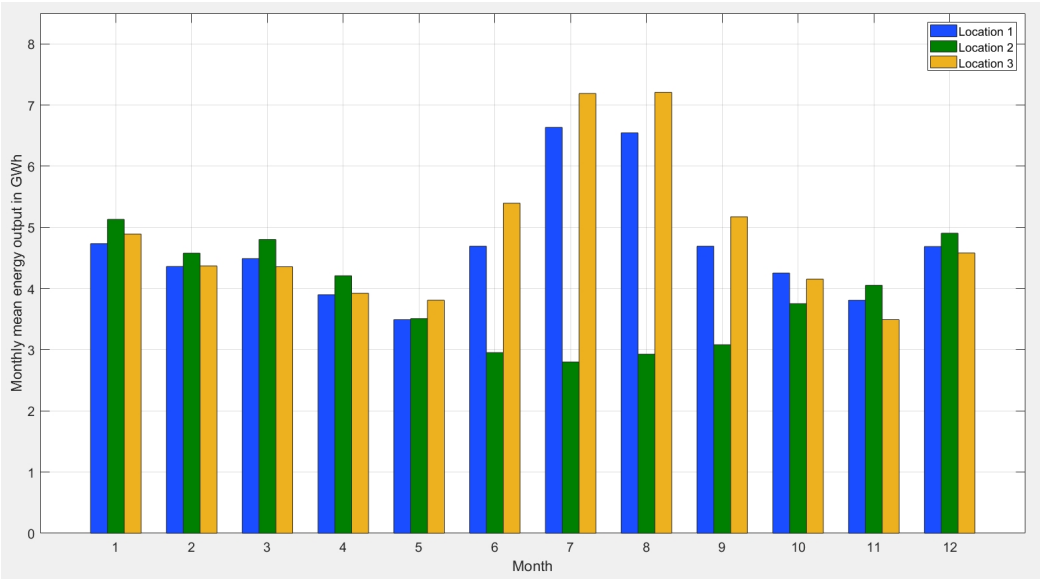


Figure 4.3: Monthly mean energy output in $GWh$ for the three examined locations (L1 in blue, L2 in green, L3 in orange) based on 20-year datasets.

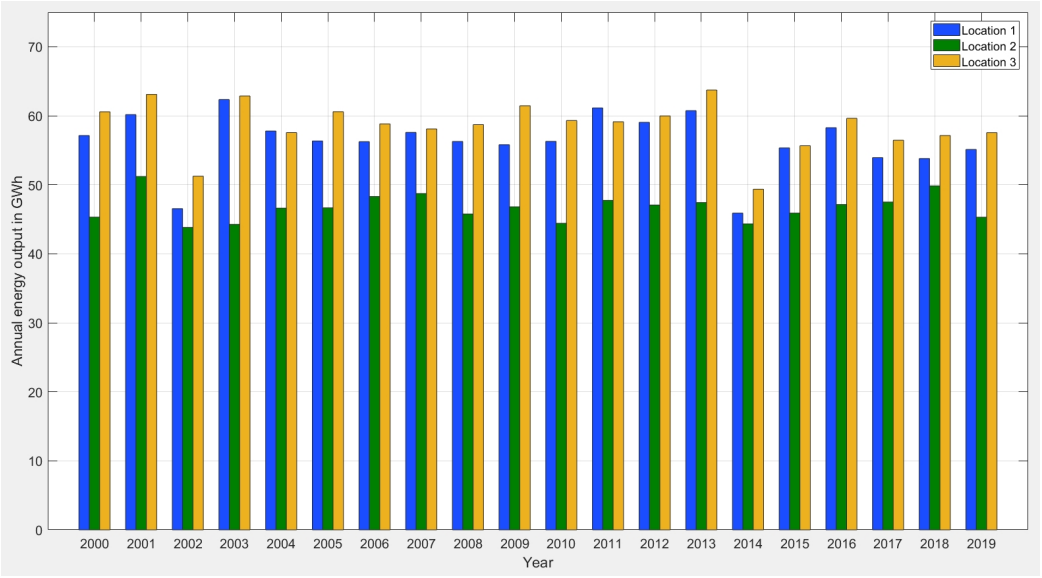


Figure 4.2: Annual energy output in $GWh$ for the three examined locations (L1 in blue, L2 in green, L3 in orange) from 2000 until 2019 (20-year datasets).

Regarding the three locations, the annual energy output is relatively higher in L1 and L3 than in L2, while the same is observed in the summer period at the respective monthly mean values (6.5 – 7 GWh on average in July and August). The exact opposite phenomenon can be seen to occur in the winter period, yet in a much lower intensity. The aforementioned observations verify and prove the presence of the strong

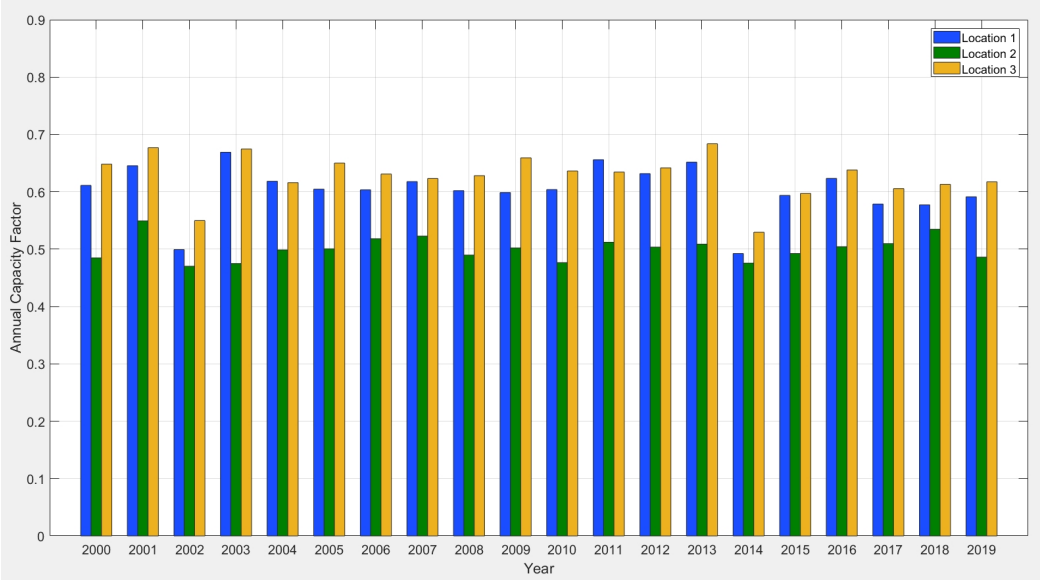


Figure 4.4: Annual capacity factor for the three examined locations (L1 in blue, L2 in green, L3 in orange) from 2000 until 2019 (20-year datasets).

Etesian winds in the Aegean Sea, which mostly affect L1 and L3 in our case. As far as energy output is concerned, these locations produce 56.30 GWh/y and 58.55 GWh/y on average respectively, while for L2 the production is limited to 46.70 GWh/y. In general, seasonal periodicity is clearly shown in the monthly results, while similar conclusions for inter-annual cycles require longer datasets.

Last but not least, the capacity factor (CF) is calculated for every site and year (Fig. 4.4). Capacity factor is the ratio of the actual energy produced in a given period, to the hypothetical maximum possible, i.e., running full time at rated power. In our case, full time at rated power equals to 365d $\times$ 24h $\times$ 10640kW = 93206400 kWh/y, and results correspond to the produced energy depicted in Fig. 4.2. Regarding the discussed locations, L1 and L3 appear to be really promising sites with CFs of 60.4% and 62.8% on average respectively, while L2 is also a very reliable choice with a CF of 50.1%. Such CF values are relatively much higher than the ones that appear in a typical onshore project, yet in these sites the very high percentages of the available wind data between the range of [4, 25] m/s (86.5% for L1, 81.3% for L2 and 87.5 for L3) were theoretically capable of operating the wind turbine. Consequently, the strong wind regime in these offshore locations may render such projects as both reliable and promising for financially feasible production of green energy.

## 4.2 Wave energy

In general, as far as wave energy converters are concerned, it is necessary to evaluate the produced energy depending on the installation site conditions and the device type. From a mathematical scope, a simple approximate analytical solution has been derived for the efficiency of wave energy absorption of an OWC wave energy device [102]. However, due to the fact that moored structures are discussed in this work, the influence of the mooring system cannot be neglected as it alters the structure's responses. Such work, comparing a TLP and a catenary mooring system towards the OWC's efficiency, has proven the former as the most efficient case in the entire band of the examined wave frequencies [103]. Although, the benefits of this higher efficiency are more than important, they are mitigated due to the high construction and installation costs of the TLP moorings, which set the motivation for further investigation on more economic solutions.

Installing the REFOS platform at the locations presented in Chapter 2, OWC devices will produce energy depending on the wave climate and the structure's responses. The procedure of calculating the wave energy from the OWCs will be discussed in detail. Firstly, the final data derived from the analysis performed in Chapter 2, regarding the three examined installation sites, were further analyzed to construct the tables of sea-state occurrences (Tab. 4.2 to 4.4).

Table 4.2: Sea-state occurrences of Location 1 analyzing 20-year data of 1-hour timestep. Highest value is depicted in bold.

| Peak Wave | Significant Wave Height $H_s$ (m) | | | | | |
|---|---|---|---|---|---|---|
| Period $T_p$ (s) | $0-1$ | $1-2$ | $2-3$ | $3-4$ | $4-5$ | $5-6$ |
| $1-2$ | 3 | 0 | 0 | 0 | 0 | 0 |
| $2-3$ | 5948 | 0 | 0 | 0 | 0 | 0 |
| $3-4$ | 41945 | 9 | 0 | 0 | 0 | 0 |
| $4-5$ | **48280** | 16770 | 0 | 0 | 0 | 0 |
| $5-6$ | 6733 | 39206 | 1053 | 0 | 0 | 0 |
| $6-7$ | 118 | 3321 | 9563 | 157 | 0 | 0 |
| $7-8$ | 1 | 74 | 569 | 1294 | 64 | 0 |
| $8-9$ | 0 | 0 | 1 | 34 | 157 | 13 |
| $9-10$ | 0 | 0 | 0 | 0 | 1 | 6 |
| $10-11$ | 0 | 0 | 0 | 0 | 0 | 0 |
| $11-12$ | 0 | 0 | 0 | 0 | 0 | 0 |

Table 4.3: Sea-state occurrences of Location 2 analyzing 20-year data of 1-hour timestep. Highest value is depicted in bold.

| Peak Wave | Significant Wave Height $H_s$ (m) | | | | | |
|---|---|---|---|---|---|---|
| Period $T_p$ (s) | $0-1$ | $1-2$ | $2-3$ | $3-4$ | $4-5$ | $5-6$ |
| $1-2$ | 11 | 0 | 0 | 0 | 0 | 0 |
| $2-3$ | 597 | 0 | 0 | 0 | 0 | 0 |
| $3-4$ | 17707 | 2 | 0 | 0 | 0 | 0 |
| $4-5$ | **51890** | 8266 | 0 | 0 | 0 | 0 |
| $5-6$ | 23392 | 30663 | 412 | 0 | 0 | 0 |
| $6-7$ | 3893 | 15396 | 7895 | 72 | 0 | 0 |
| $7-8$ | 309 | 3949 | 4515 | 1609 | 44 | 0 |
| $8-9$ | 1 | 839 | 1421 | 963 | 377 | 19 |
| $9-10$ | 0 | 107 | 381 | 315 | 119 | 15 |
| $10-11$ | 0 | 0 | 48 | 48 | 21 | 8 |
| $11-12$ | 0 | 0 | 0 | 2 | 4 | 10 |

Table 4.4: Sea-state occurrences of Location 3 analyzing 20-year data of 1-hour timestep. Highest value is depicted in bold.

| Peak Wave | Significant Wave Height $H_s$ (m) | | | | | |
|---|---|---|---|---|---|---|
| Period $T_p$ (s) | $0-1$ | $1-2$ | $2-3$ | $3-4$ | $4-5$ | $5-6$ |
| $1-2$ | 0 | 0 | 0 | 0 | 0 | 0 |
| $2-3$ | 12 | 0 | 0 | 0 | 0 | 0 |
| $3-4$ | 11284 | 0 | 0 | 0 | 0 | 0 |
| $4-5$ | **63374** | 1932 | 0 | 0 | 0 | 0 |
| $5-6$ | 27057 | 46706 | 32 | 0 | 0 | 0 |
| $6-7$ | 2121 | 13860 | 6033 | 10 | 0 | 0 |
| $7-8$ | 12 | 472 | 1424 | 900 | 7 | 0 |
| $8-9$ | 0 | 0 | 4 | 46 | 34 | 0 |
| $9-10$ | 0 | 0 | 0 | 0 | 0 | 0 |
| $10-11$ | 0 | 0 | 0 | 0 | 0 | 0 |
| $11-12$ | 0 | 0 | 0 | 0 | 0 | 0 |

In the REFOS case, two Wells-type air turbines were installed in each OWC. The pneumatic admittance $\Lambda$ of each OWC device equals to 343.848 $m^5/(kN{\cdot}s)$ regarding the Mediterranean Sea [44]. In order to estimate the absorbed energy from the de-

vices, the JONSWAP spectrum, provided by DNV [104] and results from HAMVAB, should be utilized. The HAMVAB software outputs the dimensionless absorbed energy, $Eabs'$, however, in order to derive the sought-for wave energy, the RAO of the absorbed power, $Eabs$ (divided by $(H/2)^2$), is required which equals to:

$$Eabs = Eabs' \cdot \omega \cdot \rho \cdot g \cdot \alpha^2 \tag{4.2}$$

where $\omega$ is the frequency in rad/s, $\rho = 1.025$ tn/m$^3$, $g = 9.81$ m/s$^2$ and $\alpha = 15.5$ m the outer radius of each individual cylinder of the OWC configuration. Regarding the JONSWAP spectrum $S_J(\omega)$, which corresponds to developing sea-states in fetch limited situations, it is formulated via the Pierson-Moskowitz (PM) spectrum $S_{PM}(\omega)$ that describes fully developed seas, as follows:

$$S_J(\omega) = A_\gamma \, S_{PM}(\omega) \, \gamma^{exp\left(-0.5\left(\frac{\omega-\omega_p}{\sigma\omega_p}\right)^2\right)} \tag{4.3}$$

where:

$\omega_p = \frac{2\pi}{T_p}$ the spectral peak frequency in rad/s,

$A_\gamma = 1 - 0.287 \ln \gamma$ a normalizing factor,

$$\sigma = \begin{cases} 0.07 & \text{if } \omega < \omega_p \\ 0.09 & \text{if } \omega > \omega_p \end{cases} \quad \text{a spectral width parameter,}$$

$$\gamma = \begin{cases} e^{5.75-1.15\frac{T_p}{\sqrt{H_s}}} \text{ if } 3.6 < \frac{T_p}{\sqrt{H_s}} < 5 \\ 5 \text{ if } \frac{T_p}{\sqrt{H_s}} \leq 3.6 \\ 1 \text{ if } \frac{T_p}{\sqrt{H_s}} \geq 5 \end{cases} \quad \text{a non-dimensional peak shape parameter}$$

and

$$S_{PM}(\omega) = \tfrac{5}{16} \, H_s^2 \, \omega_p^4 \, \omega^{-5} \, exp\left(-\tfrac{5}{4}\left(\tfrac{\omega}{\omega_p}\right)^4\right)$$

Subsequently, the absorbed power per sea-state can be calculated via Eq. (4.4). At this stage, the results are independent of location, yet depend on the mooring system and wave direction. As mentioned in the previous chapter, the results between TLP and chain catenaries will be further discussed, however, the tables referring to the wire rope mooring system are attached in Appendix C. In Tab. 4.5 and 4.6, the calculations from Eq. (4.4) are depicted regarding 0 deg wave direction and the two

examined mooring systems, i.e., TLP and studless chain catenaries. The rest tables referring to 30 deg and 60 deg wave directions can be found also in the Appendix C.

$$P = \int 2\, Eabs\, S_J(\omega)\, d\omega \tag{4.4}$$

Finally, the real absorbed energy per sea-state is estimated by multiplying the tables of sea-state occurrences with the ones of the absorbed power and by dividing all the cell values with the 20 years of the examined data, in order to derive the mean annual absorbed energy per sea-state, per location and for every mooring system case. These results are shown in Tab. 4.7 to 4.12, again only for 0 deg wave direction regarding the three installation sites, while the rest cases are attached in Appendix C.

Table 4.5: Absorbed power in $kW$ for 0 deg wave direction and TLP system. Highest value is depicted in bold.

| Peak Wave | Significant Wave Height $H_s$ (m) | | | | | |
|---|---|---|---|---|---|---|
| Period $T_p$ (s) | $0-1$ | $1-2$ | $2-3$ | $3-4$ | $4-5$ | $5-6$ |
| $1-2$ | 0.00 | 0.00 | 0.00 | 0.00 | 0.00 | 0.00 |
| $2-3$ | 0.00 | 0.00 | 0.00 | 0.00 | 0.01 | 0.01 |
| $3-4$ | 0.01 | 0.08 | 0.21 | 0.42 | 0.70 | 1.04 |
| $4-5$ | 0.31 | 2.01 | 5.45 | 10.69 | 17.67 | 26.39 |
| $5-6$ | 3.65 | 28.94 | 61.03 | 119.62 | 197.75 | 295.40 |
| $6-7$ | 10.37 | 93.33 | 303.30 | 628.66 | 1039.20 | 1552.40 |
| $7-8$ | 15.35 | 138.14 | 421.30 | 1060.10 | 1949.00 | **2911.50** |
| $8-9$ | 17.15 | 154.35 | 428.75 | 887.11 | 1565.30 | 2417.40 |
| $9-10$ | 16.83 | 151.42 | 420.61 | 824.40 | 1355.60 | 2024.30 |
| $10-11$ | 15.50 | 139.51 | 387.53 | 759.56 | 1250.60 | 1809.10 |
| $11-12$ | 13.86 | 124.73 | 346.48 | 679.11 | 1122.60 | 1656.70 |

Table 4.6: Absorbed power in $kW$ for 0 deg wave direction and studless chain mooring system. Highest value is depicted in bold.

| Peak Wave | Significant Wave Height $H_s$ (m) | | | | | |
|---|---|---|---|---|---|---|
| Period $T_p$ (s) | $0-1$ | $1-2$ | $2-3$ | $3-4$ | $4-5$ | $5-6$ |
| $1-2$ | 0.00 | 0.00 | 0.00 | 0.00 | 0.00 | 0.00 |
| $2-3$ | 0.00 | 0.01 | 0.03 | 0.06 | 0.10 | 0.14 |
| $3-4$ | 0.01 | 0.07 | 0.19 | 0.38 | 0.63 | 0.94 |
| $4-5$ | 0.21 | 1.40 | 3.81 | 7.47 | 12.35 | 18.44 |
| $5-6$ | 2.46 | 19.64 | 42.08 | 82.49 | 136.35 | 203.69 |
| $6-7$ | 8.29 | 74.64 | 216.37 | 424.74 | 702.13 | 1048.90 |
| $7-8$ | 13.62 | 122.62 | 375.23 | 956.95 | 1775.70 | **2652.60** |
| $8-9$ | 16.04 | 144.34 | 400.95 | 874.59 | 1632.20 | 2608.80 |
| $9-10$ | 16.67 | 150.05 | 416.81 | 816.95 | 1339.80 | 1991.50 |
| $10-11$ | 17.29 | 155.60 | 432.22 | 847.16 | 1391.90 | 1968.20 |
| $11-12$ | 18.26 | 164.35 | 456.52 | 894.78 | 1479.10 | 2181.40 |

Table 4.7: Annual absorbed energy in $kWh/y$ for 0 deg wave direction and TLP system in Location 1. Highest value is depicted in bold.

| Peak Wave | Significant Wave Height $H_s$ (m) | | | | | |
|---|---|---|---|---|---|---|
| Period $T_p$ (s) | $0-1$ | $1-2$ | $2-3$ | $3-4$ | $4-5$ | $5-6$ |
| $1-2$ | 0 | 0 | 0 | 0 | 0 | 0 |
| $2-3$ | 0 | 0 | 0 | 0 | 0 | 0 |
| $3-4$ | 27 | 0 | 0 | 0 | 0 | 0 |
| $4-5$ | 740 | 1682 | 0 | 0 | 0 | 0 |
| $5-6$ | 1227 | 56732 | 3213 | 0 | 0 | 0 |
| $6-7$ | 61 | 15497 | **145020** | 4935 | 0 | 0 |
| $7-8$ | 1 | 511 | 11986 | 68591 | 6237 | 0 |
| $8-9$ | 0 | 0 | 21 | 1508 | 12288 | 1571 |
| $9-10$ | 0 | 0 | 0 | 0 | 68 | 607 |
| $10-11$ | 0 | 0 | 0 | 0 | 0 | 0 |
| $11-12$ | 0 | 0 | 0 | 0 | 0 | 0 |

Table 4.8: Annual absorbed energy in $kWh/y$ for 0 deg wave direction and studless chain mooring system in Location 1. Highest value is depicted in bold.

| Peak Wave | Significant Wave Height $H_s$ (m) | | | | | |
|---|---|---|---|---|---|---|
| Period $T_p$ (s) | $0-1$ | $1-2$ | $2-3$ | $3-4$ | $4-5$ | $5-6$ |
| $1-2$ | 0 | 0 | 0 | 0 | 0 | 0 |
| $2-3$ | 0 | 0 | 0 | 0 | 0 | 0 |
| $3-4$ | 25 | 0 | 0 | 0 | 0 | 0 |
| $4-5$ | 502 | 1173 | 0 | 0 | 0 | 0 |
| $5-6$ | 829 | 38508 | 2216 | 0 | 0 | 0 |
| $6-7$ | 49 | 12393 | **103460** | 3334 | 0 | 0 |
| $7-8$ | 1 | 454 | 10675 | 61915 | 5682 | 0 |
| $8-9$ | 0 | 0 | 20 | 1487 | 12812 | 1696 |
| $9-10$ | 0 | 0 | 0 | 0 | 67 | 597 |
| $10-11$ | 0 | 0 | 0 | 0 | 0 | 0 |
| $11-12$ | 0 | 0 | 0 | 0 | 0 | 0 |

Table 4.9: Annual absorbed energy in $kWh/y$ for 0 deg wave direction and TLP system in Location 2. Highest value is depicted in bold.

| Peak Wave | Significant Wave Height $H_s$ (m) | | | | | |
|---|---|---|---|---|---|---|
| Period $T_p$ (s) | $0-1$ | $1-2$ | $2-3$ | $3-4$ | $4-5$ | $5-6$ |
| $1-2$ | 0 | 0 | 0 | 0 | 0 | 0 |
| $2-3$ | 0 | 0 | 0 | 0 | 0 | 0 |
| $3-4$ | 12 | 0 | 0 | 0 | 0 | 0 |
| $4-5$ | 795 | 829 | 0 | 0 | 0 | 0 |
| $5-6$ | 4263 | 44370 | 1257 | 0 | 0 | 0 |
| $6-7$ | 2018 | 71843 | **119730** | 2263 | 0 | 0 |
| $7-8$ | 237 | 27277 | 95108 | 85289 | 4288 | 0 |
| $8-9$ | 1 | 6475 | 30463 | 42715 | 29506 | 2297 |
| $9-10$ | 0 | 810 | 8013 | 12984 | 8066 | 1518 |
| $10-11$ | 0 | 0 | 930 | 1823 | 1313 | 724 |
| $11-12$ | 0 | 0 | 0 | 68 | 225 | 828 |

Table 4.10: Annual absorbed energy in $kWh/y$ for 0 deg wave direction and studless chain mooring system in Location 2. Highest value is depicted in bold.

| Peak Wave | Significant Wave Height $H_s$ (m) | | | | | |
|---|---|---|---|---|---|---|
| Period $T_p$ (s) | $0-1$ | $1-2$ | $2-3$ | $3-4$ | $4-5$ | $5-6$ |
| $1-2$ | 0 | 0 | 0 | 0 | 0 | 0 |
| $2-3$ | 0 | 0 | 0 | 0 | 0 | 0 |
| $3-4$ | 10 | 0 | 0 | 0 | 0 | 0 |
| $4-5$ | 540 | 578 | 0 | 0 | 0 | 0 |
| $5-6$ | 2880 | 30117 | 867 | 0 | 0 | 0 |
| $6-7$ | 1614 | 57454 | **85411** | 1529 | 0 | 0 |
| $7-8$ | 210 | 24211 | 84708 | 76987 | 3907 | 0 |
| $8-9$ | 1 | 6055 | 28487 | 42111 | 30766 | 2478 |
| $9-10$ | 0 | 803 | 7940 | 12867 | 7972 | 1494 |
| $10-11$ | 0 | 0 | 1037 | 2033 | 1462 | 787 |
| $11-12$ | 0 | 0 | 0 | 89 | 296 | 1091 |

Table 4.11: Annual absorbed energy in $kWh/y$ for 0 deg wave direction and TLP system in Location 3. Highest value is depicted in bold.

| Peak Wave | Significant Wave Height $H_s$ (m) | | | | | |
|---|---|---|---|---|---|---|
| Period $T_p$ (s) | $0-1$ | $1-2$ | $2-3$ | $3-4$ | $4-5$ | $5-6$ |
| $1-2$ | 0 | 0 | 0 | 0 | 0 | 0 |
| $2-3$ | 0 | 0 | 0 | 0 | 0 | 0 |
| $3-4$ | 7 | 0 | 0 | 0 | 0 | 0 |
| $4-5$ | 971 | 194 | 0 | 0 | 0 | 0 |
| $5-6$ | 4931 | 67585 | 98 | 0 | 0 | 0 |
| $6-7$ | 1100 | 64675 | **91490** | 314 | 0 | 0 |
| $7-8$ | 9 | 3260 | 29996 | 47707 | 682 | 0 |
| $8-9$ | 0 | 0 | 86 | 2040 | 2661 | 0 |
| $9-10$ | 0 | 0 | 0 | 0 | 0 | 0 |
| $10-11$ | 0 | 0 | 0 | 0 | 0 | 0 |
| $11-12$ | 0 | 0 | 0 | 0 | 0 | 0 |

Table 4.12: Annual absorbed energy in $kWh/y$ for 0 deg wave direction and studless chain mooring system in Location 3. Highest value is depicted in bold.

| Peak Wave | Significant Wave Height $H_s$ (m) | | | | | |
|---|---|---|---|---|---|---|
| Period $T_p$ (s) | $0-1$ | $1-2$ | $2-3$ | $3-4$ | $4-5$ | $5-6$ |
| $1-2$ | 0 | 0 | 0 | 0 | 0 | 0 |
| $2-3$ | 0 | 0 | 0 | 0 | 0 | 0 |
| $3-4$ | 7 | 0 | 0 | 0 | 0 | 0 |
| $4-5$ | 659 | 135 | 0 | 0 | 0 | 0 |
| $5-6$ | 3331 | 45875 | 67 | 0 | 0 | 0 |
| $6-7$ | 879 | 51722 | **65268** | 212 | 0 | 0 |
| $7-8$ | 8 | 2894 | 26716 | 43063 | 622 | 0 |
| $8-9$ | 0 | 0 | 80 | 2012 | 2775 | 0 |
| $9-10$ | 0 | 0 | 0 | 0 | 0 | 0 |
| $10-11$ | 0 | 0 | 0 | 0 | 0 | 0 |
| $11-12$ | 0 | 0 | 0 | 0 | 0 | 0 |

By adding all cell values, the total mean annual wave energy absorbed from the OWC devices is calculated for every case and final results are presented in Tab. 4.13. For better illustration, the results are also shown in Fig. 4.5. It is observed that Location 2 has the highest wave energy production, due to its strongest wave regime that depends on the greater fetch of the area, whereas comparing the other two installation sites, Location 3 shows the weakest results, perhaps due to the local conditions i.e., region with land nearby. As far as the mooring system is concerned, the TLP design shows the highest efficiency, as it is by definition the most rigid solution, however, the catenary mooring system also presents high energy production. Lastly, comparing all cases in terms of the wave direction, peak values appear when the excitation wave strikes at 60 deg, while the opposite is observed for the 30 deg wave. It is noted that all the above analysis was conducted in MATLAB, running code scripts developed by the author (Appendix B).

Table 4.13: Total mean annual absorbed energy in $MWh/y$ for every examined mooring system, wave direction and location.

| Moorings | Wave direction | Location 1 | Location 2 | Location 3 |
|---|---|---|---|---|
| TLP | 00 deg | 332.53 | 608.33 | 317.81 |
| | 30 deg | 244.71 | 463.93 | 233.88 |
| | 60 deg | 402.28 | 722.35 | 384.42 |
| Chain | 00 deg | 257.89 | 518.79 | 246.33 |
| | 30 deg | 251.70 | 496.22 | 240.37 |
| | 60 deg | 309.54 | 606.75 | 295.45 |

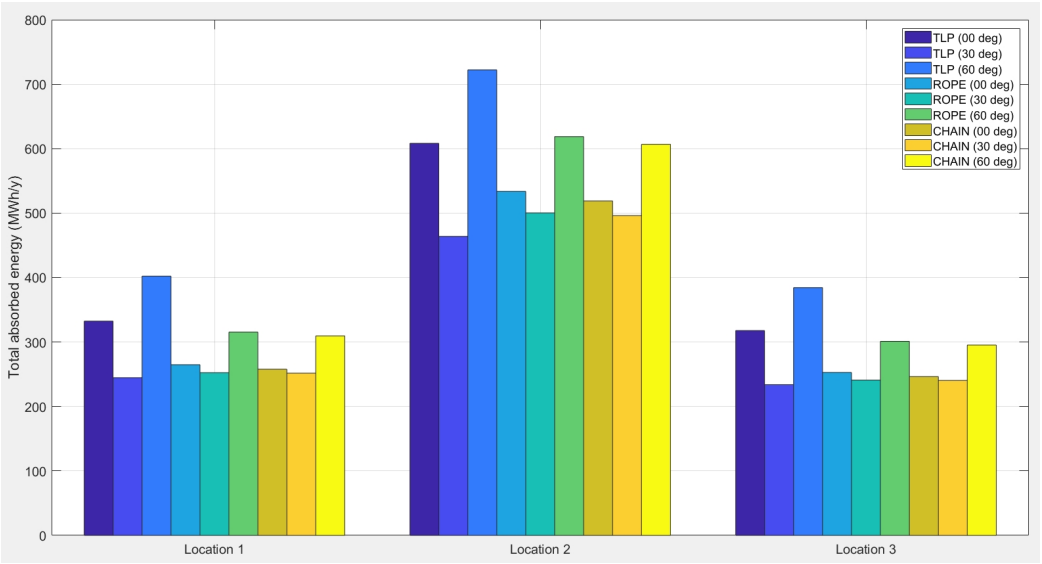


Figure 4.5: Total mean annual absorbed energy in $MWh/y$ for every examined mooring system (TLP, studless chain), wave direction (0 deg, 30 deg, 60deg) and location.

As far as the results of the dynamic analysis are concerned, wave energy calculations were performed regarding two frequencies; $\omega = 0.95$ rad/s and $\omega = 1.15$ rad/s. The reason behind this selection was that they correspond to the middle of the [6, 7] and [5, 6] peak wave period classes respectively, which present frequent occurrences, and supposing a normal distribution inside each class, wave energy outputs can be derived following a similar procedure that described above. Tab. 4.14 presents the results from the dynamic analysis along with the respective ones from TLP and quasi-static approach for comparison purposes. It is observed that for every examined location, peak values of wave energy in the investigated sea-states follow similar behavior with the criterion of absorbed energy that was mentioned in Chapter

3, i.e., *Eabs* values: TLP>Dyn>QS. However, for a more comprehensive overview of the produced wave energy, dynamic results for every frequency are necessary to yield the complete power tables for every installation site.

Table 4.14: Annual absorbed energy in $kWh/y$ for 0 deg wave direction regarding every location and comparing the TLP case with the two analysis approaches of the studless chain mooring system (quasi-static: QS and dynamic: Dyn). Highest values in every case are depicted in bold.

| Examined Cases | | Peak Wave Period $T_p$ (s) | Significant Wave Height $H_s$ (m) | | | | | |
|---|---|---|---|---|---|---|---|---|
| | | | $0-1$ | $1-2$ | $2-3$ | $3-4$ | $4-5$ | $5-6$ |
| L1 | TLP | 5-6 | 1227 | 56732 | 3213 | 0 | 0 | 0 |
| | | 6-7 | 61 | 15497 | **145020** | 4935 | 0 | 0 |
| | QS | 5-6 | 829 | 38508 | 2216 | 0 | 0 | 0 |
| | | 6-7 | 49 | 12393 | **103460** | 3334 | 0 | 0 |
| | Dyn | 5-6 | 470 | 24691 | 1864 | 0 | 0 | 0 |
| | | 6-7 | 52 | 13073 | **105050** | 3380 | 0 | 0 |
| L2 | TLP | 5-6 | 4263 | 44370 | 1257 | 0 | 0 | 0 |
| | | 6-7 | 2018 | 71843 | **119730** | 2263 | 0 | 0 |
| | QS | 5-6 | 2880 | 30117 | 867 | 0 | 0 | 0 |
| | | 6-7 | 1614 | 57454 | **85411** | 1529 | 0 | 0 |
| | Dyn | 5-6 | 1633 | 19311 | 729 | 0 | 0 | 0 |
| | | 6-7 | 1703 | 60604 | **86723** | 1550 | 0 | 0 |
| L2 | TLP | 5-6 | 4931 | 67585 | 98 | 0 | 0 | 0 |
| | | 6-7 | 1100 | 64675 | **91490** | 314 | 0 | 0 |
| | QS | 5-6 | 3331 | 45875 | 67 | 0 | 0 | 0 |
| | | 6-7 | 879 | 51722 | **65268** | 212 | 0 | 0 |
| | Dyn | 5-6 | 1888 | 29414 | 57 | 0 | 0 | 0 |
| | | 6-7 | 928 | 54558 | **66270** | 215 | 0 | 0 |

# Chapter 5

# Epilogue

## 5.1 Conclusions

Closing this thesis, it is highly useful to gather all the important conclusions regarding the stages of this study. Firstly, it is shown that higher threshold selection, than the one suggested from theory, gave great results in the EVA based on the diagnostic plots. All selections did not negate variance prerequisites and supported the bias-variance trade-off. Moreover, regarding return levels, the wave parameters referring to Location 3 showed the lowest results, perhaps due to nearby land, while the opposite occured for wind speed and Location 1, due to the strong winter and summer (Etesian) winds as well as the lack of near highland. As far as the ultimate limit state analysis is concerned, the results of EVA were not critical for the floating system. The maximum 100-year return values of the examined variables were around 30 m/s and 7 m for wind speed and significant wave height respectively at L1 and 12.5 s for peak wave period at L2. Assuming an extreme sea-state of $[H_s - T_p] = [7 - 12.5]$, the structure did not show any cause for concern. Similar conclusion can be derived for the wind turbine as it stops its operation above the 25 m/s wind speed value. Additional loads on the blades due to high winds were not investigated as they were not part of the current study, yet winds beyond the cut-out speed were extremely rare.

Regarding the analysis on the multi-purpose floating structure, the mooring systems consisting of wire ropes and studless chains showed similar behavior in terms of surge, heave and pitch responses as well as of inner OWC pressures. The chain case presented higher line tensions in general, but all fulfilling the criterion of 55% of the MBL. Peaks above this limit are located at the range of frequencies which

characterize extreme sea-states that do not occur in our three examined installation sites. The TLP concept is by default the most rigid and stable design, however, OWC chamber pressures are close among the different cases of moorings, even though the conservative quasi-static approach was followed. It is also noted that chain moorings were the main catenary system being investigated, as it is considered a more efficient and economical solution. For a more realistic analysis, dynamic effects were taken into account and frequencies in the range [0.9 rad/s, 1.15 rad/s] were investigated, as they correspond to frequently observed sea-states. For $\omega = 0.95$ rad/s and $\omega = 1$ rad/s, it was concluded that the values of heave motions and absorbed energy, between TLP and QS, holds TLP<Dyn<QS and TLP>Dyn>QS for the two examined variables respectively. The rest frequencies showed increased absorbed energy values that surpass the respective ones from the TLP case, yet further investigation in a broader range of frequencies is needed to verify such a contradictory behavior, given that TLP is the most rigid design.

As far as energy output is concerned, higher offshore wind energy is capable of being produced in Locations 1 and 3, due to the strong wind regime all year round. Location 2 is also a very promising site and showed a relatively high capacity factor, yet it presented the highest wave energy production, perhaps due to the greater fetch that characterizes the area and can host temporally longer swells. Regarding wave direction, the 60 deg wave gave the highest wave energy outputs overall, while the lowest results were derived from the 30 deg wave. Comparing the two main mooring systems in terms of efficiency, TLP represents the best case scenario. Expected results were also yielded with regard to the quasi-static and dynamic analyses. The dynamic approach presented higher peak wave energy production in the respective investigated sea-states. However, all frequency results are necessary to yield the complete power tables for every installation site and gain a more comprehensive overview of the energy status.

Considering all of the aforementioned facts regarding the research conducted for the purpose of the current work, it can be concluded that catenary mooring systems, and especially the ones consisting of studless chains, are a very competitive solution for multi-purpose floating structures or even floating wind turbines. Their performance in station-keeping as well as in ultimate limit states promise a reliable and robust design along with construction and installation financial feasibility. Such projects can become highly profitable, taking into account the decreased overall costs that lead to lower levelized cost of energy (LCOE).

## 5.2 Further Research

During the stages of this study, a lot of assumptions were made in order to balance theoretical approaches with reality and extract unbiased results. While they are not a source of significant distortions, it will be enlightening if many factors would be accounted for in future research activities. First and foremost, as far as data analysis is concerned, it is crucial to have access to unbiased and continuous in-situ measurements for the locations that are set to be examined for exploitation, as well as compare numerous methods of EVA and incorporate persistence phenomena, in terms of a more realistic study for extreme limit states. Secondly, efficient and robust indices should be developed for objective definition of profitable areas through stochastic dynamic models, taking into account historical metocean data, as well as financial metrics at any given time.

Engineering-wise, apart from the selection of different line type and configuration, e.g., multi-material lines with attached buoys etc., catenary mooring systems should be also studied regarding the dynamic responses of the lines, especially integrating VIVs, seabed interactions and internal damping due to friction between the chain links in the models, as well as avoiding snap loads and fatigue. The additional effects of mooring induced damping further decrease motions, which will probably increase the efficiency of the OWCs. Further examinations should be also performed regarding the offshore wind turbine performance, as applied coupled motions tilt the rotor and alter the turbine's operation. Last but not least, fatigue analyses and anchor design should be applied as well, while optimization on the air turbines of the OWCs would further contribute to make multi-purpose floating structures competitive in the energy market for offshore wind and wave co-exploitation.

# References


[1] C. F. Santos, C. N. Ehler, T. Agardy, F. Andrade, M. K. Orbach, and L. B. Crowder, "Marine spatial planning," in *World seas: An environmental evaluation*, pp. 571–592, Elsevier, 2019.

[2] GWEC, "Global offshore wind report," 2021.

[3] M. D. Esteban, J. J. Diez, J. S. López, and V. Negro, "Why offshore wind energy?," *Renewable energy*, vol. 36, no. 2, pp. 444–450, 2011.

[4] F. González-Longatt, P. Wall, and V. Terzija, "Wake effect in wind farm performance: Steady-state and dynamic behavior," *Renewable Energy*, vol. 39, no. 1, pp. 329–338, 2012.

[5] X. Sun, D. Huang, and G. Wu, "The current state of offshore wind energy technology development," *Energy*, vol. 41, no. 1, pp. 298–312, 2012.

[6] A. M. Forsting and N. Troldborg, "The effect of blockage on power production for laterally aligned wind turbines," in *Journal of Physics: Conference Series*, vol. 625, p. 012029, IOP Publishing, 2015.

[7] T. Nishino and R. H. Willden, "The efficiency of an array of tidal turbines partially blocking a wide channel," *Journal of Fluid Mechanics*, vol. 708, pp. 596–606, 2012.

[8] T. Nishino and S. Draper, "Local blockage effect for wind turbines," in *Journal of Physics: Conference Series*, vol. 625, p. 012010, IOP Publishing, 2015.

[9] IRENA, "Offshore renewables: An action agenda for deployment," 2021.

[10] GWEC, "Global wind report," 2022.

[11] S. Butterfield, W. Musial, J. Jonkman, and P. Sclavounos, "Engineering challenges for floating offshore wind turbines," tech. rep., National Renewable Energy Lab. (NREL), Golden, CO (United States), 2007.

[12] M. Cahay, E. Luquiau, C. Smadja, and F. Silvert, "Use of a vertical wind turbine in an offshore floating wind farm," in *Offshore technology conference*, OnePetro, 2011.

[13] Z. Jiang, "Installation of offshore wind turbines: A technical review," *Renewable and Sustainable Energy Reviews*, vol. 139, p. 110576, 2021.

[14] E. Uzunoglu, D. Karmakar, and C. Guedes Soares, "Floating offshore wind platforms," in *Floating offshore wind farms*, pp. 53–76, Springer, 2016.

[15] S. F. González and V. Diaz-Casas, "Present and future of floating offshore wind," in *Floating offshore wind farms*, pp. 1–22, Springer, 2016.

[16] G. A. D. Amaral, "Analytical assessment of the mooring system stiffness," Master's thesis, Escola Politécnica da Universidade de São Paulo, 2020.

[17] W. Musial, S. Butterfield, and A. Boone, "Feasibility of floating platform systems for wind turbines," in *42nd AIAA aerospace sciences meeting and exhibit*, p. 1007, 2004.

[18] Y. Liu, S. Li, Q. Yi, and D. Chen, "Developments in semi-submersible floating foundations supporting wind turbines: A comprehensive review," *Renewable and Sustainable Energy Reviews*, vol. 60, pp. 433–449, 2016.

[19] A. Crowle and P. Thies, "Challenges during installation of floating wind turbines," 2021.

[20] O. Hill, "A review of the technical challenges faced in floating offshore wind turbine deployment," 2020.

[21] D. Tillenburg, "Technical challenges of floating offshore wind turbines-an overview," 2021.

[22] E. N. Wayman, P. Sclavounos, S. Butterfield, J. Jonkman, and W. Musial, "Coupled dynamic modeling of floating wind turbine systems," in *Offshore technology conference*, OnePetro, 2006.

[23] P. Sclavounos, C. Tracy, and S. Lee, "Floating offshore wind turbines: Responses in a seastate pareto optimal designs and economic assessment," in *International Conference on Offshore Mechanics and Arctic Engineering*, vol. 48234, pp. 31–41, 2008.

[24] D. Matha, "Model development and loads analysis of an offshore wind turbine on a tension leg platform with a comparison to other floating turbine concepts: April 2009," tech. rep., National Renewable Energy Lab.(NREL), Golden, CO (United States), 2010.

[25] A. N. Robertson and J. M. Jonkman, "Loads analysis of several offshore floating wind turbine concepts," in *The twenty-first international offshore and polar engineering conference*, OnePetro, 2011.

[26] K. Iijima, Y. Kuroda, Y. Nihei, and M. Murai, "Comparison of weathervane performance between two types of fowt systems moored to spm," in *International Conference on Offshore Mechanics and Arctic Engineering*, vol. 56543, p. V006T05A010, American Society of Mechanical Engineers, 2015.

[27] B. J. Koo, A. J. Goupee, R. W. Kimball, and K. F. Lambrakos, "Model tests for a floating wind turbine on three different floaters," *Journal of Offshore Mechanics and Arctic Engineering*, vol. 136, no. 2, 2014.

[28] Y. Nihei, K. Iijima, M. Murai, and T. Ikoma, "A comparative study of motion performance of four different fowt designs in combined wind and wave loads," in *International Conference on Offshore Mechanics and Arctic Engineering*, vol. 45493, p. V007T05A025, American Society of Mechanical Engineers, 2014.

[29] A. Robertson, J. Jonkman, M. Masciola, H. Song, A. Goupee, A. Coulling, and C. Luan, "Definition of the semisubmersible floating system for phase II of OC4," tech. rep., National Renewable Energy Lab.(NREL), Golden, CO (United States), 2014.

[30] A. N. Robertson, F. Wendt, J. M. Jonkman, W. Popko, H. Dagher, S. Gueydon, J. Qvist, F. Vittori, J. Azcona, E. Uzunoglu, *et al.*, "OC5 project phase II: validation of global loads of the deepcwind floating semisubmersible wind turbine," *Energy Procedia*, vol. 137, pp. 38–57, 2017.

[31] I. Bayati, S. Gueydon, and M. Belloli, "Study of the effect of water depth on potential flow solution of the OC4 semisubmersible floating offshore wind turbine," *Energy Procedia*, vol. 80, pp. 168–176, 2015.

[32] H. Shin, B. Kim, P. T. Dam, and K. Jung, "Motion of OC4 5MW semi-submersible offshore wind turbine in irregular waves," in *International Conference on Offshore Mechanics and Arctic Engineering*, vol. 55423, p. V008T09A028, American Society of Mechanical Engineers, 2013.

[33] F. Huijs, E.-J. de Ridder, and F. Savenije, "Comparison of model tests and coupled simulations for a semi-submersible floating wind turbine," in *International Conference on Offshore Mechanics and Arctic Engineering*, vol. 45530, p. V09AT09A012, American Society of Mechanical Engineers, 2014.

[34] D. Roddier, C. Cermelli, A. Aubault, and A. Weinstein, "Windfloat: A floating foundation for offshore wind turbines," *Journal of renewable and sustainable energy*, vol. 2, no. 3, p. 033104, 2010.

[35] M. Karimirad and C. Michailides, "V-shaped semisubmersible offshore wind turbine: An alternative concept for offshore wind technology," *Renewable Energy*, vol. 83, pp. 126–143, 2015.

[36] M. Ohta, M. Komatsu, H. Ito, and H. Kumamoto, "Development of a v-shaped semi-submersible floating structure for 7MW offshore wind turbine," in *Proceedings of the International Symposium on Marine and Offshore Renewable Energy, Tokyo, Japan*, pp. 28–30, 2013.

[37] W. Yu, K. Müller, F. Lemmer, H. Bredmose, M. Borg, G. Sanchez, and T. Landbo, "D4. 2 public definition of the two LIFES50+ 10MW floater concepts," 2018.

[38] J. Galvan, M. Sánchez-Lara, I. Mendikoa, G. Pérez-Morán, V. Nava, and R. Rodríguez-Arias, "NAUTILUS-DTU10 MW floating offshore wind turbine at gulf of maine: Public numerical models of an actively ballasted semisubmersible," in *Journal of Physics: Conference Series*, vol. 1102, p. 012015, IOP Publishing, 2018.

[39] C. E. Silva de Souza, P. A. Berthelsen, L. Eliassen, E. E. Bachynski, E. Engebretsen, and H. Haslum, "Definition of the INO WINDMOOR 12 MW base case floating wind turbine," 2021.

[40] M. Borg, M. Walkusch Jensen, S. Urquhart, M. T. Andersen, J. B. Thomsen, and H. Stiesdal, "Technical definition of the tetraspar demonstrator floating wind turbine foundation," *Energies*, vol. 13, no. 18, p. 4911, 2020.

[41] J. O. G. Tande, K. Merz, U. S. Paulsen, and H. G. Svendsen, "Floating offshore turbines," *Wiley Interdisciplinary Reviews: Energy and Environment*, vol. 4, no. 3, pp. 213–228, 2015.

[42] B. Drew, A. R. Plummer, and M. N. Sahinkaya, "A review of wave energy converter technology," 2009.

[43] D. Konispoliatis, T. Mazarakos, T. Soukissian, and S. Mavrakos, "Refos: A multi-purpose floating platform suitable for wind and wave energy exploitation," in *Proceedings of the 11th International Conference on Deregulated Electricity Market Issues in South Eastern Europe (DEMSEE 2018), Nicosia, Cyprus*, pp. 20–21, 2018.

[44] D. N. Konispoliatis, G. M. Katsaounis, D. I. Manolas, T. H. Soukissian, S. Polyzos, T. P. Mazarakos, S. G. Voutsinas, and S. A. Mavrakos, "Refos: A renewable energy multi-purpose floating offshore system," *Energies*, vol. 14, no. 11, p. 3126, 2021.

[45] A. F. Falcão and J. C. Henriques, "Oscillating-water-column wave energy converters and air turbines: A review," *Renewable energy*, vol. 85, pp. 1391–1424, 2016.

[46] M. Karimi, M. Hall, B. Buckham, and C. Crawford, "A multi-objective design optimization approach for floating offshore wind turbine support structures," *Journal of Ocean Engineering and Marine Energy*, vol. 3, no. 1, pp. 69–87, 2017.

[47] A. Martinez and G. Iglesias, "Multi-parameter analysis and mapping of the levelised cost of energy from floating offshore wind in the mediterranean sea," *Energy Conversion and Management*, vol. 243, p. 114416, 2021.

[48] T. H. Soukissian and A. Papadopoulos, "Effects of different wind data sources in offshore wind power assessment," *Renewable Energy*, vol. 77, pp. 101–114, 2015.

[49] I. Young, J. Vinoth, S. Zieger, and A. V. Babanin, "Investigation of trends in extreme value wave height and wind speed," *Journal of Geophysical Research: Oceans*, vol. 117, no. C11, 2012.

[50] E. Vanem, "A regional extreme value analysis of ocean waves in a changing climate," *Ocean Engineering*, vol. 144, pp. 277–295, 2017.

[51] M. Katalinić and J. Parunov, "Comprehensive wind and wave statistics and extreme values for design and analysis of marine structures in the adriatic sea," *Journal of Marine Science and Engineering*, vol. 9, no. 5, p. 522, 2021.

[52] I. Morton and J. Bowers, "Extreme value analysis in a multivariate offshore environment," *Applied Ocean Research*, vol. 18, no. 6, pp. 303–317, 1996.

[53] T. H. Soukissian and C. Tsalis, "The effect of the generalized extreme value distribution parameter estimation methods in extreme wind speed prediction," *Natural Hazards*, vol. 78, no. 3, pp. 1777–1809, 2015.

[54] T. H. Soukissian and C. Tsalis, "Effects of parameter estimation method and sample size in metocean design conditions," *Ocean Engineering*, vol. 169, pp. 19–37, 2018.

[55] A. Devis-Morales, R. Montoya-Sánchez, G. Bernal, and A. Osorio, "Assessment of extreme wind and waves in the colombian caribbean sea for offshore applications," *Applied Ocean Research*, vol. 69, pp. 10–26, 2017.

[56] J. Ferreira and C. Guedes Soares, "An application of the peaks over threshold method to predict extremes of significant wave height," 1998.

[57] S. Caires and A. Sterl, "100-year return value estimates for ocean wind speed and significant wave height from the era-40 data," *Journal of Climate*, vol. 18, no. 7, pp. 1032–1048, 2005.

[58] F. J. Méndez, M. Menéndez, A. Luceño, and I. J. Losada, "Estimation of the long-term variability of extreme significant wave height using a time-dependent peak over threshold (pot) model," *Journal of Geophysical Research: Oceans*, vol. 111, no. C7, 2006.

[59] P. Dissanayake, T. Flock, J. Meier, and P. Sibbertsen, "Modelling short-and long-term dependencies of clustered high-threshold exceedances in significant wave heights," *Mathematics*, vol. 9, no. 2817, 2021.

[60] S. Coles, *An Introduction to Statistical Modeling of Extreme Values*. Bristol, UK: Springer, 2001.

[61] T. Iliopoulou, *Stochastic investigation of hydrological extremes: influence of temporal variability and dependence*. PhD thesis, National Technical University of Athens, 2020.

[62] Y. Li, X. Huang, K. F. Tee, Q. Li, and X.-P. Wu, "Comparative study of onshore and offshore wind characteristics and wind energy potentials: A case study for southeast coastal region of china," *Sustainable Energy Technologies and Assessments*, vol. 39, p. 100711, 2020.

[63] T. Soukissian, A. Papadopoulos, P. Skrimizeas, F. Karathanasi, P. Axaopoulos, E. Avgoustoglou, H. Kyriakidou, C. Tsalis, A. Voudouri, F. Gofa, *et al.*, "Assessment of offshore wind power potential in the aegean and ionian seas based on high-resolution hindcast model results," 2017.

[64] K. Kardakaris, I. Boufidi, and T. Soukissian, "Offshore wind and wave energy complementarity in the greek seas based on ERA5 data," *Atmosphere*, vol. 12, no. 10, p. 1360, 2021.

[65] I. P. Lemos, A. M. G. Lima, and M. A. V. Duarte, "thresholdmodeling: A python package for modeling excesses over a threshold using the peak-over-threshold method and the generalized pareto distribution," *Journal of Open Source Software*, vol. 5, no. 46, p. 2013, 2020.

[66] A. Vamiadakis, "Hydrodynamic analysis of an offshore multi-purpose floating structure and evaluation of the annual wave energy yield at three locations in europe," Master's thesis, National Technical University of Athens, 2018.

[67] J. Falnes and P. McIver, "Surface wave interactions with systems of oscillating bodies and pressure distributions," *Applied Ocean Research*, vol. 7, no. 4, pp. 225–234, 1985.

[68] K. Kokkinowrachos, S. Mavrakos, and S. Asorakos, "Behaviour of vertical bodies of revolution in waves," *Ocean Engineering*, vol. 13, no. 6, pp. 505–538, 1986.

[69] S. Mavrakos and P. Koumoutsakos, "Hydrodynamic interaction among vertical axisymmetric bodies restrained in waves," *Applied Ocean Research*, vol. 9, no. 3, pp. 128–140, 1987.

[70] S. Mavrakos, "Hydrodynamic coefficients for groups of interacting vertical axisymmetric bodies," *Ocean engineering*, vol. 18, no. 5, pp. 485–515, 1991.

[71] D. N. Konispoliatis and S. A. Mavrakos, "Hydrodynamics of multiple vertical axisymmetric OWC´s devices restrained in waves," in *International Conference on Offshore Mechanics and Arctic Engineering*, vol. 55430, p. V009T12A040, American Society of Mechanical Engineers, 2013.

[72] D. N. Konispoliatis and S. A. Mavrakos, "Hydrodynamics and power absorption characteristics of free floating and moored arrays of OWC´s devices," in *Proceedings of the ASME 2014 33rd International Conference on Ocean, Offshore and Arctic Engineering, San Francisco, CA, USA*, pp. 8–13, 2014.

[73] D. Konispoliatis and S. Mavrakos, "Hydrodynamic analysis of an array of interacting free-floating oscillating water column (OWC´s) devices," *Ocean engineering*, vol. 111, pp. 179–197, 2016.

[74] D. Konispoliatis, T. Mazarakos, and S. Mavrakos, "Hydrodynamic analysis of three–unit arrays of floating annular oscillating–water–column wave energy converters," *Applied Ocean Research*, vol. 61, pp. 42–64, 2016.

[75] T. P. Mazarakos, T. D. Tsaousis, S. A. Mavrakos, and I. K. Chatjigeorgiou, "Analytical investigation of tension loads acting on a tlp floating wind turbine," *Journal of Marine Science and Engineering*, vol. 10, no. 3, p. 318, 2022.

[76] T. Mazarakos, D. Konispoliatis, G. Katsaounis, S. Polyzos, D. Manolas, S. Voutsinas, T. Soukissian, and S. A. Mavrakos, "Numerical and experimental studies of a multi-purpose floating tlp structure for combined wind and wave energy exploitation," *Mediterranean Marine Science*, vol. 20, no. 4, pp. 745–763, 2019.

[77] C. Le, Y. Li, and H. Ding, "Study on the coupled dynamic responses of a submerged floating wind turbine under different mooring conditions," *Energies*, vol. 12, no. 3, p. 418, 2019.

[78] E. Huse and K. Matsumoto, "Practical estimation of mooring line damping," in *Offshore Technology Conference*, OnePetro, 1988.

[79] S. Mavrakos and J. Chatjigeorgiou, "Mooring-induced damping on floating structures," 1996.

[80] V. Papazoglou, S. Mavrakos, and M. Triantafyllou, "Non-linear cable response and model testing in water," *Journal of sound and vibration*, vol. 140, no. 1, pp. 103–115, 1990.

[81] D. Qiao and J. Ou, "Mooring line damping estimation for a floating wind turbine," *The Scientific World Journal*, vol. 2014, 2014.

[82] M. Masciola, A. Robertson, J. Jonkman, A. Coulling, and A. Goupee, "Assessment of the importance of mooring dynamics on the global response of the deepcwind floating semisubmersible offshore wind turbine," in *The Twenty-third International Offshore and Polar Engineering Conference*, OnePetro, 2013.

[83] L. Johanning, G. H. Smith, and J. Wolfram, "Measurements of static and dynamic mooring line damping and their importance for floating wec devices," *Ocean engineering*, vol. 34, no. 14-15, pp. 1918–1934, 2007.

[84] J. Davidson and J. V. Ringwood, "Mathematical modelling of mooring systems for wave energy converters—a review," *Energies*, vol. 10, no. 5, p. 666, 2017.

[85] D. N. Konispoliatis, I. K. Chatjigeorgiou, and S. A. Mavrakos, "Hydrodynamics of a moored permeable vertical cylindrical body," *Journal of Marine Science and Engineering*, vol. 10, no. 3, p. 403, 2022.

[86] S. Mavrakos, "Moorings of offshore structures," *MSc course notes (in Greek)*, 2007.

[87] D. Brown, G. Lyons, and H. Ln, "Advances in mooring line damping," *Underwater Technology*, vol. 21, no. 2, pp. 5–11, 1995.

[88] M. Triantafyllou, D. Yue, and D. Tein, "Damping of moored floating structures," in *Offshore Technology Conference*, OnePetro, 1994.

[89] H. Lie, Z. Gao, and T. Moan, "Mooring line damping estimation by a simplified dynamic model," in *International Conference on Offshore Mechanics and Arctic Engineering*, vol. 42673, pp. 197–204, 2007.

[90] "EU project: REFOS, deliverable D1.3: General arrangement of the floating supporting structure with its components and hydrostatic calculations," 2017. Life – Cycle Assessment of a Renewable Energy Multi – Purpose Floating Offshore System.

[91] S. Mavrakos, "User's manual for the software HAMVAB," 1996.

[92] J. M. Jonkman, *Dynamics modeling and loads analysis of an offshore floating wind turbine*. University of Colorado at Boulder, 2007.

[93] S. Christiansen, T. Bak, and T. Knudsen, "Damping wind and wave loads on a floating wind turbine," *Energies*, vol. 6, no. 8, pp. 4097–4116, 2013.

[94] S. Gueydon, "Aerodynamic damping on a semisubmersible floating foundation for wind turbines," *Energy Procedia*, vol. 94, pp. 367–378, 2016.

[95] P. Davies, M. François, F. Grosjean, P. Baron, K. Salomon, and D. Trassoudaine, "Synthetic mooring lines for depths to 3000 meters," in *Offshore Technology Conference*, OnePetro, 2002.

[96] H.-D. Pham, P. Cartraud, F. Schoefs, T. Soulard, and C. Berhault, "Dynamic modeling of nylon mooring lines for a floating wind turbine," *Applied Ocean Research*, vol. 87, pp. 1–8, 2019.

[97] J. Yan, D. Qiao, B. Li, B. Wang, H. Liang, D. Ning, and J. Ou, "An improved method of mooring damping estimation considering mooring line segments contribution," *Ocean Engineering*, vol. 239, p. 109887, 2021.

[98] M. J. Harrold, P. R. Thies, L. Johanning, D. Newsam, M. Checkley, and C. Bittencourt Ferreira, "Dynamic load reduction and station keeping mooring system for floating offshore wind," in *International Conference on Offshore Mechanics and Arctic Engineering*, vol. 51975, p. V001T01A018, American Society of Mechanical Engineers, 2018.

[99] S. Xu, C. Ji, and C. G. Soares, "Experimental study on taut and hybrid moorings damping and their relation with system dynamics," *Ocean Engineering*, vol. 154, pp. 322–340, 2018.

[100] C. P. Pesce, G. A. Amaral, and G. R. Franzini, "Mooring system stiffness: A general analytical formulation with an application to floating offshore wind turbines," in *International Conference on Offshore Mechanics and Arctic Engineering*, vol. 51975, p. V001T01A021, American Society of Mechanical Engineers, 2018.

[101] R. Balzola, "Mooring line damping in very large water depths," Master's thesis, Massachusetts Institute of Technology, 1999.

[102] D. Evans, "The oscillating water column wave-energy device," *IMA Journal of Applied Mathematics*, vol. 22, no. 4, pp. 423–433, 1978.

[103] D. Konispoliatis, A. Mavrakos, and S. Mavrakos, "Efficiency of an oscillating water column device for several mooring systems," in *Developments in Renewable Energies Offshore*, pp. 666–673, CRC Press, 2020.

[104] DNV-GL, "Wave loads: Class guideline DNVGL-CG-0130," 2018.

# Appendix A

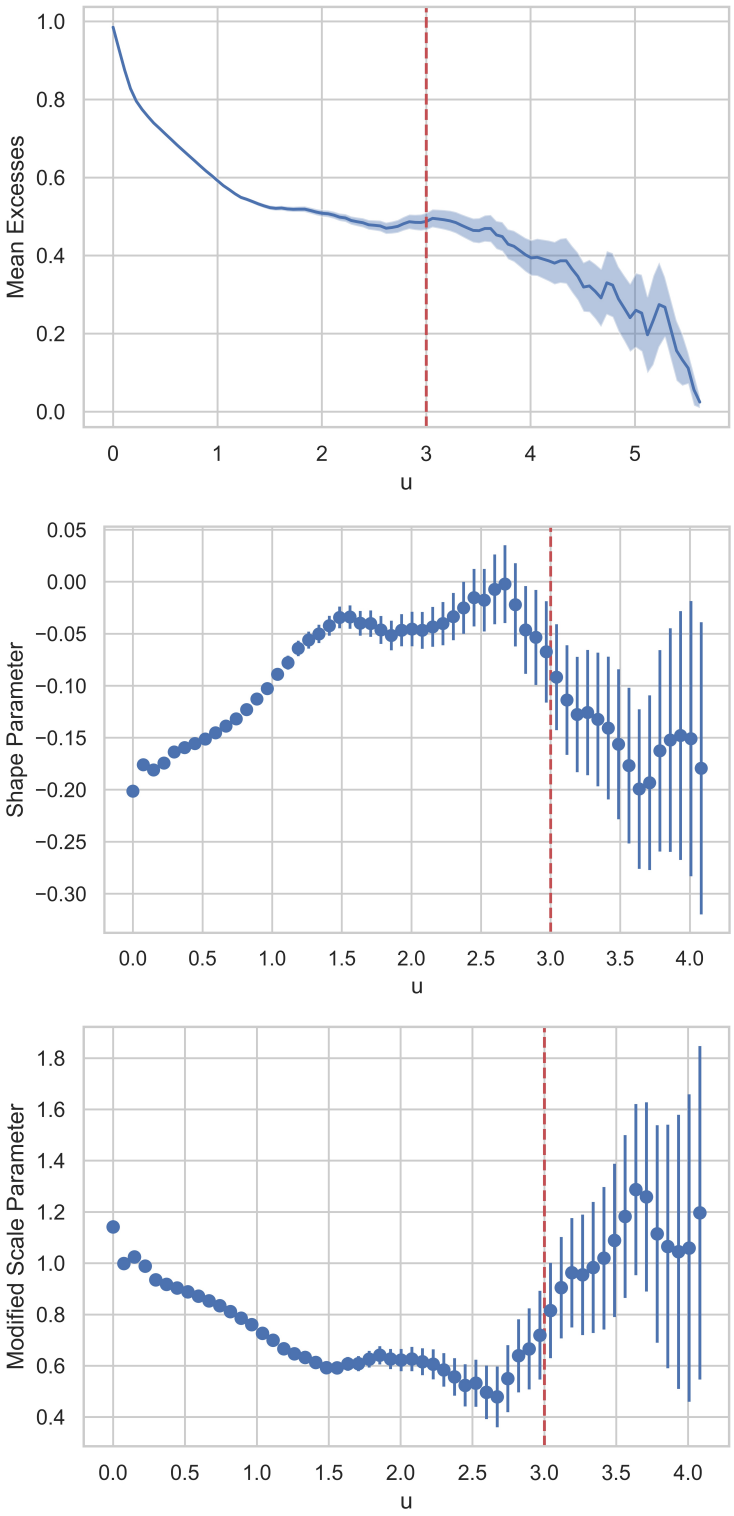


Figure A.1: MRL plot with confidence bands (top), shape stability plot (middle) and modified scale stability plot (bottom) with errorbars of $H_s$ (m) for L1. Red line depicts the threshold selection.

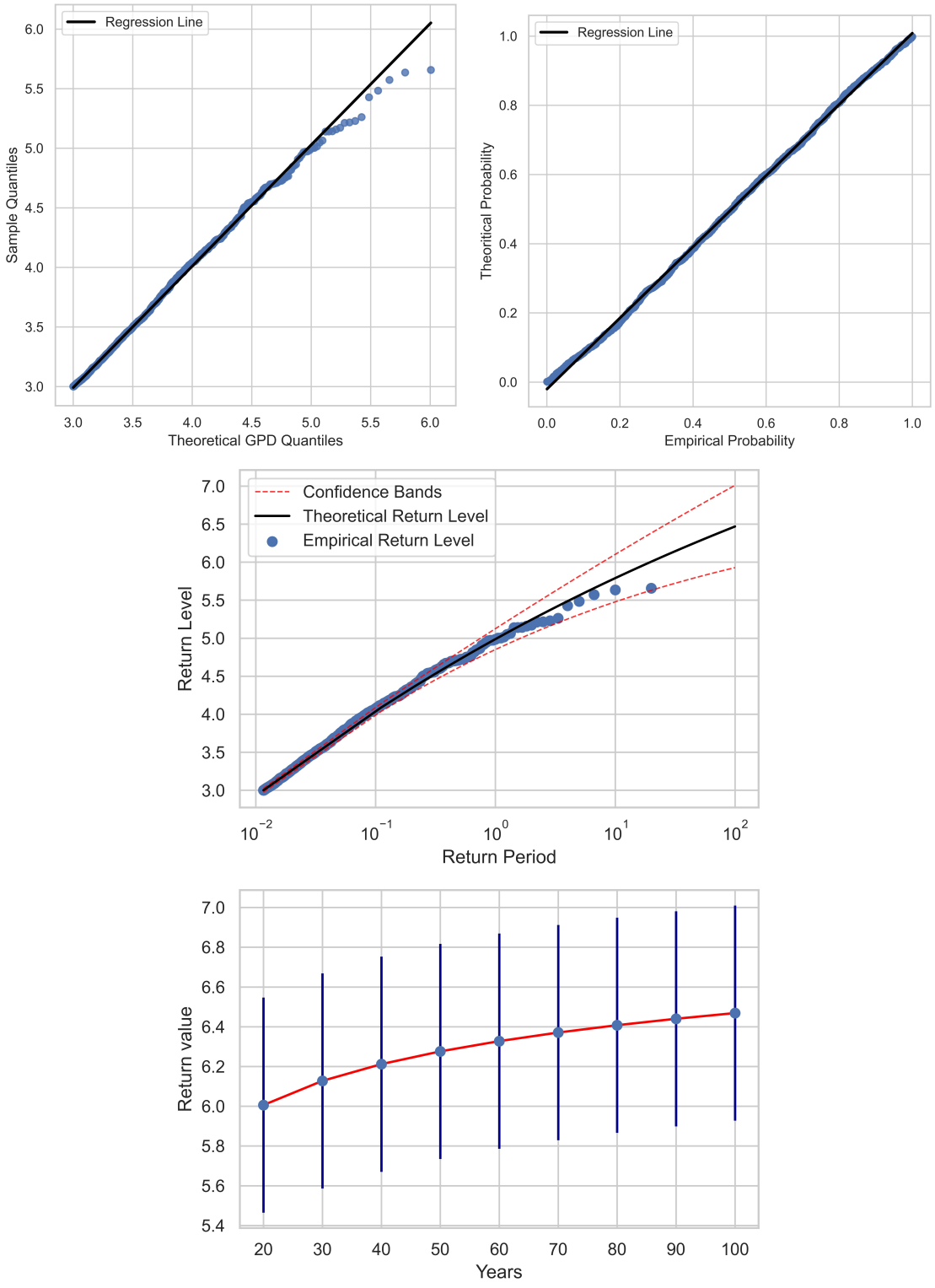


Figure A.2: QQ plot (top left), PP plot (top right), return level plot with confidence bands (middle) and return values curve with errorbars (bottom) of $H_s$ (m) for L1.

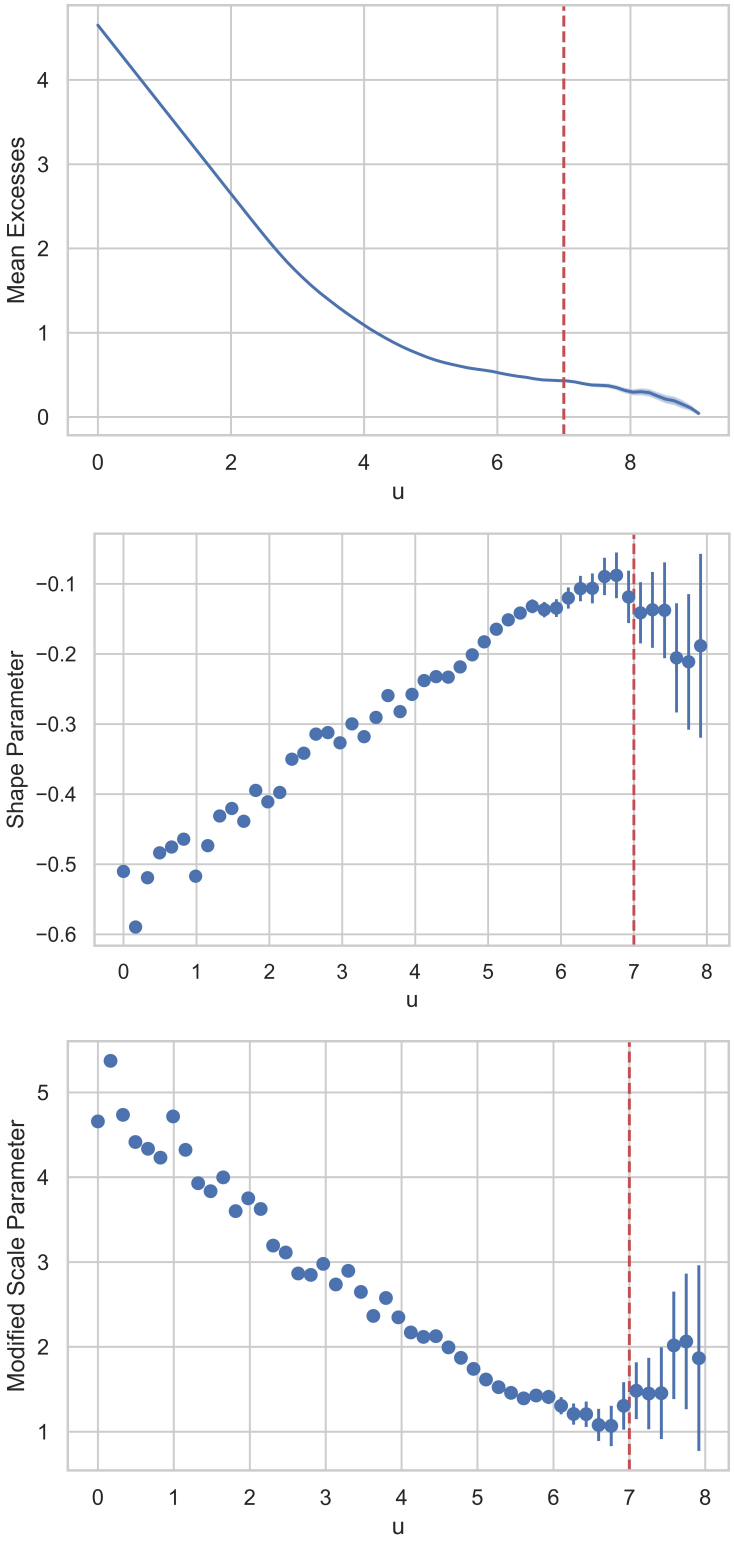


Figure A.3: MRL plot with confidence bands (top), shape stability plot (middle) and modified scale stability plot (bottom) with errorbars of $T_p$ (m) for L1. Red line depicts the threshold selection.

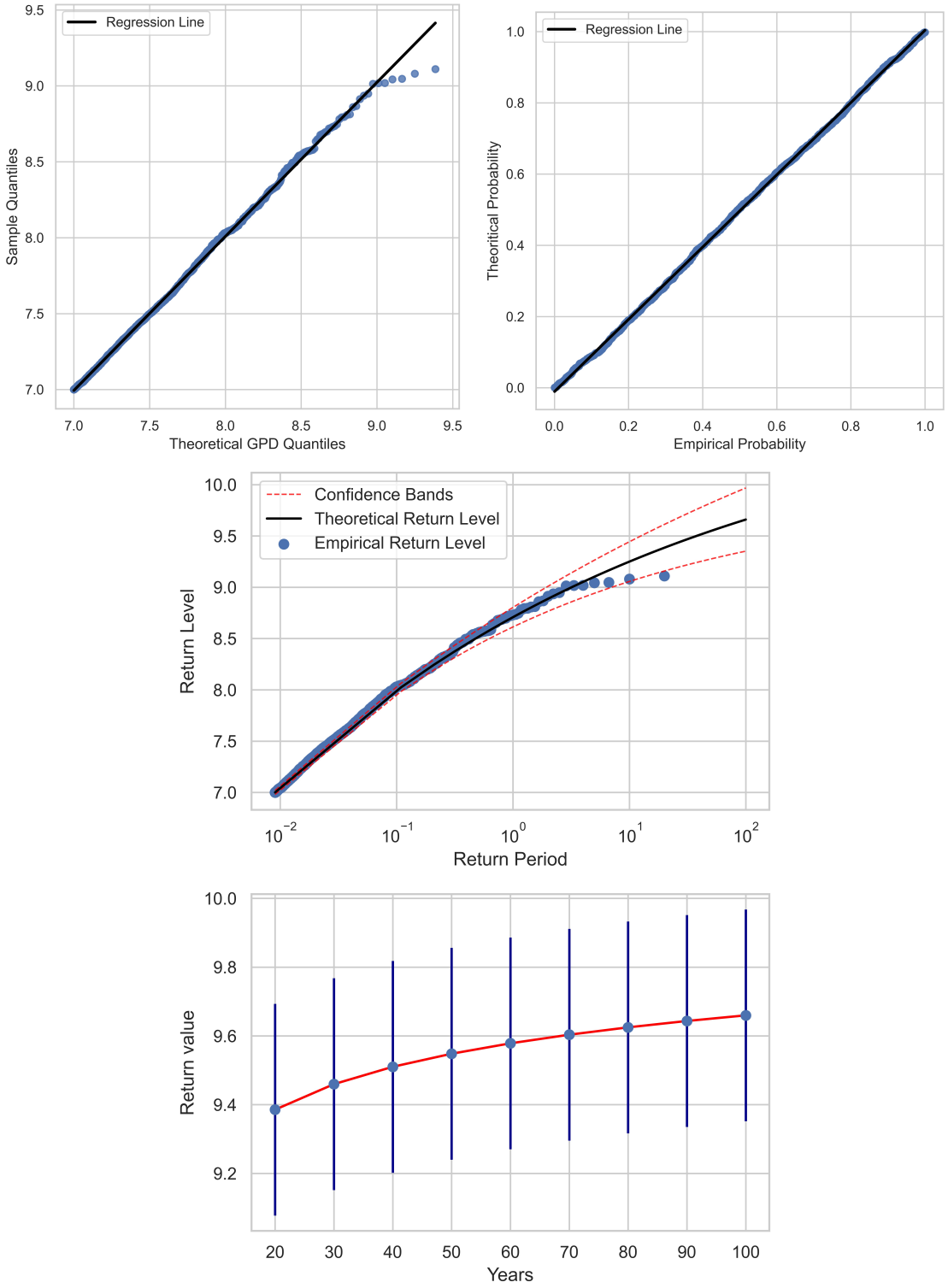


Figure A.4: QQ plot (top left), PP plot (top right), return level plot with confidence bands (middle) and return values curve with errorbars (bottom) of $T_p$ (m) for L1.

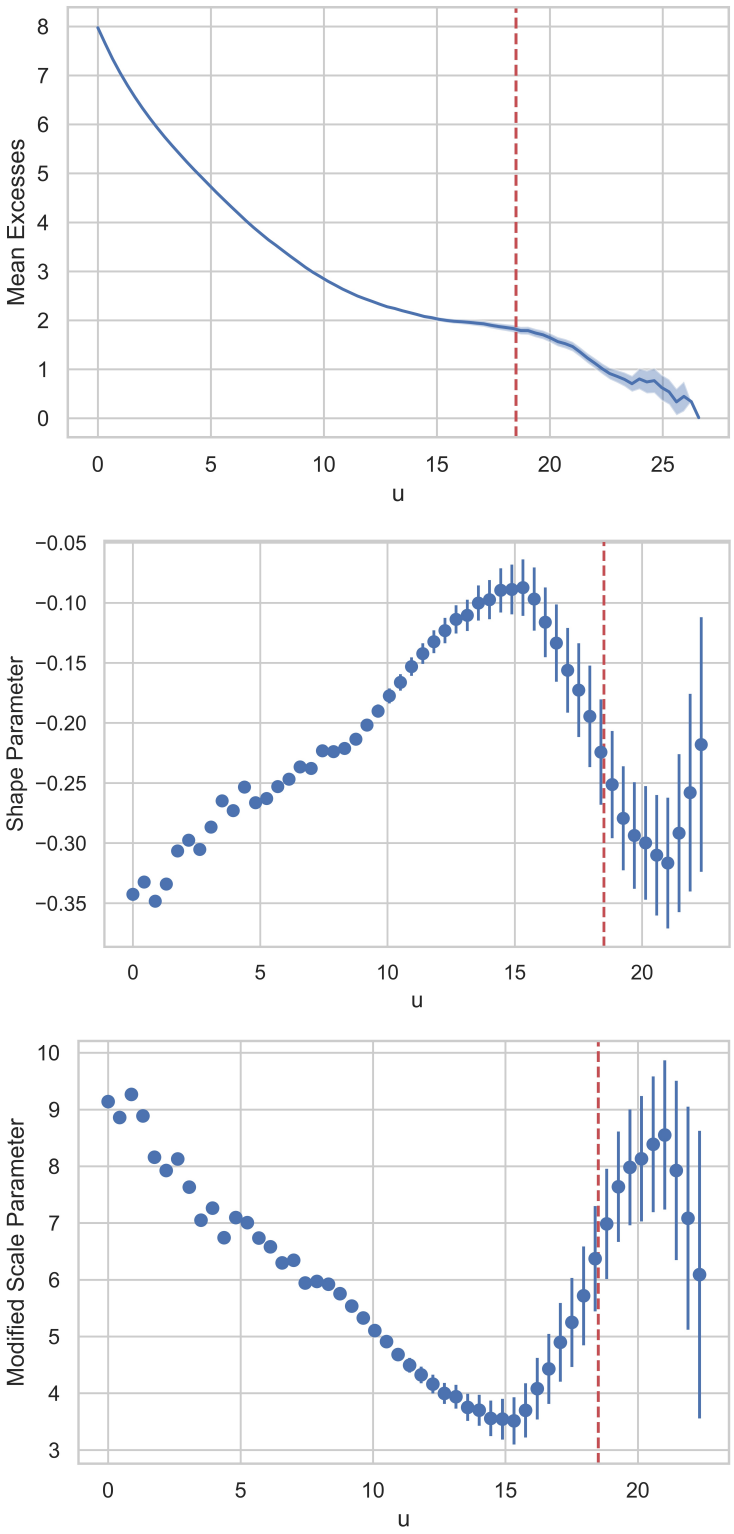


Figure A.5: MRL plot with confidence bands (top), shape stability plot (middle) and modified scale stability plot (bottom) with errorbars of $U_w$ (m) for L2. Red line depicts the threshold selection.

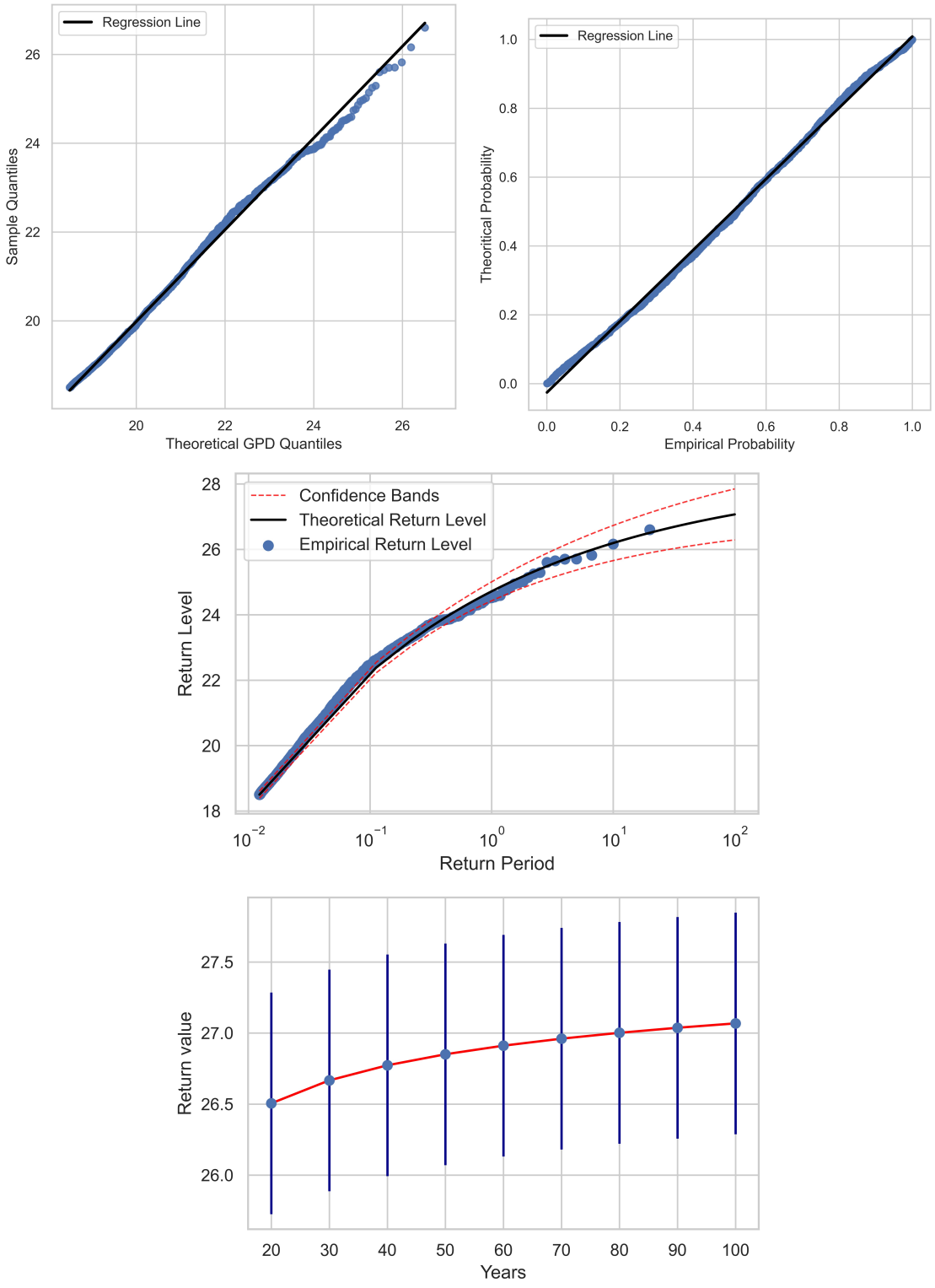


Figure A.6: QQ plot (top left), PP plot (top right), return level plot with confidence bands (middle) and return values curve with errorbars (bottom) of $U_w$ (m) for L2.

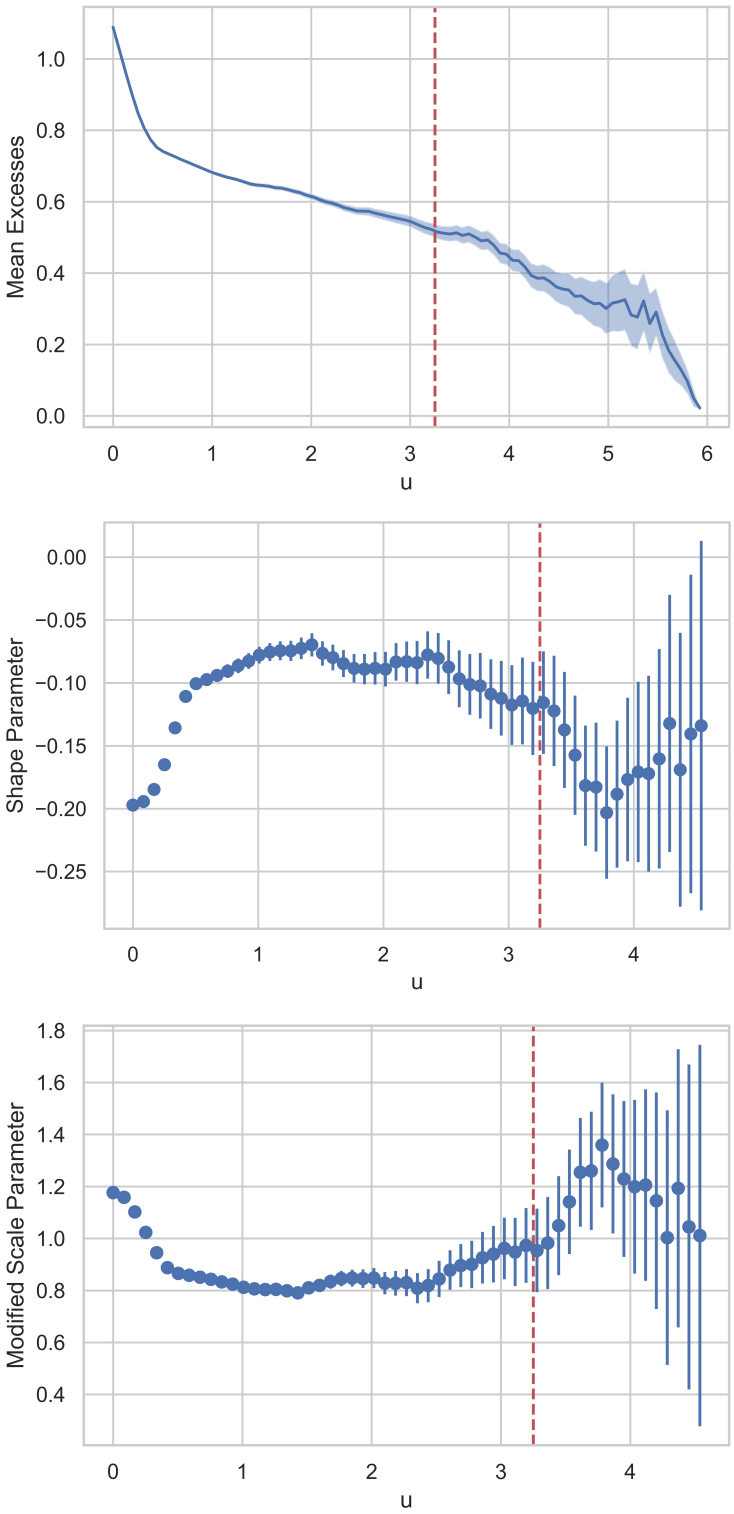


Figure A.7: MRL plot with confidence bands (top), shape stability plot (middle) and modified scale stability plot (bottom) with errorbars of $H_s$ (m) for L2. Red line depicts the threshold selection.

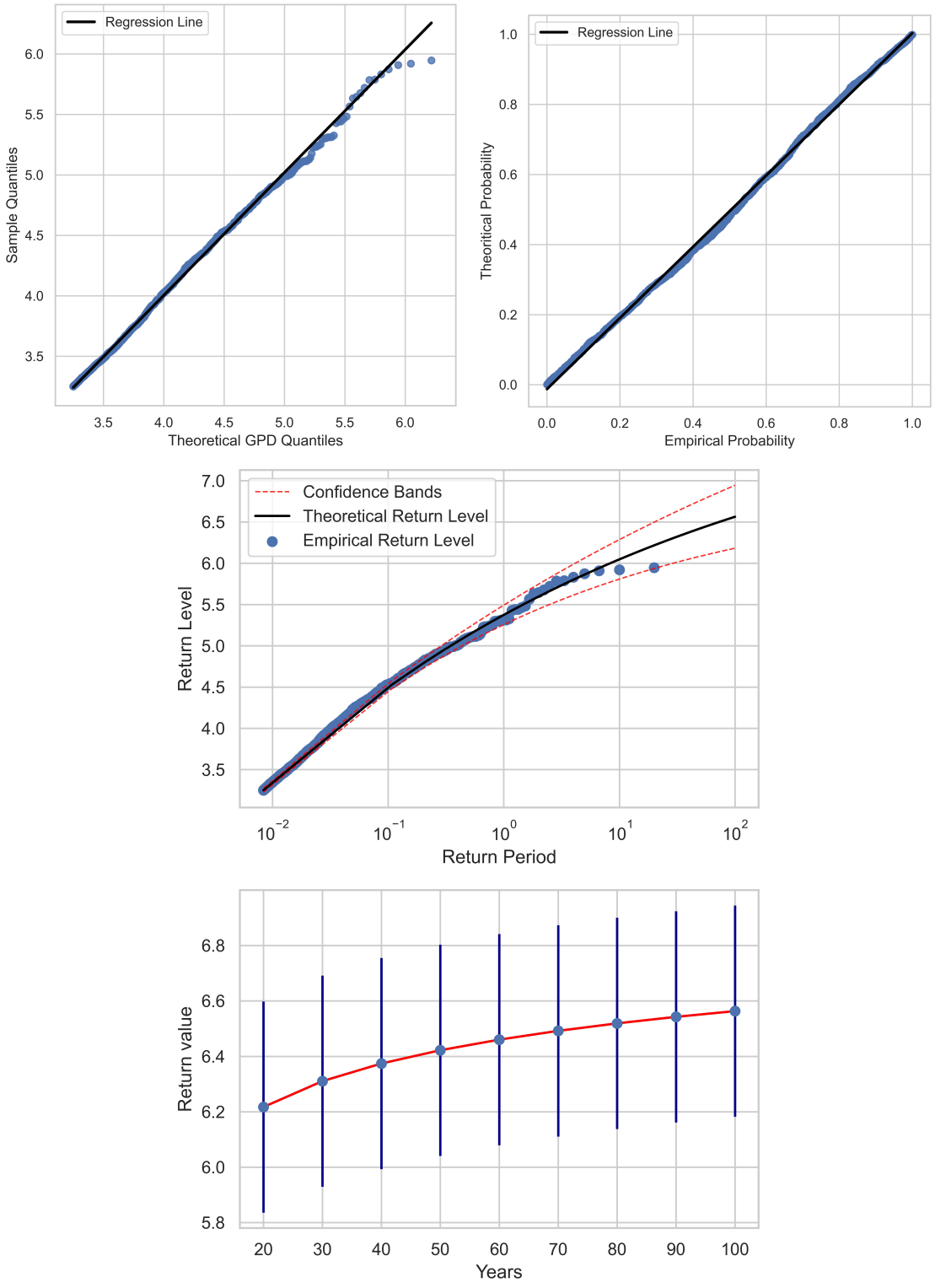


Figure A.8: QQ plot (top left), PP plot (top right), return level plot with confidence bands (middle) and return values curve with errorbars (bottom) of $H_s$ (m) for L2.

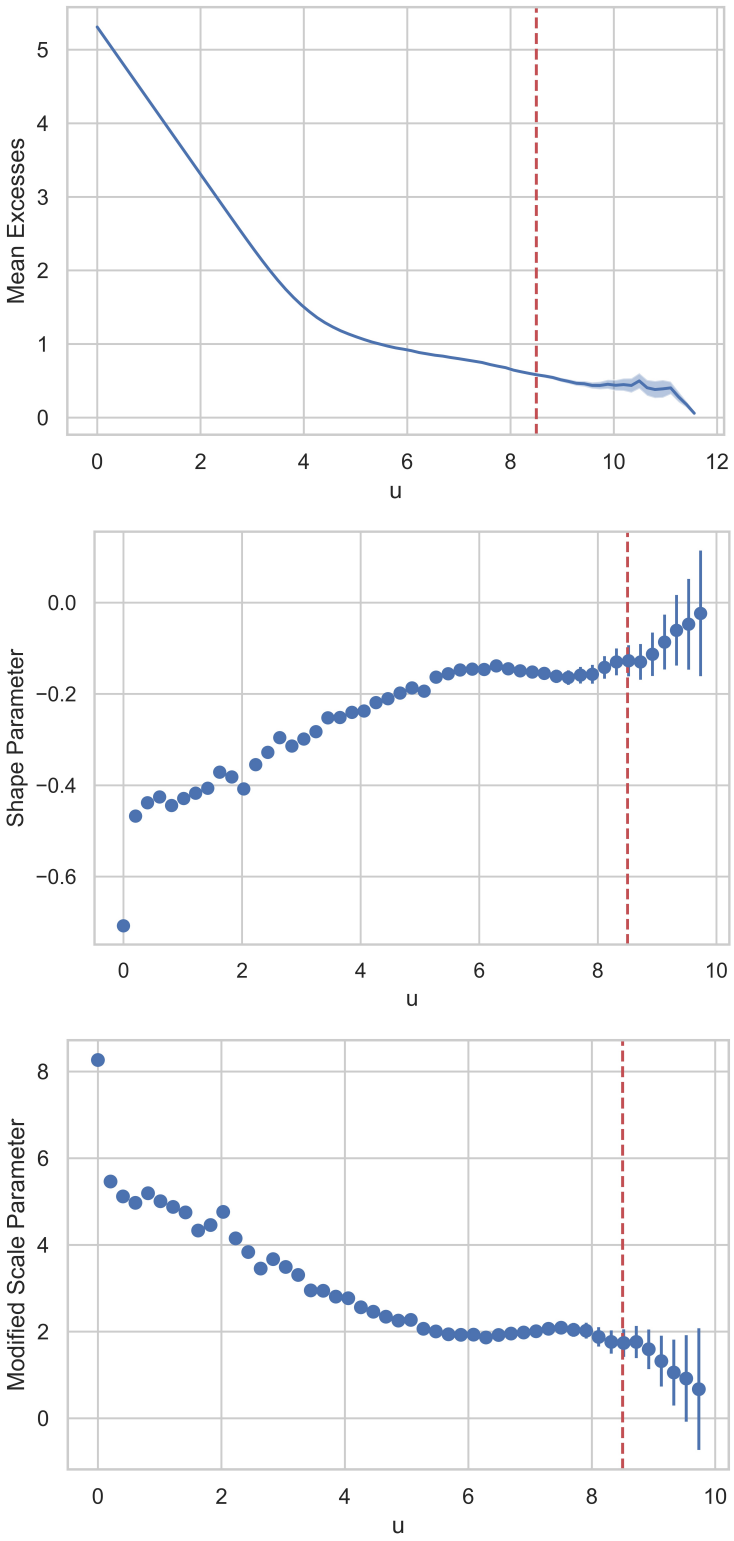


Figure A.9: MRL plot with confidence bands (top), shape stability plot (middle) and modified scale stability plot (bottom) with errorbars of $T_p$ (m) for L2. Red line depicts the threshold selection.

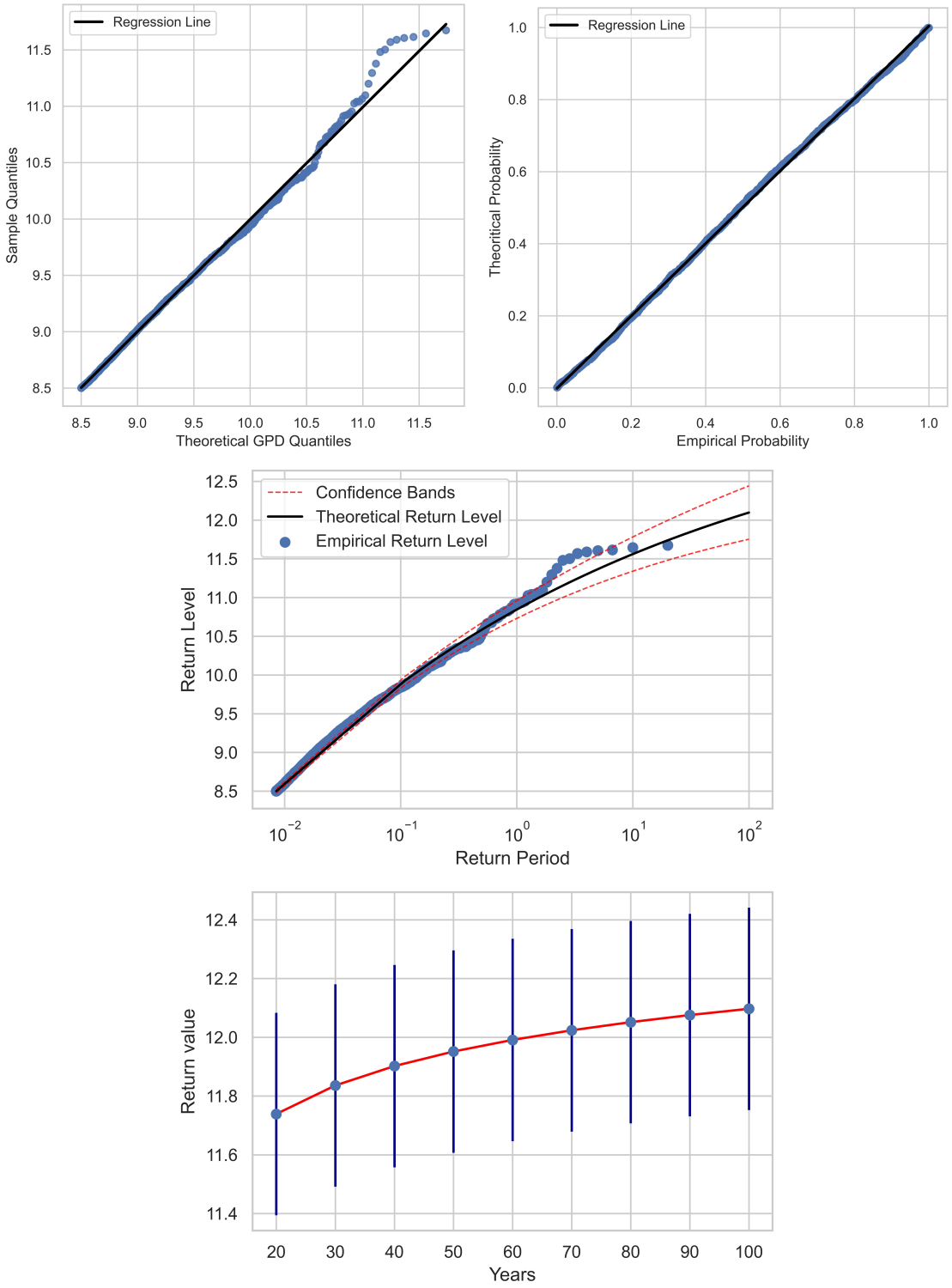


Figure A.10: QQ plot (top left), PP plot (top right), return level plot with confidence bands (middle) and return values curve with errorbars (bottom) of $T_p$ (m) for L2.

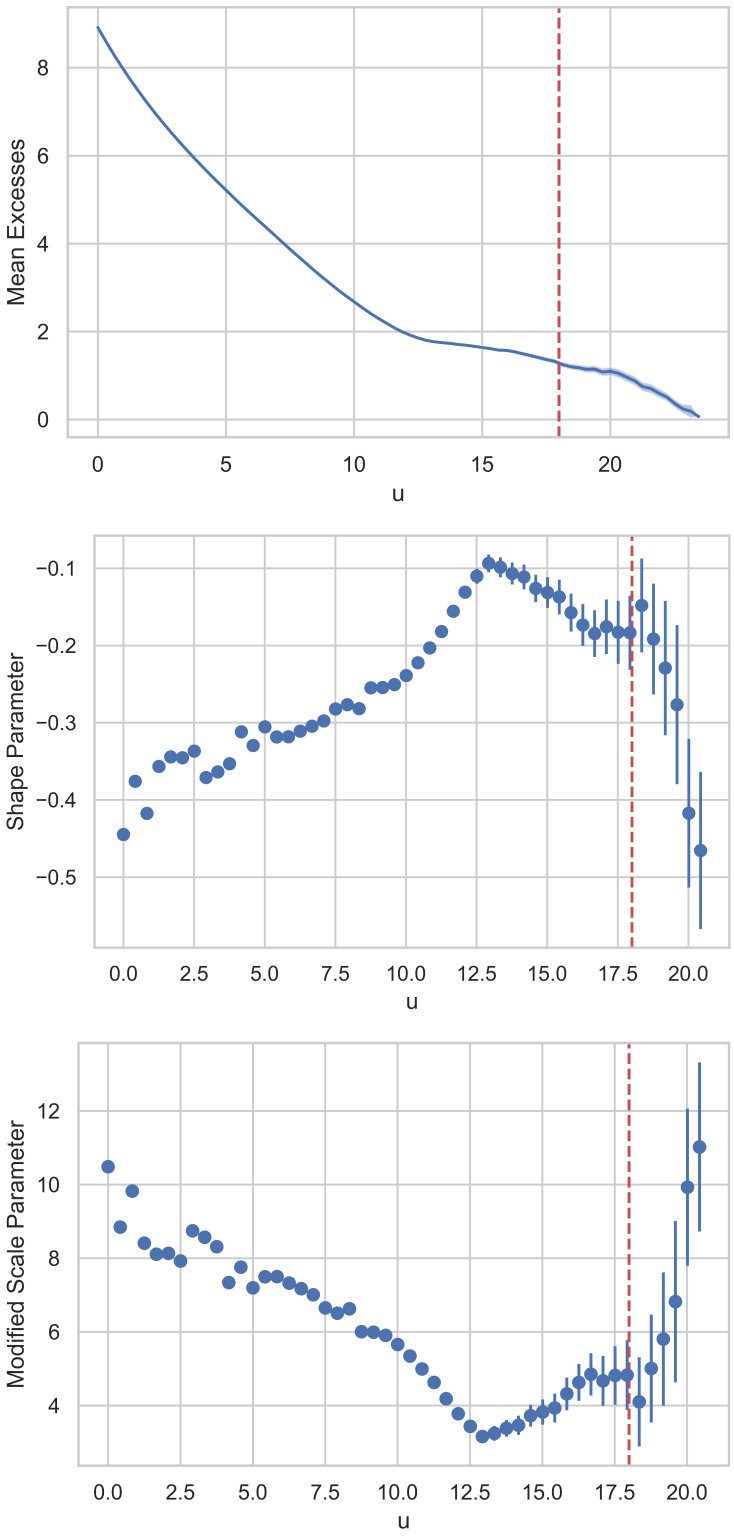


Figure A.11: MRL plot with confidence bands (top), shape stability plot (middle) and modified scale stability plot (bottom) with errorbars of $U_w$ (m) for L3. Red line depicts the threshold selection.

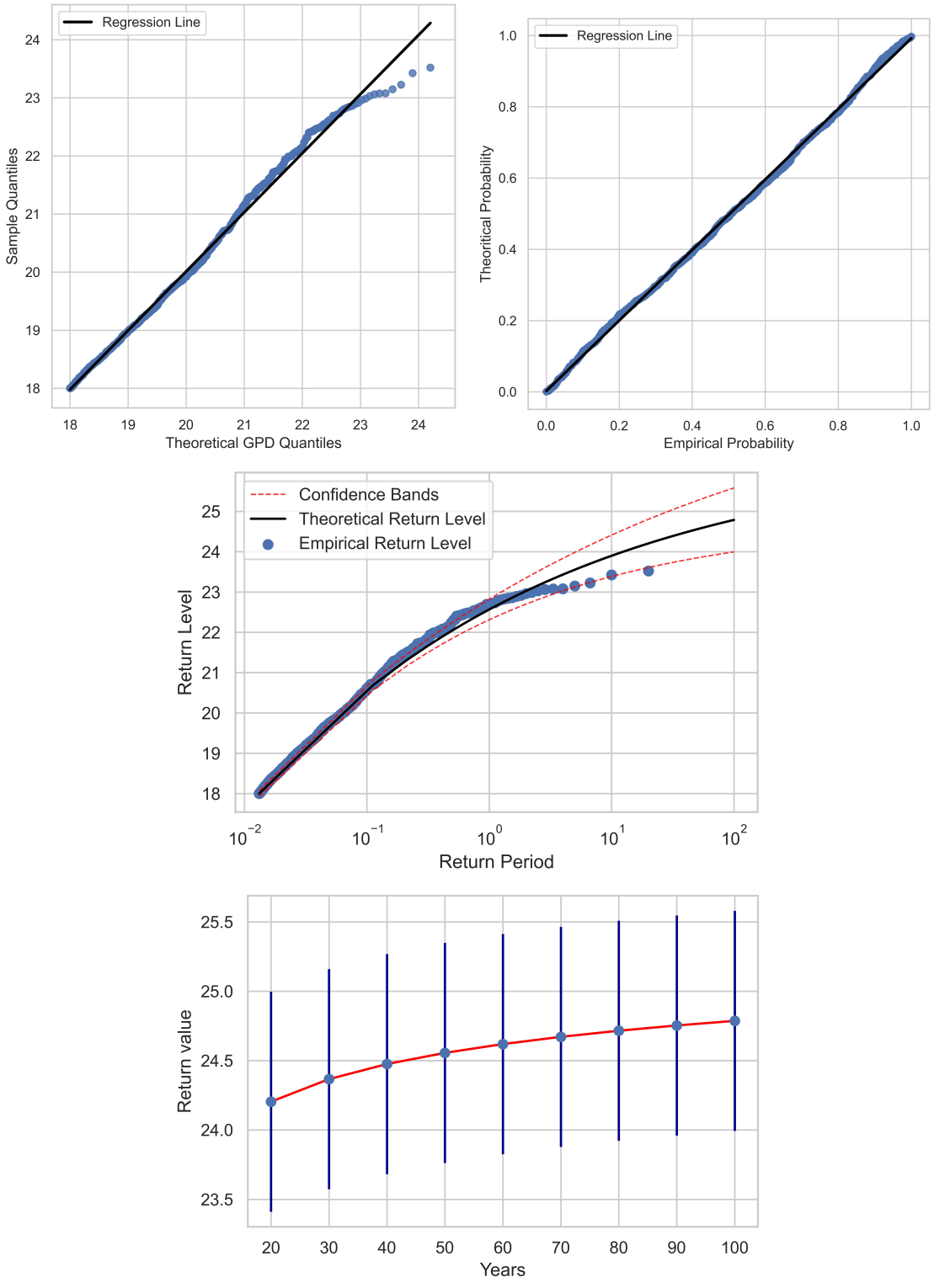


Figure A.12: QQ plot (top left), PP plot (top right), return level plot with confidence bands (middle) and return values curve with errorbars (bottom) of $U_w$ (m) for L3.

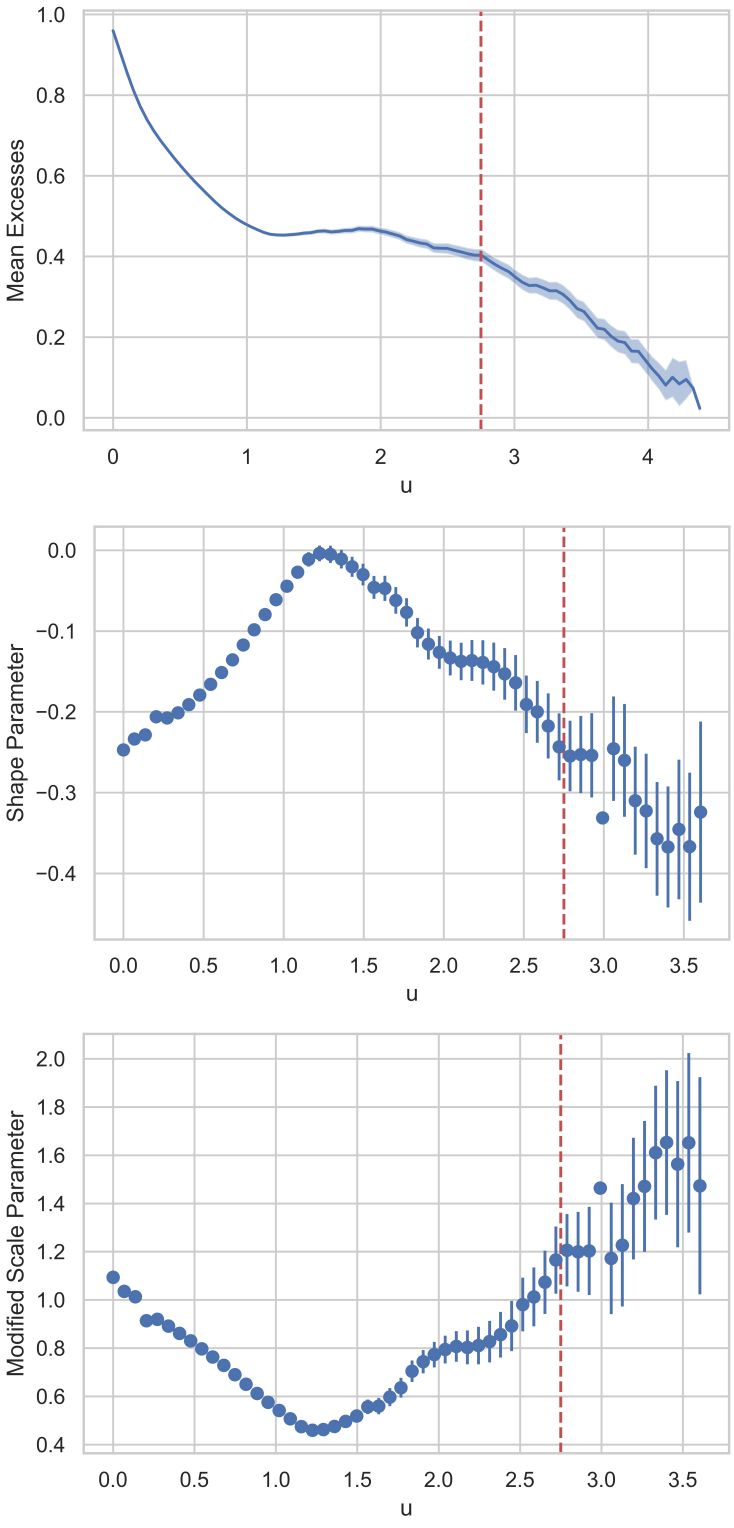


Figure A.13: MRL plot with confidence bands (top), shape stability plot (middle) and modified scale stability plot (bottom) with errorbars of $H_s$ (m) for L3. Red line depicts the threshold selection.

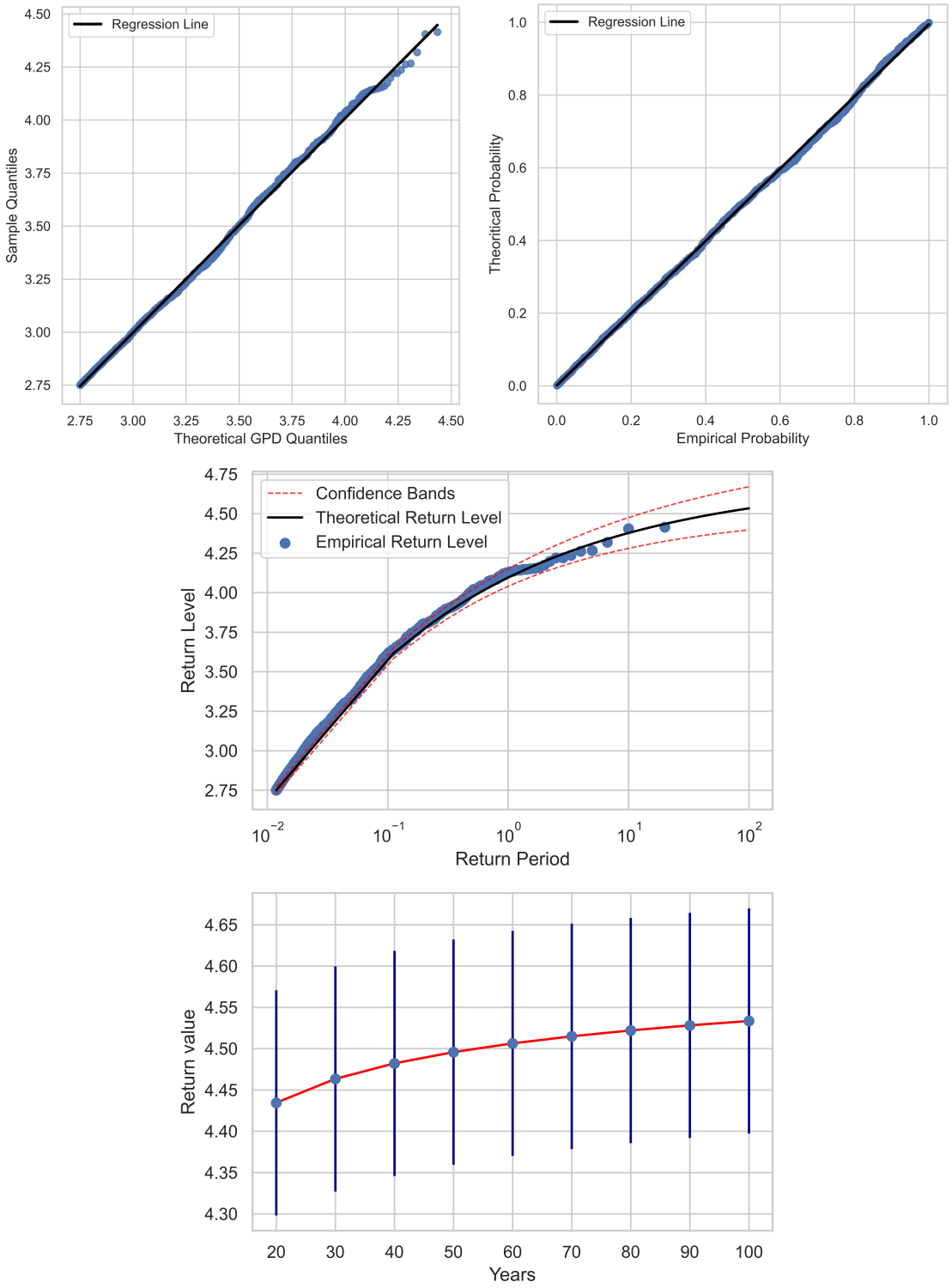


Figure A.14: QQ plot (top left), PP plot (top right), return level plot with confidence bands (middle) and return values curve with errorbars (bottom) of $H_s$ (m) for L3.

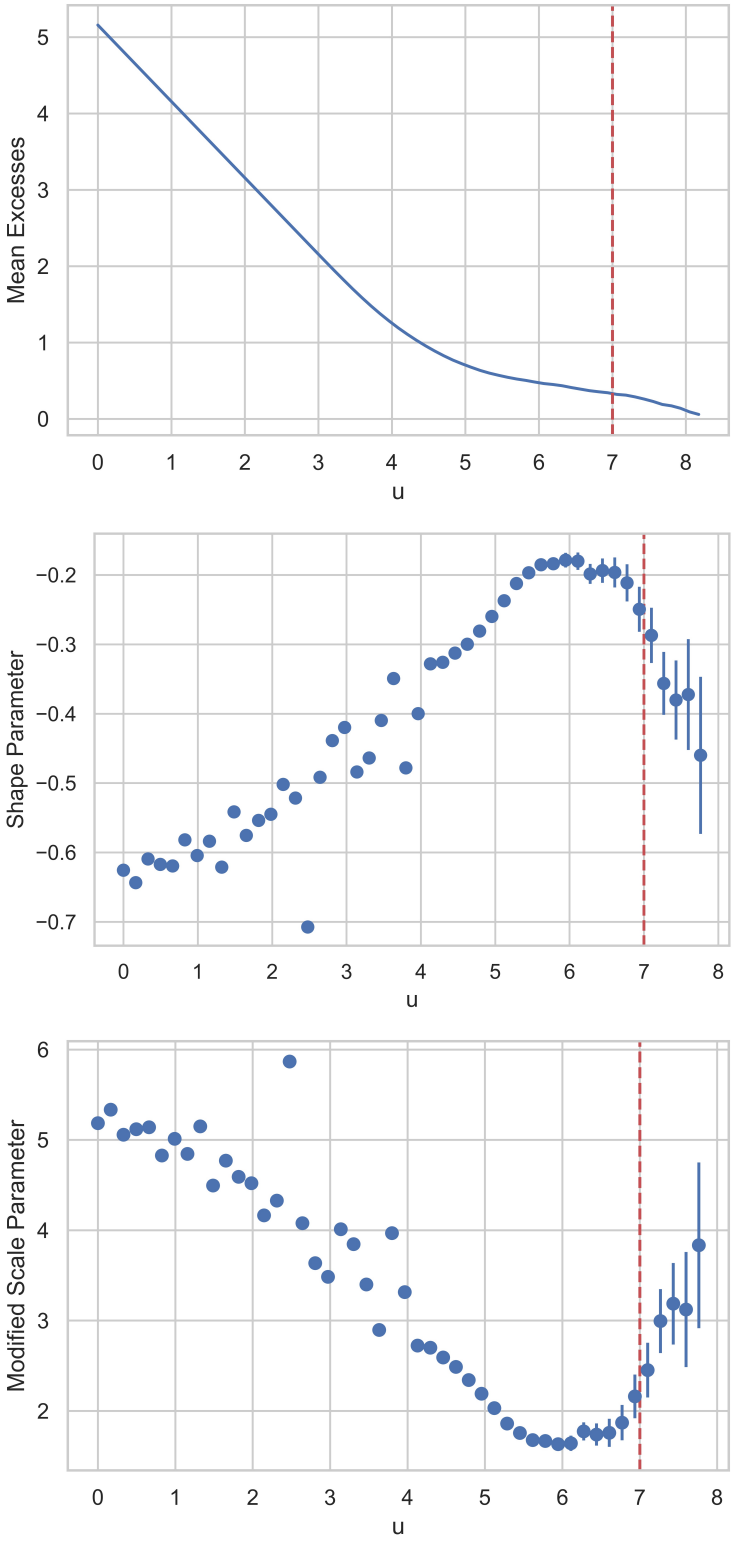


Figure A.15: MRL plot with confidence bands (top), shape stability plot (middle) and modified scale stability plot (bottom) with errorbars of $T_p$ (m) for L3. Red line depicts the threshold selection.

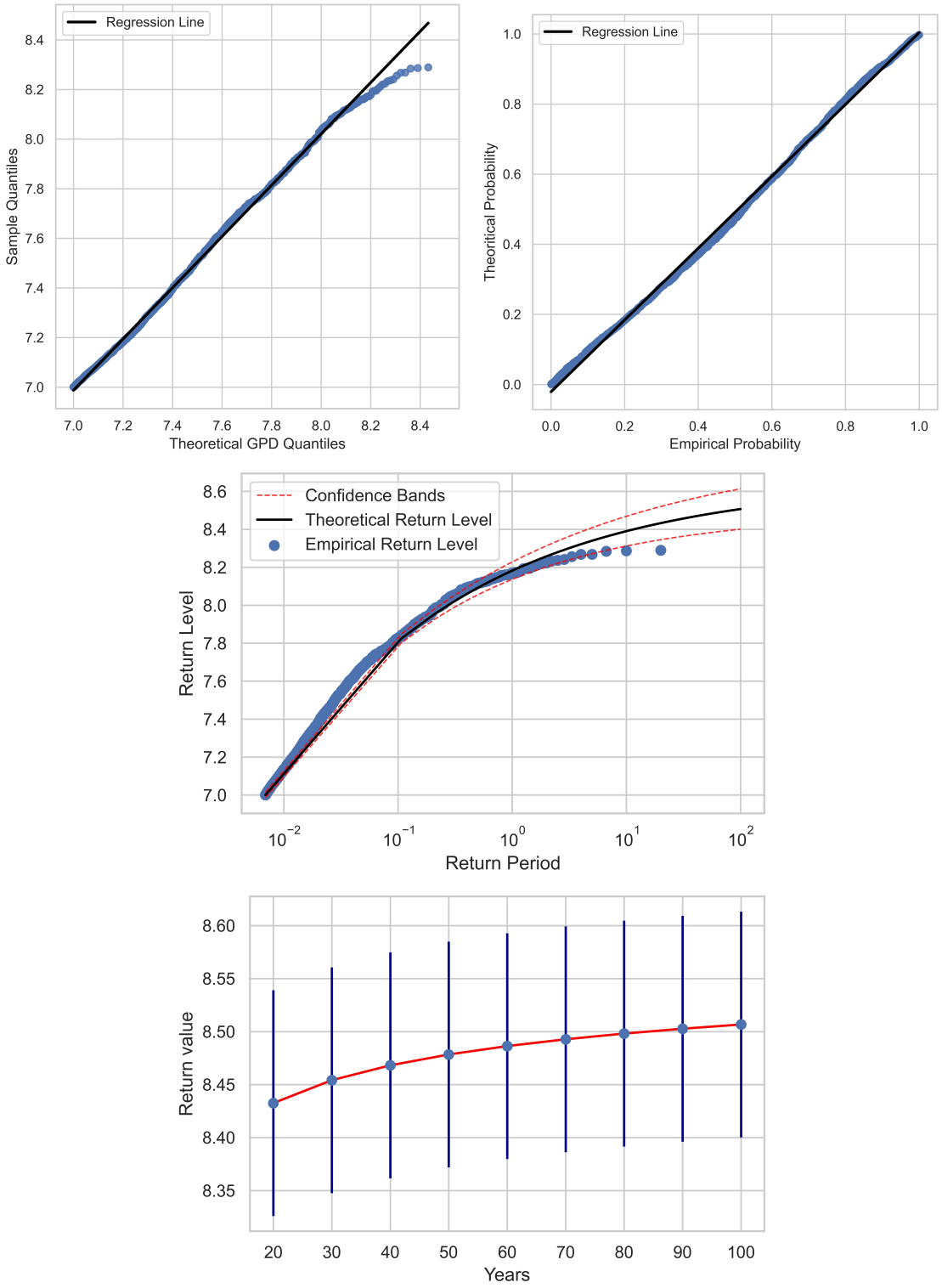


Figure A.16: QQ plot (top left), PP plot (top right), return level plot with confidence bands (middle) and return values curve with errorbars (bottom) of $T_p$ (m) for L3.

# Appendix B

*Python code script for maps.*

```
from mpl_toolkits.basemap import Basemap
import matplotlib.pyplot as plt
import numpy as np
import matplotlib.colors as colors

ca = np.loadtxt('coords_atmos.txt')
cw = np.loadtxt('coords_waves.txt')
#cc = np.loadtxt('coordsCop.txt')

loc=[[37.220,35.964,35.378],
     [26.115,23.160,27.038]]

latmin=np.nanmin(cw[0][:]) -0.5; latmax=np.nanmax(cw[0][:]) +0.5;
lonmin=np.nanmin(cw[1][:]) -0.5; lonmax=np.nanmax(cw[1][:]) +1.5;

idd=[281,280,300,299,169,188,170,189,322,323,341,342];

fig=plt.figure(figsize=(12, 8),frameon=False)
m = Basemap(llcrnrlon=lonmin,llcrnrlat=latmin,urcrnrlon=lonmax,urcrnrlat
    =latmax, epsg=2100)
m.arcgisimage(service='World_Imagery', xpixels = 2000)
for ii in range(len(idd)):
    m.scatter(cw[1][idd[ii]],cw[0][idd[ii]],latlon=True,s=10,c='white')
m.scatter(loc[1][:],loc[0][:],latlon=True, s=18, c='red')
m.drawparallels(np.arange(latmin,latmax,0.5),labels=[1,0,0,0], fontsize
    =10)
meridians=m.drawmeridians(np.arange(lonmin,lonmax,0.5),labels=[0,0,0,1],
     fontsize=10)
for mm in meridians:
    try:
        meridians[mm][1][0].set_rotation(45)
    except:
        pass
plt.savefig('WaveGridLocsInterpolation.jpg', bbox_inches='tight',dpi
    =800)

idd2=[1060,1097,1061,1098,658,621,659,622,1215,1216,1252,1253];

fig=plt.figure(figsize=(12, 8),frameon=False)
m = Basemap(llcrnrlon=lonmin,llcrnrlat=latmin,urcrnrlon=lonmax,urcrnrlat
    =latmax, epsg=2100)
```

```
37 m.arcgisimage(service='World_Imagery', xpixels = 2000)
38 for ii in range(len(idd2)):
39     m.scatter(ca[1][idd2[ii]],ca[0][idd2[ii]],latlon=True,s=10,c='white'
       )
40 m.scatter(loc[1][:],loc[0][:],latlon=True, s=18, c='red')
41 m.drawparallels(np.arange(latmin,latmax,0.5),labels=[1,0,0,0], fontsize
   =10)
42 meridians=m.drawmeridians(np.arange(lonmin,lonmax,0.5),labels=[0,0,0,1],
    fontsize=10)
43 for mm in meridians:
44     try:
45         meridians[mm][1][0].set_rotation(45)
46     except:
47         pass
48 plt.savefig('WindGridLocsInterpolation.jpg', bbox_inches='tight',dpi
   =800)
49
50 fig=plt.figure(figsize=(12, 8),frameon=False)
51 m = Basemap(llcrnrlon=lonmin,llcrnrlat=latmin,urcrnrlon=lonmax,urcrnrlat
   =latmax, epsg=2100)
52 m.arcgisimage(service='World_Imagery', xpixels = 2000)
53 for i in range(25):
54     for j in range(25):
55         m.scatter(cc[1][j],cc[0][i],latlon=True,s=5,c='white')
56 m.scatter(loc[1][:],loc[0][:],latlon=True, s=10, c='red')
57 m.drawparallels(np.arange(latmin,latmax,0.5),labels=[1,0,0,0], fontsize
   =10)
58 meridians=m.drawmeridians(np.arange(lonmin,lonmax,0.5),labels=[0,0,0,1],
    fontsize=10)
59 for mm in meridians:
60     try:
61         meridians[mm][1][0].set_rotation(45)
62     except:
63         pass
64 plt.savefig('Copern.jpg', bbox_inches='tight',dpi=800)
```

*Matlab code script for spatial interpolation and linear regression.*

```
clc;
% ERA5 data read
wsp=dlmread('era5_wind_speed_100m_2d');
swh=dlmread('era5_swh_2d');
mwp=dlmread('era5_mwp_2d');
ca=dlmread('coords_atmos'); cw=dlmread('coords_waves');

%%
% ERA5 data
clc; clearvars -except ca cw wsp swh mwp

ellipsoid = [6378.1 , 0.00335];

locs = [37.220,35.964,35.378;
          26.115,23.160,27.038];

L1id=[1061,1098,1062,1099;
         282,281,301,300];

L2id=[659,622,660,623;
         170,189,171,190];

L3id=[1216,1217,1253,1254;
         323,324,342,343];

% Wind Speed
dist1=[]; dist2=[]; dist3=[];
for i=1:4
    dist1 = [dist1; distance(locs(1,1),locs(2,1),ca(1,L1id(1,i)),ca(2,
        L1id(1,i)),ellipsoid)];
    dist2 = [dist2; distance(locs(1,2),locs(2,2),ca(1,L2id(1,i)),ca(2,
        L2id(1,i)),ellipsoid)];
    dist3 = [dist3; distance(locs(1,3),locs(2,3),ca(1,L3id(1,i)),ca(2,
        L3id(1,i)),ellipsoid)];
end
d1=dist1'; d2=dist2'; d3=dist3';

sp1=[wsp(:,L1id(1,1)),wsp(:,L1id(1,2)),wsp(:,L1id(1,3)),wsp(:,
    L1id(1,4))];
sp2=[wsp(:,L2id(1,1)),wsp(:,L2id(1,2)),wsp(:,L2id(1,3)),wsp(:,
    L2id(1,4))];
```

```
37 sp3=[wsp( : ,L3id(1,1)),wsp( : ,L3id(1,2)),wsp( : ,L3id(1,3)),wsp( : ,
       L3id(1,4))];
38
39 S=sp1./(d1.^2); S=sum(S,2); S0=sum(1./(d1.^2));
40 wspL1=S./S0; dlmwrite('wspL1era5.txt',wspL1);
41
42 S=sp2./(d2.^2); S=sum(S,2); S0=sum(1./(d2.^2));
43 wspL2=S./S0; dlmwrite('wspL2era5.txt',wspL2);
44
45 S=sp3./(d3.^2); S=sum(S,2); S0=sum(1./(d3.^2));
46 wspL3=S./S0; dlmwrite('wspL3era5.txt',wspL3);
47
48 % WAVES
49 dist11=[]; dist22=[]; dist33=[];
50 for i=1:4
51     dist11 = [dist11; distance(locs(1,1),locs(2,1),cw(1,L1id(2,i)),cw(2,
           L1id(2,i)),ellipsoid)];
52     dist22 = [dist22; distance(locs(1,2),locs(2,2),cw(1,L2id(2,i)),cw(2,
           L2id(2,i)),ellipsoid)];
53     dist33 = [dist33; distance(locs(1,3),locs(2,3),cw(1,L3id(2,i)),cw(2,
           L3id(2,i)),ellipsoid)];
54 end
55 d11=dist11'; d22=dist22'; d33=dist33';
56
57 % Significant Wave Height
58 wh1=[swh( : ,L1id(2,1)),swh( : ,L1id(2,2)),swh( : ,L1id(2,3)),swh( : ,
       L1id(2,4))];
59 wh2=[swh( : ,L2id(2,1)),swh( : ,L2id(2,2)),swh( : ,L2id(2,3)),swh( : ,
       L2id(2,4))];
60 wh3=[swh( : ,L3id(2,1)),swh( : ,L3id(2,2)),swh( : ,L3id(2,3)),swh( : ,
       L3id(2,4))];
61
62 S=wh1./(d11.^2); S=sum(S,2); S0=sum(1./(d11.^2));
63 swhL1=S./S0; dlmwrite('swhL1era5.txt',swhL1);
64
65 S=wh2./(d22.^2); S=sum(S,2); S0=sum(1./(d22.^2));
66 swhL2=S./S0; dlmwrite('swhL2era5.txt',swhL2);
67
68 S=wh3./(d33.^2); S=sum(S,2); S0=sum(1./(d33.^2));
69 swhL3=S./S0; dlmwrite('swhL3era5.txt',swhL3);
70
71 % Peak Wave Period
72 wp1=[mwp( : ,L1id(2,1)),mwp( : ,L1id(2,2)),mwp( : ,L1id(2,3)),mwp( : ,
```

```
    L1id(2,4))];
wp2=[mwp(:,L2id(2,1)),mwp(:,L2id(2,2)),mwp(:,L2id(2,3)),mwp(:,
    L2id(2,4))];
wp3=[mwp(:,L3id(2,1)),mwp(:,L3id(2,2)),mwp(:,L3id(2,3)),mwp(:,
    L3id(2,4))];

S=wp1./(d11.^2); S=sum(S,2); S0=sum(1./(d11.^2));
mwpL1=S./S0; dlmwrite('pwpL1era5.txt',mwpL1./0.9);

S=wp2./(d22.^2); S=sum(S,2); S0=sum(1./(d22.^2));
mwpL2=S./S0; dlmwrite('pwpL2era5.txt',mwpL2./0.9);

S=wp3./(d33.^2); S=sum(S,2); S0=sum(1./(d33.^2));
mwpL3=S./S0; dlmwrite('pwpL3era5.txt',mwpL3./0.9);
%%
% Copernicus WAVE data selection
lat=ncread('CopernDataswh1.nc','latitude');
lon=ncread('CopernDataswh1.nc','longitude');
cCop=[lat,lon]';
dlmwrite('coordsCopNxN.txt',cCop,'delimiter','\t','precision',8);

locs = [37.220,35.964,35.378;
          26.115,23.160,27.038];

L3id=[1216,1217,1253,1254;
        323,324,342,343];

era5NL30=[cw(1,L3id(2,1)), cw(1,L3id(2,2)), cw(1,L3id(2,3)), cw(1,L3id
    (2,4));
            cw(2,L3id(2,1)), cw(2,L3id(2,2)), cw(2,L3id(2,3)), cw(2,L3id
                (2,4))];

ellipsoid = [6378.1 , 0.00335];

distC0=100; distC1=100; distC2=100; distC3=100; distC4=100;
for i=1:length(cCop)
    for j=1:length(cCop)
        dcop0=distance(locs(1,3),locs(2,3),cCop(1,i),cCop(2,j),ellipsoid
            );
        dcop1=distance(era5NL30(1,1),era5NL30(2,1),cCop(1,i),cCop(2,j),
            ellipsoid);
        dcop2=distance(era5NL30(1,2),era5NL30(2,2),cCop(1,i),cCop(2,j),
            ellipsoid);
```

```
108         dcop3=distance(era5NL30(1,3),era5NL30(2,3),cCop(1,i),cCop(2,j),
                ellipsoid);
109         dcop4=distance(era5NL30(1,4),era5NL30(2,4),cCop(1,i),cCop(2,j),
                ellipsoid);
110         if dcop0<distC0
111             i0=i; j0=j; distC0=dcop0;
112         end
113         if dcop1<distC1
114             i1=i; j1=j; distC1=dcop1;
115         end
116         if dcop2<distC2
117             i2=i; j2=j; distC2=dcop2;
118         end
119         if dcop3<distC3
120             i3=i; j3=j; distC3=dcop3;
121         end
122         if dcop4<distC4
123             i4=i; j4=j; distC4=dcop4;
124         end
125     end
126 end
127 copNL30=[cCop(1,i1),cCop(1,i2),cCop(1,i3),cCop(1,i4);
128            cCop(2,j1),cCop(2,j2),cCop(2,j3),cCop(2,j4)];
129 copL3=[cCop(1,i0);
130        cCop(2,j0)];
131
132 % Copernicus WAVE data interpolation
133 Hs1=ncread('CopernDataswh1.nc','VHM0');
134 Hs2=ncread('CopernDataswh2.nc','VHM0');
135 Tp1=ncread('CopernDataspp1.nc','VTPK');
136 Tp2=ncread('CopernDataspp2.nc','VTPK');
137
138 hs1=[squeeze(Hs1(j1,i1,:)),squeeze(Hs1(j2,i2,:)),squeeze(Hs1(j3,i3,
      :)),squeeze(Hs1(j4,i4,:))];
139 hs2=[squeeze(Hs2(j1,i1,:)),squeeze(Hs2(j2,i2,:)),squeeze(Hs2(j3,i3,
      :)),squeeze(Hs2(j4,i4,:))];
140 tp1=[squeeze(Tp1(j1,i1,:)),squeeze(Tp1(j2,i2,:)),squeeze(Tp1(j3,i3,
      :)),squeeze(Tp1(j4,i4,:))];
141 tp2=[squeeze(Tp2(j1,i1,:)),squeeze(Tp2(j2,i2,:)),squeeze(Tp2(j3,i3,
      :)),squeeze(Tp2(j4,i4,:))];
142
143 hs=[hs1;hs2];
144 tp=[tp1;tp2];
```

```
145 hs0=[squeeze(Hs1(j0,i0,:));squeeze(Hs2(j0,i0,:))];
146 tp0=[squeeze(Tp1(j0,i0,:));squeeze(Tp2(j0,i0,:))];
147
148 distCop=[];
149 for i=1:4
150     distCop = [distCop; distance(copL3(1,1),copL3(2,1),copNL30(1,i),
        copNL30(2,i),ellipsoid)];
151 end
152 dCop=distCop';
153
154 % Significant Wave Height
155 S=hs./(dCop.^2); S=sum(S,2); S0=sum(1./(dCop.^2));
156 cophL3=S./S0; dlmwrite('swhNL3Cop.txt',cophL3); dlmwrite('swhL3Cop.txt',
    hs0);
157
158 % Peak Wave Period
159 S=tp./(dCop.^2); S=sum(S,2); S0=sum(1./(dCop.^2));
160 coptL3=S./S0; dlmwrite('pwpNL3Cop.txt',coptL3); dlmwrite('pwpL3Cop.txt',
    tp0);
161
162 %%
163 % distance between L3 and nearest point of Copernicus data
164 diffdistL3=distance(35.378,27.038,copL3(1,1),copL3(2,1),ellipsoid);
165
166 % distances between points from ERA5 and Copernicus (neighboring of L3)
167 for k=1:4
168     distance(era5NL30(1,k),era5NL30(2,k),copNL30(1,k),copNL30(2,k),
        ellipsoid);
169 end
170
171 % comparison between era5 and copernicus data (upper left point of L3 -
    nearly the same point regarding lat lon)
172 diffdist=distance(era5NL30(1,1),era5NL30(2,1),copNL30(1,1),copNL30(2,1),
    ellipsoid);
173
174 % Regression (draft plots)
175 subplot(1,2,1)
176 scatter(wh3(:,1),hs(:,1),'filled'); title('Significant Wave Height (
    Hs)');
177 xlabel('Hs from ERA5 (m)'); ylabel('Hs from Copernicus (m)');
178 xlim([0 ceil(max(wh3(:,1)))]); ylim([0 ceil(max(hs(:,1)))]);
179 subplot(1,2,2)
180 scatter(wp3(:,1),tp(:,1),'filled'); title('Peak Wave Period (Tp)');
```

```
181 xlabel('Tp from ERA5 (s)'); ylabel('Tp from Copernicus (s)');
182 xlim([0 ceil(max(wp3( : ,1)))]); ylim([0 ceil(max(tp( : ,1)))]);
183
184 % ——— comparison of copernicus data (L3 and interpolation for L3)
185 % Linear Regression: Hs
186 x=cophL3; y=hs0;
187 mbe=mean((x-y),'omitnan');
188 [p,S] = polyfit(x,y,1);
189 yfit = polyval(p,x);
190 yresid=y-yfit;
191 SSresid = sum(yresid.^2);
192 SStotal = (length(y)-1) * var(y);
193 rsq = 1 - SSresid/SStotal;
194 figure(1)
195 scatter(x,y,'b.');
196 xlim([floor(min(x)) ceil(max(x))]);
197 ylim([floor(min(y)) ceil(max(y))]);
198 hold on; grid on;
199 plot([0;x],[p(2);yfit],'r-','linewidth',1.5);
200 xlabel('Significant Wave Height from interpolation (m)'); ylabel('
      Significant Wave Height of L3 (m)');
201 %title('Copernicus Data','fontsize',14);
202 text=['R^2=' num2str(rsq,3) newline 'bias=' num2str(mbe,3)];
203 legend({'Data',['y = ' num2str(round(p(1),3)) 'x - ' num2str(abs(
      round(p(2),3)))],text},'Location','northwest','fontsize',11);
204 saveas(figure(1), ['swhCopLR.jpg'], 'jpeg');
205
206 % Linear Regression: Tp
207 x=coptL3; y=tp0;
208 mbe=mean((x-y),'omitnan');
209 [p,S] = polyfit(x,y,1);
210 yfit = polyval(p,x);
211 yresid=y-yfit;
212 SSresid = sum(yresid.^2);
213 SStotal = (length(y)-1) * var(y);
214 rsq = 1 - SSresid/SStotal;
215 figure(2)
216 scatter(x,y,'b.');
217 xlim([floor(min(x)) ceil(max(x))]);
218 ylim([floor(min(y)) ceil(max(y))]);
219 hold on; grid on;
220 plot([0;x],[p(2);yfit],'r-','linewidth',1.5);
221 xlabel('Peak Wave Period from interpolation (s)'); ylabel('Peak Wave
```

```
    Period of L3 (s)');
%title('Copernicus Data','fontsize',14);
text=['R^2=' num2str(rsq,3) newline 'bias=' num2str(mbe,3)];
legend({'Data',['y = ' num2str(round(p(1),3)) 'x + ' num2str(round(p
    (2),3))],text},'Location','northwest','fontsize',11);
saveas(figure(2), ['pwpCopLR.jpg'], 'jpeg');

%%
% ERA5 WAVE data fix for L3
aa=dlmread('swhL3era5.txt');
ab=dlmread('pwpL3era5.txt');

aaf=0.841.*aa-0.012;
abf=0.8.*ab+1.02;

dlmwrite('swhL3era5_fixed.txt',aaf);
dlmwrite('pwpL3era5_fixed.txt',abf);
```

*Matlab code script for wind energy calculations.*

```
clc;
swh=dlmread('era5_swh_2d');
%%
clc;
clearvars -except swh
year=swh(:,1);
month=swh(:,2);

files=["wspL1era5.txt","wspL2era5.txt","wspL3era5.txt"];
titles=["Location 1","Location 2","Location 3"]; y1=[]; y2=[]; y3=[];
windheight=119; % Hub height of the 10MW DTU Reference W/T
f=log(windheight/0.0002)/log(100/0.0002);
pcurve=[280,800,1530,2500,3730,5310,7290,9700,10640]; % Power curve
    values for wind speed integers
% link for the above values: https://github.com/NREL/turbine-models/blob
    /master/Offshore/DTU_10MW_178_RWT_v1.csv
for nf=1:3
wspL=dlmread(files(nf)); wsp=wspL*f;
sum(wspL>25)
perc1=(sum(wspL>=4)-sum(wspL>25))/175320
end
% perc2=(sum(wsp>=4)-sum(wsp>25))/175320

% per year
uy=cell(1,20);
for y=2000:2019
    for kk=1:length(year)
        if year(kk,1)==y
            uy{y-1999}=[uy{y-1999};wsp(kk)];
        end
    end
end

env1=zeros(1,20); env3=zeros(1,20);
for y=1:20
    pv1=0; wtfullp=10640*length(uy{y});
    for i=1:length(uy{y})
        for j=4:11 % Change accordingly, ATTENTION to indices
            if uy{y}(i)>=j && uy{y}(i)<j+1
                pv1=pv1+pcurve(j-3)+(uy{y}(i)-j)*(pcurve(j-2)-pcurve(j
                    -3));
```

```
39              end
40          end
41          if uy{y}(i)>11 && uy{y}(i)<11.4 % Change accordingly
42              pv1=pv1+pcurve(end-1)+(uy{y}(i)-11)*(pcurve(end)-pcurve(end
                    -1))/(11.4-11);
43          end
44          if uy{y}(i)>=11.4 && uy{y}(i)<=25 % Change accordingly
45              pv1=pv1+10640; % Change accordingly
46          end
47      end
48      env1(1,y)=pv1; env3(1,y)=pv1/wtfullp;
49  end
50  yfpower=mean(env1)/10^6; % GWh
51
52
53  % per month
54  um=cell(1,12);
55  for m=1:12
56      for kk=1:length(month)
57          if month(kk,1)==m
58              um{m}=[um{m};wsp(kk)];
59          end
60      end
61  end
62
63  env2=zeros(1,12);
64  for m=1:12
65      pv1=0;
66      for i=1:length(um{m})
67          for j=4:11 % Change accordingly
68              if um{m}(i)>=j && um{m}(i)<j+1
69                  pv1=pv1+pcurve(j-3)+(um{m}(i)-j)*(pcurve(j-2)-pcurve(j
                        -3));
70              end
71          end
72          if um{m}(i)>11 && um{m}(i)<11.4 % Change accordingly
73              pv1=pv1+pcurve(end-1)+(um{m}(i)-11)*(pcurve(end)-pcurve(end
                    -1))/(11.4-11);
74          end
75          if um{m}(i)>=11.4 && um{m}(i)<=25 % Change accordingly
76              pv1=pv1+10640; % Change accordingly
77          end
78      end
```

```
79        env2(1,m)=pv1/20;
80    end
81    mfpower=sum(env2)/10^6; %GWh
82
83    % verification
84    disp(titles(nf))
85    disp(yfpower)
86    disp(mfpower)
87
88    y1=[y1;env1/10^6]; y2=[y2;env2/10^6]; y3=[y3;env3];
89
90    end
91
92    %%
93    %plots
94    f1=figure;
95    x=2000:2019;
96    b=bar(x,y1','hist');
97    b(1).FaceColor=[0.1 0.3 1];
98    b(2).FaceColor=[0, 0.5, 0];
99    b(3).FaceColor=[0.9290, 0.6940, 0.1250];
100   xlim([1999,2020]); xticks([x]);  grid on
101   ylim([0,75]);
102   ylabel('Annual energy output in GWh');
103   xlabel('Year');
104   legend(titles);
105   set(gca,'FontSize',15);
106   %saveas(f1,'AnnualEn', 'jpeg');
107
108   f2=figure;
109   x=1:12;
110   b=bar(x,y2','hist');
111   b(1).FaceColor=[0.1 0.3 1];
112   b(2).FaceColor=[0, 0.5, 0];
113   b(3).FaceColor=[0.9290, 0.6940, 0.1250];
114   xlim([0,13]); xticks([x]);  grid on;
115   ylim([0,8.5]);
116   ylabel('Monthly mean energy output in GWh');
117   xlabel('Month');
118   legend(titles);
119   set(gca,'FontSize',15);
120   %saveas(f2,'MonMeanEn', 'jpeg');
121
```

```
f3=figure;
x=2000:2019;
b=bar(x,y3','hist');
b(1).FaceColor=[0.1 0.3 1];
b(2).FaceColor=[0, 0.5, 0];
b(3).FaceColor=[0.9290, 0.6940, 0.1250];
xlim([1999,2020]); xticks([x]); grid on;
ylim([0,0.90]);
ylabel('Annual Capacity Factor');
xlabel('Year');
legend(titles);
set(gca,'FontSize',15);
%saveas(f3,'CF', 'jpeg');
```

*Matlab code script for wave energy calculations.*

```
clc; clear all; %Run in HYDRO folder
wvec=[0.05:0.05:3];
c=[1 4 2 4 1];
dx=0.05; n=length(wvec);
freq1=dlmread(['OccTabL1.txt']); freq2=dlmread(['OccTabL2.txt']); freq3=
    dlmread(['OccTabL3.txt']);
datfiles=["temp1TLP003.txt","temp1TLP303.txt","temp1TLP603.txt","
    temp1CHA003.txt","temp1CHA303.txt","temp1CHA603.txt"]; %"temp1ROP003
    .txt","temp1ROP303.txt","temp1ROP603.txt",

for file=1:length(datfiles)
    data=dlmread(datfiles(file)); eabs=data(181:240,3)'.*wvec
        *15.5^2*1.025*9.81;
    l=1;
    for Tp=1.5:11.5
        wp=2*pi()/Tp; m=1;
        for Hs=0.5:5.5
            if Tp/sqrt(Hs)<=3.6
                Gamma=5;
            elseif Tp/sqrt(Hs)>=5
                Gamma=1;
            else
                Gamma=exp(5.75-1.15*Tp/sqrt(Hs));
            end
            Ag=1-0.287*log(Gamma);
            for j=1:length(wvec)
                w=wvec(j);
                if w<=wp
                    sigma=0.07;
                else
                    sigma=0.09;
                end
                kappa=-0.5*((w-wp)/sigma/wp)^2;
                Spm(j)=5/16*Hs^2*wp^4*w^(-5)*exp(-5/4*(w/wp)^(-4)); %
                    Pierson_Moskowitz spectrum
                Sj(j)=Ag*Spm(j)*Gamma^(exp(kappa)); %Jonswap spectrum
            end
            z1=0;
            p=2.*eabs.*Sj;
            for i=1:4:(n-4)
                z1=z1+c.*[p(i) p(i+1) p(i+2) p(i+3) p(i+4)].*dx;
```

```
37                 end
38                 Power{file}(l,m)=sum(z1)/3; %kW / cell array (order of
                       display): TLP(00deg, 30deg, 60deg), ROPE(00deg, 30deg,
                       60deg), CHAIN(00deg, 30deg, 60deg)
39                 m=m+1;
40             end
41             l=l+1;
42         end
43         TotPower1=freq1.*Power{file}; TotPower2=freq2.*Power{file};
               TotPower3=freq3.*Power{file};
44         %cell arrays for the 3 locations (order of display): TLP(00deg, 30
               deg, 60deg), ROPE(00deg, 30deg, 60deg), CHAIN(00deg, 30deg, 60
               deg)
45         MeanAnnTotPower1{file}=TotPower1/20; MeanAnnTotPower2{file}=
               TotPower2/20; MeanAnnTotPower3{file}=TotPower3/20; %kWh/year /
               Tables
46         TotP(file,1)=sum(sum(MeanAnnTotPower1{file})); TotP(file,2)=sum(sum(
               MeanAnnTotPower2{file})); TotP(file,3)=sum(sum(MeanAnnTotPower3{
               file})); %kWh/year
47 end
48
49 saveP=[]; saveEn1=[]; saveEn2=[]; saveEn3=[];
50 for i=1:length(datfiles)
51     saveP=[saveP;Power{i}];
52     saveEn1=[saveEn1;MeanAnnTotPower1{i}];
53     saveEn2=[saveEn2;MeanAnnTotPower2{i}];
54     saveEn3=[saveEn3;MeanAnnTotPower3{i}];
55 end
56 dlmwrite('SeaStatePower.txt',saveP,'delimiter','\t');
57 dlmwrite('TotEnTablesL1.txt',saveEn1,'delimiter','\t');
58 dlmwrite('TotEnTablesL2.txt',saveEn2,'delimiter','\t');
59 dlmwrite('TotEnTablesL3.txt',saveEn3,'delimiter','\t');
60 dlmwrite('TotalEnergyOWC.txt',TotP,'delimiter','\t');
61
62 % plots for Total Power
63 titles=["TLP (00 deg)","TLP (30 deg)","TLP (60 deg)","CHAIN (00 deg)","
       CHAIN (30 deg)","CHAIN (60 deg)"]; %"ROPE (00 deg)","ROPE (30 deg)
       ","ROPE (60 deg)",
64 figure()
65 y=TotP'/1000;
66 b=bar(y,'hist','FaceColor','flat');
67 ylabel('Total absorbed energy (MWh/y)');
68 xticks([1 2 3]); xlim([0.5,3.5]);
```

```
69 xticklabels({'Location 1','Location 2','Location 3'});
70 legend(titles); grid on;
71 set(gca,'FontSize',18);
```

# Appendix C

Table C.1: Absorbed power in $kW$ for 0 deg wave direction and wire rope mooring system. Highest value is depicted in bold.

| Peak Wave | Significant Wave Height $H_s$ (m) | | | | | |
|---|---|---|---|---|---|---|
| Period $T_p$ (s) | $0-1$ | $1-2$ | $2-3$ | $3-4$ | $4-5$ | $5-6$ |
| $1-2$ | 0.00 | 0.00 | 0.00 | 0.00 | 0.00 | 0.00 |
| $2-3$ | 0.00 | 0.01 | 0.02 | 0.05 | 0.08 | 0.12 |
| $3-4$ | 0.01 | 0.07 | 0.19 | 0.38 | 0.63 | 0.94 |
| $4-5$ | 0.21 | 1.43 | 3.90 | 7.65 | 12.65 | 18.90 |
| $5-6$ | 2.53 | 20.15 | 43.11 | 84.49 | 139.66 | 208.63 |
| $6-7$ | 8.51 | 76.58 | 222.49 | 437.26 | 722.81 | 1079.80 |
| $7-8$ | 14.04 | 126.35 | 385.77 | 977.99 | 1809.70 | 2703.40 |
| $8-9$ | 16.58 | 149.20 | 414.45 | 906.30 | 1697.50 | **2721.10** |
| $9-10$ | 17.21 | 154.86 | 430.18 | 843.15 | 1389.60 | 2074.20 |
| $10-11$ | 17.72 | 159.45 | 442.91 | 868.11 | 1426.40 | 2019.00 |
| $11-12$ | 18.57 | 167.09 | 464.14 | 909.71 | 1503.80 | 2217.10 |

Table C.2: Table C2. Absorbed power in $kW$ for 30 deg wave direction and TLP system. Highest value is depicted in bold.

| Peak Wave | Significant Wave Height $H_s$ (m) | | | | | |
|---|---|---|---|---|---|---|
| Period $T_p$ (s) | $0-1$ | $1-2$ | $2-3$ | $3-4$ | $4-5$ | $5-6$ |
| $1-2$ | 0.00 | 0.00 | 0.00 | 0.00 | 0.00 | 0.00 |
| $2-3$ | 0.00 | 0.00 | 0.00 | 0.01 | 0.01 | 0.01 |
| $3-4$ | 0.01 | 0.07 | 0.18 | 0.36 | 0.59 | 0.88 |
| $4-5$ | 0.35 | 2.19 | 5.91 | 11.59 | 19.15 | 28.61 |
| $5-6$ | 2.66 | 22.34 | 53.28 | 104.43 | 172.63 | 257.88 |
| $6-7$ | 7.49 | 67.43 | 209.80 | 433.87 | 717.21 | 1071.40 |
| $7-8$ | 11.81 | 106.27 | 320.57 | 793.70 | 1459.00 | **2179.50** |
| $8-9$ | 13.88 | 124.95 | 347.08 | 745.33 | 1367.60 | 2162.60 |
| $9-10$ | 14.13 | 127.17 | 353.25 | 692.37 | 1161.30 | 1762.10 |
| $10-11$ | 13.38 | 120.41 | 334.46 | 655.54 | 1080.80 | 1586.40 |
| $11-12$ | 12.22 | 109.94 | 305.39 | 598.57 | 989.48 | 1463.40 |

Table C.3: Table C3. Absorbed power in $kW$ for 30 deg wave direction and wire rope mooring system. Highest value is depicted in bold.

| Peak Wave | Significant Wave Height $H_s$ (m) | | | | | |
|---|---|---|---|---|---|---|
| Period $T_p$ (s) | $0-1$ | $1-2$ | $2-3$ | $3-4$ | $4-5$ | $5-6$ |
| $1-2$ | 0.00 | 0.00 | 0.00 | 0.00 | 0.00 | 0.00 |
| $2-3$ | 0.00 | 0.02 | 0.06 | 0.12 | 0.19 | 0.29 |
| $3-4$ | 0.01 | 0.08 | 0.22 | 0.43 | 0.71 | 1.06 |
| $4-5$ | 0.32 | 2.06 | 5.59 | 10.95 | 18.10 | 27.04 |
| $5-6$ | 2.58 | 21.46 | 50.37 | 98.73 | 163.21 | 243.80 |
| $6-7$ | 7.87 | 70.80 | 210.97 | 426.26 | 704.63 | 1052.60 |
| $7-8$ | 12.92 | 116.28 | 351.29 | 872.27 | 1604.60 | 2397.00 |
| $8-9$ | 15.48 | 139.34 | 387.07 | 847.63 | 1589.80 | **2550.60** |
| $9-10$ | 16.56 | 149.08 | 414.10 | 811.64 | 1347.30 | 2024.20 |
| $10-11$ | 18.00 | 161.95 | 449.86 | 881.73 | 1449.30 | 2059.30 |
| $11-12$ | 20.04 | 180.34 | 500.94 | 981.84 | 1623.00 | 2394.60 |

Table C.4: Absorbed power in $kW$ for 30 deg wave direction and studless chain mooring system. Highest value is depicted in bold.

| Peak Wave | Significant Wave Height $H_s$ (m) | | | | | |
|---|---|---|---|---|---|---|
| Period $T_p$ (s) | $0-1$ | $1-2$ | $2-3$ | $3-4$ | $4-5$ | $5-6$ |
| $1-2$ | 0.00 | 0.00 | 0.00 | 0.00 | 0.00 | 0.00 |
| $2-3$ | 0.00 | 0.03 | 0.07 | 0.14 | 0.24 | 0.36 |
| $3-4$ | 0.02 | 0.08 | 0.23 | 0.45 | 0.75 | 1.11 |
| $4-5$ | 0.32 | 2.06 | 5.57 | 10.92 | 18.06 | 26.97 |
| $5-6$ | 2.58 | 21.51 | 50.46 | 98.91 | 163.50 | 244.25 |
| $6-7$ | 7.84 | 70.58 | 210.84 | 426.51 | 705.05 | 1053.20 |
| $7-8$ | 12.78 | 114.97 | 348.05 | 868.55 | 1601.30 | 2392.10 |
| $8-9$ | 15.23 | 137.04 | 380.67 | 831.02 | 1552.60 | **2483.90** |
| $9-10$ | 16.30 | 146.68 | 407.44 | 798.58 | 1318.30 | 1971.30 |
| $10-11$ | 17.83 | 160.45 | 445.69 | 873.55 | 1435.60 | 2035.70 |
| $11-12$ | 20.00 | 180.02 | 500.05 | 980.09 | 1620.20 | 2390.80 |

Table C.5: Absorbed power in $kW$ for 60 deg wave direction and TLP system. Highest value is depicted in bold.

| Peak Wave | Significant Wave Height $H_s$ (m) | | | | | |
|---|---|---|---|---|---|---|
| Period $T_p$ (s) | $0-1$ | $1-2$ | $2-3$ | $3-4$ | $4-5$ | $5-6$ |
| $1-2$ | 0.00 | 0.00 | 0.00 | 0.00 | 0.00 | 0.00 |
| $2-3$ | 0.00 | 0.00 | 0.00 | 0.00 | 0.01 | 0.01 |
| $3-4$ | 0.01 | 0.06 | 0.16 | 0.32 | 0.53 | 0.79 |
| $4-5$ | 0.29 | 1.85 | 5.04 | 9.87 | 16.32 | 24.38 |
| $5-6$ | 4.39 | 33.97 | 66.16 | 129.67 | 214.35 | 320.20 |
| $6-7$ | 12.66 | 113.90 | 374.41 | 778.92 | 1287.60 | 1923.50 |
| $7-8$ | 18.15 | 163.34 | 503.59 | 1299.60 | 2414.70 | **3607.10** |
| $8-9$ | 19.53 | 175.80 | 488.34 | 994.09 | 1718.50 | 2615.20 |
| $9-10$ | 18.57 | 167.12 | 464.23 | 909.89 | 1451.70 | 2109.50 |
| $10-11$ | 16.71 | 150.38 | 417.72 | 818.73 | 1345.60 | 1911.50 |
| $11-12$ | 14.69 | 132.18 | 367.15 | 719.62 | 1189.60 | 1752.10 |

Table C.6: Absorbed power in $kW$ for 60 deg wave direction and wire rope mooring system. Highest value is depicted in bold.

| Peak Wave | Significant Wave Height $H_s$ (m) | | | | | |
|---|---|---|---|---|---|---|
| Period $T_p$ (s) | $0-1$ | $1-2$ | $2-3$ | $3-4$ | $4-5$ | $5-6$ |
| $1-2$ | 0.00 | 0.00 | 0.00 | 0.00 | 0.00 | 0.00 |
| $2-3$ | 0.00 | 0.01 | 0.02 | 0.03 | 0.06 | 0.08 |
| $3-4$ | 0.01 | 0.04 | 0.11 | 0.22 | 0.36 | 0.54 |
| $4-5$ | 0.18 | 1.07 | 2.90 | 5.69 | 9.40 | 14.04 |
| $5-6$ | 3.06 | 23.59 | 45.46 | 89.10 | 147.29 | 220.02 |
| $6-7$ | 10.17 | 91.52 | 275.57 | 551.08 | 910.97 | 1360.80 |
| $7-8$ | 16.11 | 144.98 | 446.32 | 1153.70 | 2152.70 | **3215.80** |
| $8-9$ | 18.48 | 166.28 | 461.88 | 988.76 | 1808.00 | 2853.00 |
| $9-10$ | 18.87 | 169.80 | 471.67 | 924.47 | 1498.90 | 2206.80 |
| $10-11$ | 19.37 | 174.37 | 484.36 | 949.34 | 1558.90 | 2191.80 |
| $11-12$ | 20.44 | 183.97 | 511.03 | 1001.60 | 1655.70 | 2439.50 |

Table C.7: Absorbed power in $kW$ for 60 deg wave direction and studless chain mooring system. Highest value is depicted in bold.

| Peak Wave | Significant Wave Height $H_s$ (m) | | | | | |
|---|---|---|---|---|---|---|
| Period $T_p$ (s) | $0-1$ | $1-2$ | $2-3$ | $3-4$ | $4-5$ | $5-6$ |
| $1-2$ | 0.00 | 0.00 | 0.00 | 0.00 | 0.00 | 0.00 |
| $2-3$ | 0.00 | 0.01 | 0.02 | 0.04 | 0.06 | 0.10 |
| $3-4$ | 0.01 | 0.04 | 0.11 | 0.22 | 0.36 | 0.54 |
| $4-5$ | 0.17 | 1.05 | 2.84 | 5.57 | 9.21 | 13.75 |
| $5-6$ | 3.00 | 23.11 | 44.54 | 87.31 | 144.32 | 215.59 |
| $6-7$ | 9.98 | 89.82 | 269.87 | 539.15 | 891.24 | 1331.40 |
| $7-8$ | 15.78 | 142.06 | 437.95 | 1136.20 | 2123.50 | **3172.20** |
| $8-9$ | 18.08 | 162.68 | 451.90 | 966.39 | 1764.20 | 2779.70 |
| $9-10$ | 18.50 | 166.54 | 462.60 | 906.69 | 1464.80 | 2149.70 |
| $10-11$ | 19.17 | 172.56 | 479.33 | 939.48 | 1542.50 | 2165.50 |
| $11-12$ | 20.46 | 184.09 | 511.37 | 1002.30 | 1656.80 | 2441.40 |

Table C.8: Annual absorbed energy in $kWh/y$ for 0 deg wave direction and wire rope mooring system in Location 1. Highest value is depicted in bold.

| Peak Wave | Significant Wave Height $H_s$ (m) | | | | | |
|---|---|---|---|---|---|---|
| Period $T_p$ (s) | $0-1$ | $1-2$ | $2-3$ | $3-4$ | $4-5$ | $5-6$ |
| $1-2$ | 0 | 0 | 0 | 0 | 0 | 0 |
| $2-3$ | 0 | 0 | 0 | 0 | 0 | 0 |
| $3-4$ | 25 | 0 | 0 | 0 | 0 | 0 |
| $4-5$ | 514 | 1202 | 0 | 0 | 0 | 0 |
| $5-6$ | 850 | 39496 | 2270 | 0 | 0 | 0 |
| $6-7$ | 50 | 12716 | **106380** | 3433 | 0 | 0 |
| $7-8$ | 1 | 468 | 10975 | 63276 | 5791 | 0 |
| $8-9$ | 0 | 0 | 21 | 1541 | 13325 | 1769 |
| $9-10$ | 0 | 0 | 0 | 0 | 69 | 622 |
| $10-11$ | 0 | 0 | 0 | 0 | 0 | 0 |
| $11-12$ | 0 | 0 | 0 | 0 | 0 | 0 |

Table C.9: Annual absorbed energy in $kWh/y$ for 30 deg wave direction and TLP system in Location 1. Highest value is depicted in bold.

| Peak Wave | Significant Wave Height $H_s$ (m) | | | | | |
|---|---|---|---|---|---|---|
| Period $T_p$ (s) | $0-1$ | $1-2$ | $2-3$ | $3-4$ | $4-5$ | $5-6$ |
| $1-2$ | 0 | 0 | 0 | 0 | 0 | 0 |
| $2-3$ | 0 | 0 | 0 | 0 | 0 | 0 |
| $3-4$ | 25 | 0 | 0 | 0 | 0 | 0 |
| $4-5$ | 845 | 1833 | 0 | 0 | 0 | 0 |
| $5-6$ | 896 | 43792 | 2805 | 0 | 0 | 0 |
| $6-7$ | 44 | 11196 | **100320** | 3406 | 0 | 0 |
| $7-8$ | 1 | 393 | 9120 | 51353 | 4669 | 0 |
| $8-9$ | 0 | 0 | 17 | 1267 | 10736 | 1406 |
| $9-10$ | 0 | 0 | 0 | 0 | 58 | 529 |
| $10-11$ | 0 | 0 | 0 | 0 | 0 | 0 |
| $11-12$ | 0 | 0 | 0 | 0 | 0 | 0 |

Table C.10: Annual absorbed energy in $kWh/y$ for 30 deg wave direction and wire rope mooring system in Location 1. Highest value is depicted in bold.

| Peak Wave | Significant Wave Height $H_s$ (m) | | | | | |
|---|---|---|---|---|---|---|
| Period $T_p$ (s) | $0-1$ | $1-2$ | $2-3$ | $3-4$ | $4-5$ | $5-6$ |
| $1-2$ | 0 | 0 | 0 | 0 | 0 | 0 |
| $2-3$ | 1 | 0 | 0 | 0 | 0 | 0 |
| $3-4$ | 31 | 0 | 0 | 0 | 0 | 0 |
| $4-5$ | 781 | 1730 | 0 | 0 | 0 | 0 |
| $5-6$ | 867 | 42068 | 2652 | 0 | 0 | 0 |
| $6-7$ | 46 | 11756 | **100870** | 3346 | 0 | 0 |
| $7-8$ | 1 | 430 | 9994 | 56436 | 5135 | 0 |
| $8-9$ | 0 | 0 | 19 | 1441 | 12480 | 1658 |
| $9-10$ | 0 | 0 | 0 | 0 | 67 | 607 |
| $10-11$ | 0 | 0 | 0 | 0 | 0 | 0 |
| $11-12$ | 0 | 0 | 0 | 0 | 0 | 0 |

Table C.11: Annual absorbed energy in $kWh/y$ for 30 deg wave direction and studless chain mooring system in Location 1. Highest value is depicted in bold.

| Peak Wave | Significant Wave Height $H_s$ (m) | | | | | |
|---|---|---|---|---|---|---|
| Period $T_p$ (s) | $0-1$ | $1-2$ | $2-3$ | $3-4$ | $4-5$ | $5-6$ |
| $1-2$ | 0 | 0 | 0 | 0 | 0 | 0 |
| $2-3$ | 1 | 0 | 0 | 0 | 0 | 0 |
| $3-4$ | 33 | 0 | 0 | 0 | 0 | 0 |
| $4-5$ | 781 | 1727 | 0 | 0 | 0 | 0 |
| $5-6$ | 870 | 42167 | 2657 | 0 | 0 | 0 |
| $6-7$ | 46 | 11720 | **100810** | 3348 | 0 | 0 |
| $7-8$ | 1 | 425 | 9902 | 56195 | 5124 | 0 |
| $8-9$ | 0 | 0 | 19 | 1413 | 12188 | 1615 |
| $9-10$ | 0 | 0 | 0 | 0 | 66 | 591 |
| $10-11$ | 0 | 0 | 0 | 0 | 0 | 0 |
| $11-12$ | 0 | 0 | 0 | 0 | 0 | 0 |

Table C.12: Annual absorbed energy in $kWh/y$ for 60 deg wave direction and TLP system in Location 1. Highest value is depicted in bold.

| Peak Wave | Significant Wave Height $H_s$ (m) | | | | | |
|---|---|---|---|---|---|---|
| Period $T_p$ (s) | $0-1$ | $1-2$ | $2-3$ | $3-4$ | $4-5$ | $5-6$ |
| $1-2$ | 0 | 0 | 0 | 0 | 0 | 0 |
| $2-3$ | 0 | 0 | 0 | 0 | 0 | 0 |
| $3-4$ | 22 | 0 | 0 | 0 | 0 | 0 |
| $4-5$ | 688 | 1554 | 0 | 0 | 0 | 0 |
| $5-6$ | 1479 | 66582 | 3483 | 0 | 0 | 0 |
| $6-7$ | 75 | 18914 | **179020** | 6115 | 0 | 0 |
| $7-8$ | 1 | 604 | 14327 | 84082 | 7727 | 0 |
| $8-9$ | 0 | 0 | 24 | 1690 | 13490 | 1700 |
| $9-10$ | 0 | 0 | 0 | 0 | 73 | 633 |
| $10-11$ | 0 | 0 | 0 | 0 | 0 | 0 |
| $11-12$ | 0 | 0 | 0 | 0 | 0 | 0 |

Table C.13: Annual absorbed energy in $kWh/y$ for 60 deg wave direction and wire rope mooring system in Location 1. Highest value is depicted in bold.

| Peak Wave | Significant Wave Height $H_s$ (m) | | | | | |
|---|---|---|---|---|---|---|
| Period $T_p$ (s) | $0-1$ | $1-2$ | $2-3$ | $3-4$ | $4-5$ | $5-6$ |
| $1-2$ | 0 | 0 | 0 | 0 | 0 | 0 |
| $2-3$ | 0 | 0 | 0 | 0 | 0 | 0 |
| $3-4$ | 13 | 0 | 0 | 0 | 0 | 0 |
| $4-5$ | 423 | 900 | 0 | 0 | 0 | 0 |
| $5-6$ | 1031 | 46238 | 2393 | 0 | 0 | 0 |
| $6-7$ | 60 | 15196 | **131760** | 4326 | 0 | 0 |
| $7-8$ | 1 | 536 | 12698 | 74646 | 6889 | 0 |
| $8-9$ | 0 | 0 | 23 | 1681 | 14193 | 1855 |
| $9-10$ | 0 | 0 | 0 | 0 | 75 | 662 |
| $10-11$ | 0 | 0 | 0 | 0 | 0 | 0 |
| $11-12$ | 0 | 0 | 0 | 0 | 0 | 0 |

Table C.14: Annual absorbed energy in $kWh/y$ for 60 deg wave direction and studless chain mooring system in Location 1. Highest value is depicted in bold.

| Peak Wave | Significant Wave Height $H_s$ (m) | | | | | |
|---|---|---|---|---|---|---|
| Period $T_p$ (s) | $0-1$ | $1-2$ | $2-3$ | $3-4$ | $4-5$ | $5-6$ |
| $1-2$ | 0 | 0 | 0 | 0 | 0 | 0 |
| $2-3$ | 0 | 0 | 0 | 0 | 0 | 0 |
| $3-4$ | 13 | 0 | 0 | 0 | 0 | 0 |
| $4-5$ | 415 | 881 | 0 | 0 | 0 | 0 |
| $5-6$ | 1010 | 45299 | 2345 | 0 | 0 | 0 |
| $6-7$ | 59 | 14915 | **129040** | 4232 | 0 | 0 |
| $7-8$ | 1 | 526 | 12460 | 73509 | 6795 | 0 |
| $8-9$ | 0 | 0 | 23 | 1643 | 13849 | 1807 |
| $9-10$ | 0 | 0 | 0 | 0 | 73 | 645 |
| $10-11$ | 0 | 0 | 0 | 0 | 0 | 0 |
| $11-12$ | 0 | 0 | 0 | 0 | 0 | 0 |

Table C.15: Annual absorbed energy in $kWh/y$ for 0 deg wave direction and wire rope mooring system in Location 2. Highest value is depicted in bold.

| Peak Wave | Significant Wave Height $H_s$ (m) | | | | | |
|---|---|---|---|---|---|---|
| Period $T_p$ (s) | $0-1$ | $1-2$ | $2-3$ | $3-4$ | $4-5$ | $5-6$ |
| $1-2$ | 0 | 0 | 0 | 0 | 0 | 0 |
| $2-3$ | 0 | 0 | 0 | 0 | 0 | 0 |
| $3-4$ | 10 | 0 | 0 | 0 | 0 | 0 |
| $4-5$ | 553 | 593 | 0 | 0 | 0 | 0 |
| $5-6$ | 2955 | 30890 | 888 | 0 | 0 | 0 |
| $6-7$ | 1656 | 58949 | **87827** | 1574 | 0 | 0 |
| $7-8$ | 217 | 24949 | 87087 | 78679 | 3981 | 0 |
| $8-9$ | 1 | 6259 | 29447 | 43639 | 31997 | 2585 |
| $9-10$ | 0 | 829 | 8195 | 13280 | 8268 | 1556 |
| $10-11$ | 0 | 0 | 1063 | 2084 | 1498 | 808 |
| $11-12$ | 0 | 0 | 0 | 91 | 301 | 1109 |

Table C.16: Annual absorbed energy in $kWh/y$ for 30 deg wave direction and TLP system in Location 2. Highest value is depicted in bold.

| Peak Wave | Significant Wave Height $H_s$ (m) | | | | | |
|---|---|---|---|---|---|---|
| Period $T_p$ (s) | $0-1$ | $1-2$ | $2-3$ | $3-4$ | $4-5$ | $5-6$ |
| $1-2$ | 0 | 0 | 0 | 0 | 0 | 0 |
| $2-3$ | 0 | 0 | 0 | 0 | 0 | 0 |
| $3-4$ | 11 | 0 | 0 | 0 | 0 | 0 |
| $4-5$ | 908 | 904 | 0 | 0 | 0 | 0 |
| $5-6$ | 3112 | 34250 | 1098 | 0 | 0 | 0 |
| $6-7$ | 1458 | 51906 | **82820** | 1562 | 0 | 0 |
| $7-8$ | 182 | 20983 | 72370 | 63853 | 3210 | 0 |
| $8-9$ | 1 | 5242 | 24660 | 35888 | 25780 | 2054 |
| $9-10$ | 0 | 680 | 6729 | 10905 | 6910 | 1322 |
| $10-11$ | 0 | 0 | 803 | 1573 | 1135 | 635 |
| $11-12$ | 0 | 0 | 0 | 60 | 198 | 732 |

Table C.17: Annual absorbed energy in $kWh/y$ for 30 deg wave direction and wire rope mooring system in Location 2. Highest value is depicted in bold.

| Peak Wave | Significant Wave Height $H_s$ (m) | | | | | |
|---|---|---|---|---|---|---|
| Period $T_p$ (s) | $0-1$ | $1-2$ | $2-3$ | $3-4$ | $4-5$ | $5-6$ |
| $1-2$ | 0 | 0 | 0 | 0 | 0 | 0 |
| $2-3$ | 0 | 0 | 0 | 0 | 0 | 0 |
| $3-4$ | 13 | 0 | 0 | 0 | 0 | 0 |
| $4-5$ | 839 | 853 | 0 | 0 | 0 | 0 |
| $5-6$ | 3014 | 32902 | 1038 | 0 | 0 | 0 |
| $6-7$ | 1531 | 54500 | **83279** | 1535 | 0 | 0 |
| $7-8$ | 200 | 22959 | 79304 | 70174 | 3530 | 0 |
| $8-9$ | 1 | 5846 | 27501 | 40813 | 29968 | 2423 |
| $9-10$ | 0 | 798 | 7889 | 12783 | 8016 | 1518 |
| $10-11$ | 0 | 0 | 1080 | 2116 | 1522 | 824 |
| $11-12$ | 0 | 0 | 0 | 98 | 325 | 1197 |

Table C.18: Annual absorbed energy in $kWh/y$ for 30 deg wave direction and studless chain mooring system in Location 2. Highest value is depicted in bold.

| Peak Wave | Significant Wave Height $H_s$ (m) | | | | | |
|---|---|---|---|---|---|---|
| Period $T_p$ (s) | $0-1$ | $1-2$ | $2-3$ | $3-4$ | $4-5$ | $5-6$ |
| $1-2$ | 0 | 0 | 0 | 0 | 0 | 0 |
| $2-3$ | 0 | 0 | 0 | 0 | 0 | 0 |
| $3-4$ | 14 | 0 | 0 | 0 | 0 | 0 |
| $4-5$ | 840 | 851 | 0 | 0 | 0 | 0 |
| $5-6$ | 3021 | 32979 | 1040 | 0 | 0 | 0 |
| $6-7$ | 1527 | 54332 | **83227** | 1535 | 0 | 0 |
| $7-8$ | 197 | 22702 | 78573 | 69874 | 3523 | 0 |
| $8-9$ | 1 | 5749 | 27047 | 40013 | 29267 | 2360 |
| $9-10$ | 0 | 785 | 7762 | 12578 | 7844 | 1479 |
| $10-11$ | 0 | 0 | 1070 | 2097 | 1507 | 814 |
| $11-12$ | 0 | 0 | 0 | 98 | 324 | 1195 |

Table C.19: Annual absorbed energy in $kWh/y$ for 60 deg wave direction and TLP system in Location 2. Highest value is depicted in bold.

| Peak Wave | Significant Wave Height $H_s$ (m) | | | | | |
|---|---|---|---|---|---|---|
| Period $T_p$ (s) | $0-1$ | $1-2$ | $2-3$ | $3-4$ | $4-5$ | $5-6$ |
| $1-2$ | 0 | 0 | 0 | 0 | 0 | 0 |
| $2-3$ | 0 | 0 | 0 | 0 | 0 | 0 |
| $3-4$ | 9 | 0 | 0 | 0 | 0 | 0 |
| $4-5$ | 739 | 766 | 0 | 0 | 0 | 0 |
| $5-6$ | 5139 | 52074 | 1363 | 0 | 0 | 0 |
| $6-7$ | 2464 | 87683 | **147800** | 2804 | 0 | 0 |
| $7-8$ | 280 | 32251 | 113690 | 104550 | 5312 | 0 |
| $8-9$ | 1 | 7375 | 34696 | 47866 | 32394 | 2484 |
| $9-10$ | 0 | 894 | 8844 | 14331 | 8637 | 1582 |
| $10-11$ | 0 | 0 | 1003 | 1965 | 1413 | 765 |
| $11-12$ | 0 | 0 | 0 | 72 | 238 | 876 |

Table C.20: Annual absorbed energy in $kWh/y$ for 60 deg wave direction and wire rope mooring system in Location 2. Highest value is depicted in bold.

| Peak Wave | Significant Wave Height $H_s$ (m) | | | | | |
|---|---|---|---|---|---|---|
| Period $T_p$ (s) | $0-1$ | $1-2$ | $2-3$ | $3-4$ | $4-5$ | $5-6$ |
| $1-2$ | 0 | 0 | 0 | 0 | 0 | 0 |
| $2-3$ | 0 | 0 | 0 | 0 | 0 | 0 |
| $3-4$ | 5 | 0 | 0 | 0 | 0 | 0 |
| $4-5$ | 455 | 443 | 0 | 0 | 0 | 0 |
| $5-6$ | 3582 | 36162 | 936 | 0 | 0 | 0 |
| $6-7$ | 1979 | 70450 | **108780** | 1984 | 0 | 0 |
| $7-8$ | 249 | 28626 | 100760 | 92817 | 4736 | 0 |
| $8-9$ | 1 | 6975 | 32817 | 47609 | 34082 | 2710 |
| $9-10$ | 0 | 908 | 8985 | 14560 | 8918 | 1655 |
| $10-11$ | 0 | 0 | 1163 | 2278 | 1637 | 877 |
| $11-12$ | 0 | 0 | 0 | 100 | 331 | 1220 |

Table C.21: Annual absorbed energy in $kWh/y$ for 60 deg wave direction and studless chain mooring system in Location 2. Highest value is depicted in bold.

| Peak Wave Period $T_p$ (s) | Significant Wave Height $H_s$ (m) | | | | | |
|---|---|---|---|---|---|---|
| | $0-1$ | $1-2$ | $2-3$ | $3-4$ | $4-5$ | $5-6$ |
| $1-2$ | 0 | 0 | 0 | 0 | 0 | 0 |
| $2-3$ | 0 | 0 | 0 | 0 | 0 | 0 |
| $3-4$ | 6 | 0 | 0 | 0 | 0 | 0 |
| $4-5$ | 446 | 434 | 0 | 0 | 0 | 0 |
| $5-6$ | 3509 | 35429 | 918 | 0 | 0 | 0 |
| $6-7$ | 1943 | 69145 | **106530** | 1941 | 0 | 0 |
| $7-8$ | 244 | 28049 | 98866 | 91403 | 4672 | 0 |
| $8-9$ | 1 | 6825 | 32107 | 46532 | 33255 | 2641 |
| $9-10$ | 0 | 891 | 8813 | 14280 | 8715 | 1612 |
| $10-11$ | 0 | 0 | 1150 | 2255 | 1620 | 866 |
| $11-12$ | 0 | 0 | 0 | 100 | 331 | 1221 |

Table C.22: Annual absorbed energy in $kWh/y$ for 0 deg wave direction and wire rope mooring system in Location 3. Highest value is depicted in bold.

| Peak Wave Period $T_p$ (s) | Significant Wave Height $H_s$ (m) | | | | | |
|---|---|---|---|---|---|---|
| | $0-1$ | $1-2$ | $2-3$ | $3-4$ | $4-5$ | $5-6$ |
| $1-2$ | 0 | 0 | 0 | 0 | 0 | 0 |
| $2-3$ | 0 | 0 | 0 | 0 | 0 | 0 |
| $3-4$ | 7 | 0 | 0 | 0 | 0 | 0 |
| $4-5$ | 675 | 139 | 0 | 0 | 0 | 0 |
| $5-6$ | 3418 | 47051 | 69 | 0 | 0 | 0 |
| $6-7$ | 902 | 53068 | **67113** | 219 | 0 | 0 |
| $7-8$ | 8 | 2982 | 27467 | 44010 | 633 | 0 |
| $8-9$ | 0 | 0 | 83 | 2085 | 2886 | 0 |
| $9-10$ | 0 | 0 | 0 | 0 | 0 | 0 |
| $10-11$ | 0 | 0 | 0 | 0 | 0 | 0 |
| $11-12$ | 0 | 0 | 0 | 0 | 0 | 0 |

Table C.23: Annual absorbed energy in $kWh/y$ for 30 deg wave direction and TLP system in Location 3. Highest value is depicted in bold.

| Peak Wave | Significant Wave Height $H_s$ (m) | | | | | |
|---|---|---|---|---|---|---|
| Period $T_p$ (s) | $0-1$ | $1-2$ | $2-3$ | $3-4$ | $4-5$ | $5-6$ |
| $1-2$ | 0 | 0 | 0 | 0 | 0 | 0 |
| $2-3$ | 0 | 0 | 0 | 0 | 0 | 0 |
| $3-4$ | 7 | 0 | 0 | 0 | 0 | 0 |
| $4-5$ | 1109 | 211 | 0 | 0 | 0 | 0 |
| $5-6$ | 3600 | 52169 | 85 | 0 | 0 | 0 |
| $6-7$ | 795 | 46727 | **63287** | 217 | 0 | 0 |
| $7-8$ | 7 | 2508 | 22825 | 35717 | 511 | 0 |
| $8-9$ | 0 | 0 | 69 | 1714 | 2325 | 0 |
| $9-10$ | 0 | 0 | 0 | 0 | 0 | 0 |
| $10-11$ | 0 | 0 | 0 | 0 | 0 | 0 |
| $11-12$ | 0 | 0 | 0 | 0 | 0 | 0 |

Table C.24: Annual absorbed energy in $kWh/y$ for 30 deg wave direction and wire rope mooring system in Location 3. Highest value is depicted in bold.

| Peak Wave | Significant Wave Height $H_s$ (m) | | | | | |
|---|---|---|---|---|---|---|
| Period $T_p$ (s) | $0-1$ | $1-2$ | $2-3$ | $3-4$ | $4-5$ | $5-6$ |
| $1-2$ | 0 | 0 | 0 | 0 | 0 | 0 |
| $2-3$ | 0 | 0 | 0 | 0 | 0 | 0 |
| $3-4$ | 8 | 0 | 0 | 0 | 0 | 0 |
| $4-5$ | 1025 | 199 | 0 | 0 | 0 | 0 |
| $5-6$ | 3486 | 50116 | 81 | 0 | 0 | 0 |
| $6-7$ | 834 | 49063 | **63638** | 213 | 0 | 0 |
| $7-8$ | 8 | 2744 | 25012 | 39252 | 562 | 0 |
| $8-9$ | 0 | 0 | 77 | 1950 | 2703 | 0 |
| $9-10$ | 0 | 0 | 0 | 0 | 0 | 0 |
| $10-11$ | 0 | 0 | 0 | 0 | 0 | 0 |
| $11-12$ | 0 | 0 | 0 | 0 | 0 | 0 |

Table C.25: Annual absorbed energy in $kWh/y$ for 30 deg wave direction and studless chain mooring system in Location 3. Highest value is depicted in bold.

| Peak Wave Period $T_p$ (s) | Significant Wave Height $H_s$ (m) | | | | | |
|---|---|---|---|---|---|---|
| | $0-1$ | $1-2$ | $2-3$ | $3-4$ | $4-5$ | $5-6$ |
| $1-2$ | 0 | 0 | 0 | 0 | 0 | 0 |
| $2-3$ | 0 | 0 | 0 | 0 | 0 | 0 |
| $3-4$ | 9 | 0 | 0 | 0 | 0 | 0 |
| $4-5$ | 1026 | 199 | 0 | 0 | 0 | 0 |
| $5-6$ | 3495 | 50233 | 81 | 0 | 0 | 0 |
| $6-7$ | 832 | 48911 | **63599** | 213 | 0 | 0 |
| $7-8$ | 8 | 2713 | 24781 | 39085 | 560 | 0 |
| $8-9$ | 0 | 0 | 76 | 1911 | 2640 | 0 |
| $9-10$ | 0 | 0 | 0 | 0 | 0 | 0 |
| $10-11$ | 0 | 0 | 0 | 0 | 0 | 0 |
| $11-12$ | 0 | 0 | 0 | 0 | 0 | 0 |

Table C.26: Annual absorbed energy in $kWh/y$ for 60 deg wave direction and TLP system in Location 3. Highest value is depicted in bold.

| Peak Wave Period $T_p$ (s) | Significant Wave Height $H_s$ (m) | | | | | |
|---|---|---|---|---|---|---|
| | $0-1$ | $1-2$ | $2-3$ | $3-4$ | $4-5$ | $5-6$ |
| $1-2$ | 0 | 0 | 0 | 0 | 0 | 0 |
| $2-3$ | 0 | 0 | 0 | 0 | 0 | 0 |
| $3-4$ | 6 | 0 | 0 | 0 | 0 | 0 |
| $4-5$ | 903 | 179 | 0 | 0 | 0 | 0 |
| $5-6$ | 5945 | 79319 | 106 | 0 | 0 | 0 |
| $6-7$ | 1342 | 78935 | **112940** | 389 | 0 | 0 |
| $7-8$ | 11 | 3855 | 35856 | 58480 | 845 | 0 |
| $8-9$ | 0 | 0 | 98 | 2286 | 2922 | 0 |
| $9-10$ | 0 | 0 | 0 | 0 | 0 | 0 |
| $10-11$ | 0 | 0 | 0 | 0 | 0 | 0 |
| $11-12$ | 0 | 0 | 0 | 0 | 0 | 0 |

Table C.27: Annual absorbed energy in $kWh/y$ for 60 deg wave direction and wire rope mooring system in Location 3. Highest value is depicted in bold.

| Peak Wave | Significant Wave Height $H_s$ (m) | | | | | |
|---|---|---|---|---|---|---|
| Period $T_p$ (s) | $0-1$ | $1-2$ | $2-3$ | $3-4$ | $4-5$ | $5-6$ |
| $1-2$ | 0 | 0 | 0 | 0 | 0 | 0 |
| $2-3$ | 0 | 0 | 0 | 0 | 0 | 0 |
| $3-4$ | 3 | 0 | 0 | 0 | 0 | 0 |
| $4-5$ | 556 | 104 | 0 | 0 | 0 | 0 |
| $5-6$ | 4143 | 55083 | 73 | 0 | 0 | 0 |
| $6-7$ | 1078 | 63421 | **83124** | 276 | 0 | 0 |
| $7-8$ | 10 | 3422 | 31778 | 51918 | 753 | 0 |
| $8-9$ | 0 | 0 | 92 | 2274 | 3074 | 0 |
| $9-10$ | 0 | 0 | 0 | 0 | 0 | 0 |
| $10-11$ | 0 | 0 | 0 | 0 | 0 | 0 |
| $11-12$ | 0 | 0 | 0 | 0 | 0 | 0 |

Table C.28: Annual absorbed energy in $kWh/y$ for 60 deg wave direction and studless chain mooring system in Location 3. Highest value is depicted in bold.

| Peak Wave | Significant Wave Height $H_s$ (m) | | | | | |
|---|---|---|---|---|---|---|
| Period $T_p$ (s) | $0-1$ | $1-2$ | $2-3$ | $3-4$ | $4-5$ | $5-6$ |
| $1-2$ | 0 | 0 | 0 | 0 | 0 | 0 |
| $2-3$ | 0 | 0 | 0 | 0 | 0 | 0 |
| $3-4$ | 4 | 0 | 0 | 0 | 0 | 0 |
| $4-5$ | 544 | 101 | 0 | 0 | 0 | 0 |
| $5-6$ | 4058 | 53965 | 71 | 0 | 0 | 0 |
| $6-7$ | 1058 | 62246 | **81405** | 270 | 0 | 0 |
| $7-8$ | 9 | 3353 | 31182 | 51127 | 743 | 0 |
| $8-9$ | 0 | 0 | 90 | 2223 | 2999 | 0 |
| $9-10$ | 0 | 0 | 0 | 0 | 0 | 0 |
| $10-11$ | 0 | 0 | 0 | 0 | 0 | 0 |
| $11-12$ | 0 | 0 | 0 | 0 | 0 | 0 |

# Appendix D

*HAMVAB Input file for the case of studless chain mooring system, excited by 0 deg wave. Analysis in the [0.05, 1.50] frequency range.*

```
HYDRODYNAMIC ANALYSIS. ARISTEIA FLOATING W/T.
.TRUE. .TRUE. .TRUE. .TRUE. .TRUE.
200.0          4   30    7    00.000
    3
  1  1  1  1  1
  1  1  1  1  1
  1  1  1  1  1
  1  1  1  1  1
15.50       15.50       15.50       6.000
14.00       14.00       14.00       0.000
7.000       7.000       7.000       0.000
-28.87      14.43       14.43       0.000
0.000       -25.00      25.00       0.000
0.000
    7  39    7    1    1    3    0
    015.50
0.050  0.100  0.150  0.200  0.250  0.300  0.350  0.400  0.450  0.500
0.550  0.600  0.650  0.700  0.750  0.800  0.850  0.900  0.950  1.000
1.050  1.100  1.150  1.200  1.250  1.300  1.350  1.400  1.450  1.500
    2    1    1    1    2
0.0   0.0   -14.780   14.6575E3   6.385E6    6.385E6    1.170E7
1 -28.87 0.00 -20.00
153.867 4.833 18.483 0 0 0
2800 0 1790.193
2 14.43 25.00 -20.00
38.467 1.208 18.483 0 0 0
2800 0 1790.193
3 14.43 -25.00 -20.00
38.467 1.208 18.483 0 0 0
2800 0 1790.193
15.50       15.50       15.50       6.000
    1
GEOMETRIC CHARACTERISTICS OF THE INDIVIDUAL BODY
15.50
.FALSE..TRUE. .TRUE. .false..TRUE.
     2     0
     1     0
180.0       200.0       192.0
    79    39    79
```

```
 7.000       14.00       15.50
 200.0       -2.891      325961.     1967.
      2
  0.0
  343.848
      2
      3
      2
      0
      1
GEOMETRIC CHARACTERISTICS OF THE CYLINDER SUPPORTING THE W/
 6.000
 .FALSE..TRUE.  .TRUE.  .FALSE..TRUE.
      0      0

 180.0
     79
 6.000
 200.0       -5.000      41732.      1118.
      0
 1
 1
 0.00   0.00   0.00   0.00   110080.00    0.00   13.37  0.00   0.00   -34.48
      1569.90   -17.62    0.00   0.00   0.00   0.00   -0.01  0.01
 0.00   0.00   0.00   -110080.00  0.00   -439.37   0.14   2.50   -0.03  -292.68
      -2696.60  -18.30    0.00   0.00   0.00   0.02   -0.29  -11.88
 0.00   0.00   0.00   0.00   439.37    0.00   0.15   -0.03  2.48   9.53   35.31
      -2710.90  0.00   0.00   0.00   -0.01  11.64  0.29
 0.00   -110080.00  0.00   10397000.00  0.00   56517.00  5407.50   -292.72
      9.51   68330.00  959020.00    2475.80   0.00   0.00   0.00   -1042600.00
      89.05  1378.80
 110080.00    0.00   439.37    0.00   10337000.00  0.00   1568.90   16.97  17.29
      -6081.10  200850.00    60737.00  0.00   0.00   0.00   0.00   -1042600.00
      -27.35
 0.00   -439.37   0.00   56517.00  0.00   97578.00  -13.77    -17.67    17.53
      2048.60   -64646.00    16212.00  0.00   0.00   0.00   -4308.80  35.57  -3.59
```